Ray-Born Modelling and Full Waveform Inversion

Hans Christian Bertelsen Tengesdal

Thesis for the degree
Master of Science

Department of Earth Science

University of Bergen

June 3, 2013

"Most people, if you describe a train of events to them will tell you what the result would be. They can put those events together in their minds, and argue from them that something will come to pass. There are few people, however, who, if you told them a result, would be able to evolve from their own inner consciousness what the steps were which led up to that result. This power is what I mean when I talk of reasoning backward."

Sherlock Holmes, in A Study of Scarlet

by Arthur Conan Doyle (1859 - 1930)

Abstract

Seismic forward modelling is used to simulate seismic wave propagation in the subsurface. Common modelling techniques include methods such as the ray-Born approximation and the finite difference method. In this thesis I present a comparison between the ray-Born approximation and the finite difference method. This comparison consists of computing synthetic seismograms using both methods for several seismic velocity models and performing a comparison between them. The main motivation for this comparison is to see if the ray-Born approximation, which is known to be faster, provides enough accuracy to provide an efficient alternative to the finite difference method. The ray-Born approximation was found to be sufficiently accurate in cases where the velocity model did not have large velocity contrasts and multipathing did not occur. In those cases the method can replace the finite difference method in forward modelling algorithms.

Full waveform inversion is a technique that is used to compute a model of the subsurface given the seismic data recorded at the surface. In order to perform full waveform inversion, forward modelling is an obvious requirement. Traditional full waveform inversion algorithms use the finite difference method to perform forward modelling and the cost of the computation is therefore high. In order to reduce the cost of the inversion, a full waveform inversion algorithm that uses the ray-Born approximation instead of the finite difference method has been developed. The results from the full waveform inversion when using the ray-Born approximation show that it is possible to achieve an accurate reproduction of the subsurface at a greatly reduced cost compared to the finite difference method. The ray-Born approximation is therefore evaluated to be a method that can replace the finite difference method both in forward modelling and in full waveform inversion algorithms.

Acknowledgements

This thesis has been written at the Institute of geoscience, University of Bergen, under the guidance of associate professor Henk Keers.

The process of achieving the results presented in thesis have been an entertaining and educational process. As a result of writing this thesis I have gotten a greater understanding for geophysical modelling and believe I have gained important knowledge that will help me during my professional career.

I would like to thank my supervisor Henk Keers and cosupervisor Lars Ottemller for helpful ideas, conversations and guidance during my two years as a master student. I would like to thank Alexander Minakov and Audun Libak for our discussions about inversion.

I would like to thank my fellow students for the time we have had together at the University. They have become good friends that have made my time at the University fun and entertaining in addition to helping with comments on my thesis.

I would like to thank my family for the economical and moral support through my years as a student. Their help has made it easier to focus on completing my studies. Finally I would like to thank my girlfriend Kristine for her kindness and support. You have been very important for me when I've been writing my thesis.

Contents

List of Figures

List of Tables

Chapter 1

Introduction

1.1 Introduction

The global energy demand is increasing while the production from mature hydrocarbon reservoirs is decreasing. In order to accommodate this growing energy demand in the future it is crucial to increase the hydrocarbon production by improving the hydrocarbon extraction rate from mature reservoirs as well identifying new hydrocarbon reservoirs. Seismic exploration is the primary method of determining the physical properties of the subsurface and identifying commercially economic deposits of oil and gas. In order to increase the hydrocarbon production it is therefore crucial to continue the development of the technology used in seismics.

Seismics consist of seismic acquisition and processing of seismic data. It is essential to develop processing methods that will increase subsurface resolution and allow for accurate and efficient identification of new reservoirs as well as maintaining the production from mature fields. Traditional seismic processing techniques consist of increasing the signal to noise ratio, attenuation of surface multiples, velocity model building and imaging. The velocity model is determined only through the use of travel times and therefore only resolves the large scale structures of the subsurface. Imaging is used to identify small scale structures such as faults and discontinuities by using the rough velocity model as a starting point. Due to the inaccuracy of the rough velocity model, the small scale structures obtained from imaging may appear at the incorrect location or not at all. An attempt to overcome this weakness has resulted in the development of full waveform inversion.

Full waveform inversion methods use the entire waveform instead of just travel times and accurate inversion algorithms instead of simplified inversion algorithms. By using the entire waveform it is possible to resolve small subsurface structures with accurate position and velocity. Full waveform inversion was first introduced by Tarantola (1984a). Among those who have performed it later we find Gauthier et al. (1986) who performed full waveform inversion in the space-time domain and Pratt et al. (1998) and Operto et al. (2006) who performed full waveform inversion in the space-frequency domain. Most full waveform inversion algorithms are based on the finite difference method as the primary forward modelling method. Inversion methods based on the finite difference method are slow and due to the memory consumption of the method it is difficult to perform waveform inversion for large models.

The main objective of this thesis is to develop a full waveform inversion algorithm that is faster than full waveform inversion algorithms based on the finite difference method while still resolving the subsurface structures with high accuracy. The ray-Born approximation has been evaluated as a potential candidate to replace the finite difference method as the primary forward modelling method in full waveform inversion. I will therefore give a review of the forward modelling techniques: the ray-Born approximation and the finite difference method. This review includes the background theory as well as the numerical implementation of the methods. I will perform a quantitative comparison between the ray-Born approximation and the finite difference method for several seismic velocity models. Using this

information it is possible to evaluate if the ray-Born approximation can be used as a fast and accurate replacement for the finite difference method in both forward modelling and full waveform inversion. Finally, I will present a full waveform inversion algorithm based on the ray-Born approximation and perform a comparison between the results obtained from the ray-Born approximation full waveform inversion algorithm with a full waveform inversion algorithm based on the finite difference method. (The modelling methods that are presented in this thesis have been implemented in Matlab as a part of the work of the thesis.)

The thesis has been divided into six different chapters. In chapter 1 I give an introduction to the thesis where I discuss the motivation behind the work that has been done as well as the objectives of the thesis. In Chapter 2 I give the relevant background theory for the forward modelling methods that have been used in this thesis. In Chapter 3 I discuss the numerical implementation of the forward modelling techniques and perform a comparison between the ray-Born approximation and the finite difference method. In Chapter 4 I give the background theory required in order to perform full waveform inversion. In Chapter 5 I discuss the numerical implementation and results from the full waveform inversion algorithm that has been developed. In chapter 6 I discuss the results of the thesis and suggest further improvements and directions that can be taken in order to further develop the full waveform inversion algorithm.

Chapter 2

Forward Modelling: Theory

2.1 Outline

In this chapter I present the theoretical background of the three different forward modelling methods that are used in this thesis: geometrical ray theory, the ray-Born approximation and the finite difference method. The methods have been applied to the constant density acoustic wave equation. This equation will for the remainder of the thesis be referred to as the wave equation.

2.2 The Wave Equation

Seismic forward modelling consists of solving the acoustic wave equation with constant density (e.g Auld (1973), Pujol (2003) and Cerveny (2005)) that is given as:

$$\nabla^2 P(\mathbf{x},t) - \frac{1}{c^2(\mathbf{x})}\frac{\partial^2 P(\mathbf{x},t)}{\partial t^2} = S(\mathbf{x},t), \tag{2.1}$$

with initial conditions $P(\mathbf{x},0)$ and $\frac{\partial^2 P(\mathbf{x},0)}{\partial t^2}$ given. ∇^2 is the Laplace operator, $P(\mathbf{x},\mathrm{t})$ is the acoustic pressure at $\mathbf{x}$ and t, $c(\mathbf{x})$ is the seismic velocity at $\mathbf{x}$ and $S(\mathbf{x},t)$ is the source at position $\mathbf{x}$ in 2-D or 3-D and time t.

Solutions to the wave equation (2.1) (e.g Cerveny (2005)) for a point source in time and space $S(\mathbf{x},t) = -\delta(\mathbf{x}-\mathbf{x_s})\delta(t-t_0)$ are called Green functions and are denoted by a G. Here $\mathbf{x_s}$ is the source location and δ is the Dirac distribution. We can set $t_0 = 0$ as we assume that the velocity c is time independent. In this case G satisfies:

$$\Delta G(\mathbf{x},\mathbf{x_s},t) - \frac{1}{c^2(\mathbf{x})}\frac{\partial^2 G(\mathbf{x},\mathbf{x_s},t)}{\partial t^2} = -\delta(\mathbf{x}-\mathbf{x_s})\delta(t). \tag{2.2}$$

Once the Green function is known, it can be used to represent the solution to equation (2.1), $P(\mathbf{x},t)$ for a general source $S(\mathbf{x},t)$.

$$P(\mathbf{x},t) = \int G(\mathbf{x},\mathbf{x_s},t-t_0)S(\mathbf{x},t)d\mathbf{x}dt. \tag{2.3}$$

In this thesis $S(\mathbf{x},t) = \delta(\mathbf{x}-\mathbf{x_s})R(t)$, where $R(t)$ is the Ricker wavelet (e.g Ricker (1953) and Ryan (1994)):

$$R(t) = 1 - (t-\frac{1}{f_0})^2 f_0^2 \pi^2 exp^{-(t-\frac{1}{f_0})^2\pi^2 f_0^2}, \tag{2.4}$$

where f_0 is the centre frequency of the synthetic source wavelet. The Ricker wavelet is plotted with frequencies 5,10,15 and 20 Hz in figure 2.1. The Ricker wavelet is defined as the second derivative of the error function and was chosen for it's similarity to actual seismic wavelets.

It is often convenient to use the wave equation in the frequency domain by performing a Fourier transformation (e.g Cerveny (2005)). This often simplifies the computations and can make the physical

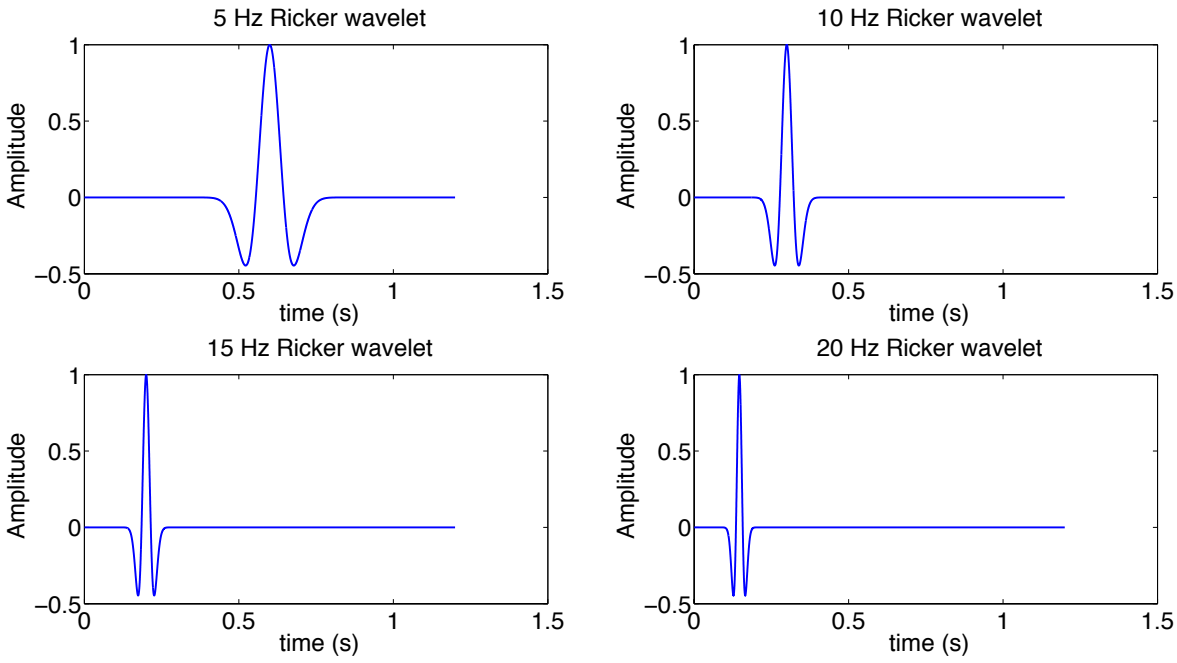

Figure 2.1: The Ricker wavelet

interpretation of the different terms clearer. The notation used for this thesis is:

$$p(\mathbf{x},\omega) = \int P(\mathbf{x},t)e^{i\omega t}dt \leftrightarrow f(\mathbf{x},t) = \frac{1}{2\pi}\int p(\mathbf{x},\omega)e^{-i\omega t}d\omega. \tag{2.5}$$

The wave equation (2.1) in the frequency domain is called the Helmholtz equation:

$$\nabla^2 p(\mathbf{x},\omega) + \frac{\omega^2}{c(\mathbf{x})^2}p(\mathbf{x},\omega) = s(\mathbf{x},\omega), \tag{2.6}$$

where $\omega = 2\pi f$, f is the frequency, $p(\mathbf{x},\omega)$ is the pressure field and $s(\mathbf{x},\omega)$ the source. Similarly, the Green function G in the frequency domain, g, satisfies

$$\nabla^2 g(\mathbf{x},\mathbf{x_s},\omega) + \frac{\omega^2}{c_0^2(\mathbf{x})}g(\mathbf{x},\mathbf{x_s},\omega) = -\delta(\mathbf{x}-\mathbf{x_s}). \tag{2.7}$$

The solution, $p(\mathbf{x},\omega)$, to the Helmholtz equation (2.6) is then written as:

$$p(\mathbf{x},\omega) = \int g(\mathbf{x},\mathbf{x_s},\omega)s(\mathbf{x},\omega)d\mathbf{x}d\omega, \tag{2.8}$$

where $g(\mathbf{x},\omega)$ is the solution of the pressure field and $s(\mathbf{x},\omega)$ is the input source wavelet for a given position $\mathbf{x}$ and ω. The equations stated in this section are valid in both 2-D and 3-D media.

2.3 Green Functions

In a constant velocity model, the frequency domain 3-D Green function is expressed as (e.g Bleistein et al. (2001), Cerveny (2005) and Nowack (2010)):

$$g(\mathbf{x},\omega) = \mathrm{A}(\mathbf{x})\mathrm{e}^{-\mathrm{i}\omega\mathrm{T}(\mathbf{x})}, \tag{2.9}$$

and the frequency domain 2-D Green function is expressed as:

$$g(\mathbf{x},\omega) = \frac{i}{4}H_0^{(1)}(\omega T(\mathbf{x})), \tag{2.10}$$

where $H_0^{(1)}$ is the Hankel function of the zeroth order and first kind, $A(\mathbf{x})$ is the amplitude and $T(\mathbf{x})$ is the travel time at position $\mathbf{x}$. The amplitude is defined as the inverse of the distance between the source and the receiver:

$$A(\mathbf{x}) = \frac{1}{\sqrt{\mathbf{x}_\mathbf{r}^2 - \mathbf{x}_\mathbf{s}^2}}, \tag{2.11}$$

and the travel time is defined as the distance between the source and the receiver over the velocity:

$$T(\mathbf{x}) = \frac{\sqrt{\mathbf{x}_\mathbf{r}^2 - \mathbf{x}_\mathbf{s}^2}}{c(\mathbf{x})}. \tag{2.12}$$

If the velocity $c(\mathbf{x})$ is constant then the solution obtained using the Green function is exact. Solving the wave equation in this way allows for a fast and accurate solution of the wavefield for constant velocity media. This method can for example be applied in acoustic oceanography where the velocity is considered to be constant.

In heterogenous media such as the subsurface rocks encountered in seismic exploration, the previous equations would give an inaccurate representation of the wavefield (e.g Bleistein et al. (2001), Cerveny (2005) and Nowack (2010)). The frequency domain 3-D Green function is given as in equation (2.9), but with a different amplitude and traveltime. The frequency domain 2-D Green function in such media can be approximated as:

$$g(\mathbf{x},\omega) = \frac{A(\mathbf{x})e^{-i(\omega T(\mathbf{x})+\frac{\pi}{4})}}{\sqrt{8\pi\omega}}. \tag{2.13}$$

The amplitude $A(\mathbf{x})$ and travel time $T(\mathbf{x})$ can not be directly solved in such media and one therefore has to consider methods such as geometrical ray theory in order to find the travel time and amplitude.

2.4 Geometrical Ray Theory

Geometrical ray theory provides a high frequency approximation of the wave equation (2.1). The theory can not be used unless the seismic properties of the model do not vary much over the distance of the

dominant wavelength of the seismic source signal. The derivation follows Pujol (2003) and Cerveny (2005). In geometrical ray theory one assumes a solution of the Helmholtz equation (2.6) similar to equation (2.9) but now with a different traveltime and amplitude. Equations for the amplitude $A(\mathbf{x})$ and traveltime $T(\mathbf{x})$ can be found by substituting the solution (2.9) into the Helmholtz equation (2.6) and setting the source term equal to 0. The Helmholtz equation can then be written as:

$$\nabla^2 g(\mathbf{x},\omega) = -\frac{\omega^2}{c(\mathbf{x})^2} g(\mathbf{x},\omega). \tag{2.14}$$

Since $\nabla^2 g(\mathbf{x},\omega)$:

$$\nabla^2 g(\mathbf{x},\omega) = \left[\nabla^2 A(\mathbf{x}) + 2i\omega\nabla(A(\mathbf{x})\,T(\mathbf{x})) + iA(\mathbf{x})\omega\nabla^2 T(\mathbf{x}) - A(\mathbf{x})\omega(\nabla T(\mathbf{x}))^2\right] e^{i\omega T(\mathbf{x})}, \tag{2.15}$$

equation (2.15) can be inserted into equation (2.14). Dividing both sides by $\omega^2 A(\mathbf{x})$ and rearranging the terms yields:

$$\left((\nabla T(\mathbf{x}))^2 - \frac{1}{c^2(\mathbf{x})}\right) - \frac{i}{\omega}\left(\frac{2}{A(\mathbf{x})}\nabla(A(\mathbf{x})\,T(\mathbf{x})) + \nabla^2 T(\mathbf{x})\right) - \frac{1}{\omega^2 A(\mathbf{x})}\nabla^2 A(\mathbf{x}) = 0. \tag{2.16}$$

Due to the presence of ω^{-1} and ω^{-2} in the last two terms of equation (2.16) the first term will be dominant for large ω. This yields the eikonal equation:

$$(\nabla T(\mathbf{x}))^2 = \frac{1}{c(\mathbf{x})^2}. \tag{2.17}$$

The eikonal equation (2.17) is a first order non-linear partial differential equation. The solution to this equation can be found by solving a set of ordinary differential equations: the kinematic ray equations. The kinematic ray equations are given as (e.g Bleistein et al. (2001) , Krebes (2004), and Cerveny (2005)):

$$\frac{d\mathbf{x}(s)}{ds} = c(\mathbf{x})\mathbf{p}(s), \tag{2.18}$$

$$\frac{d\mathbf{p}(s)}{ds} = -\frac{1}{2}\nabla c^{-2}(\mathbf{x}(s)), \tag{2.19}$$

where s is the arc length along the ray path, $\mathbf{p}(s)$ is the slowness vector that is perpendicular to the wavefront ($\mathbf{p}(s) = \nabla T(s)$) and $\mathbf{x}(s)$ is a point along the ray path. The initial conditions to the equations are given as $\mathbf{x}(0) = \mathbf{x_s}$ and $\mathbf{p}(0) = \mathbf{p}_0$ where $\mathbf{x_s}$ is the source position and $\mathbf{p_0}$ is in the $x-z$ plane given as:

$$\mathbf{p}_0 = \left(\frac{\sin\theta_0}{c(\mathbf{x_s})}, \frac{\cos\theta_0}{c(\mathbf{x_s})}\right), \tag{2.20}$$

and in 3-D given as:

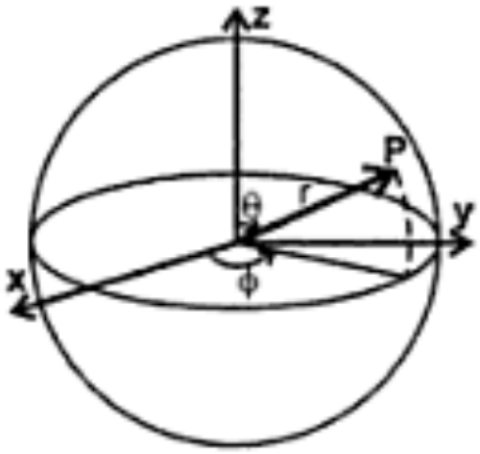

Figure 2.2: Takeoff angles used in geometrical ray theory(Fowler (1990))

$$\mathbf{p}_0 = \left(\frac{\sin\theta_0 \cos\phi_0}{c(\mathbf{x_s})}, \frac{\sin\theta_0 \sin\phi_0}{c(\mathbf{x_s})}, \frac{\cos\theta_0}{c(\mathbf{x_s})} \right), \tag{2.21}$$

where θ_0 and ϕ_0 are the takeoff angles of the ray as seen in figure 2.2. With a known ray path the travel time can be found by integrating along the ray path:

$$T(\mathbf{x}(s)) = \int_0^s \frac{ds'}{c(\mathbf{x}(s'))}. \tag{2.22}$$

The amplitude of the ray is found by solving the transport equation. The transport equation is found by considering the second term of equation (2.16) and is given as:

$$2\nabla A(\mathbf{x}) \cdot \nabla T(\mathbf{x}) + A(\mathbf{x})\nabla^2 T(\mathbf{x}) = 0. \tag{2.23}$$

From the transport equation (2.23), one can find the geometrical spreading of the ray field, which is inversely proportional to the amplitude (e.g Keers (1997) and Bleistein et al. (2001)). The geometrical spreading is in 2-D given as:

$$J = \det \left[\frac{\partial \mathbf{x}}{\partial \theta}, \frac{d\mathbf{x}}{ds} \right]^{1/2}, \tag{2.24}$$

and in 3-D given as:

$$J = \det \left[\frac{\partial \mathbf{x}}{\partial \theta}, \frac{\partial \mathbf{x}}{\partial \phi}, \frac{d\mathbf{x}}{ds} \right]^{1/2}, \tag{2.25}$$

where det is the determinant of the matrix. The derivatives of $\mathbf{x}$ and $\mathbf{p}$ along the ray with respect to the takeoff angles are governed by the dynamic ray equations (2.26) and (2.27):

$$\frac{d}{dt}\left(\frac{\partial x_i}{\partial \alpha} \right) = 2c\left(\frac{\partial c}{\partial x_j} \right)\left(\frac{\partial x_j}{\partial \alpha} \right) p_i + c^2 \frac{\partial p_i}{\partial \alpha}, \tag{2.26}$$

$$\frac{d}{dt}\left(\frac{\partial p_i}{\partial \alpha}\right) = c^{-2}\left(\frac{\partial c}{\partial x_j}\frac{\partial x_j}{\partial \alpha}\right)\frac{\partial c}{\partial x_i} - c^{-1}\frac{\partial^2 c}{\partial x_i \partial x_j}\frac{\partial x_j}{\partial \alpha}, \tag{2.27}$$

where α is either θ or ϕ. The initial conditions to the equations in 2-D are given as:

$$\frac{\partial \mathbf{x}}{\partial \theta_0} = 0, \tag{2.28}$$

$$\frac{\partial \mathbf{p}}{\partial \theta_0} = \left(\frac{\cos\theta_0}{c(\mathbf{x_s})}, \frac{-\sin\theta_0}{c(\mathbf{x_s})}\right), \tag{2.29}$$

and in 3-D given as:

$$\frac{\partial \mathbf{x}}{\partial \phi_0} = 0, \tag{2.30}$$

$$\frac{\partial \mathbf{p}}{\partial \theta_0} = \left(\frac{\cos\theta_0\cos\phi_0}{c(\mathbf{x_s})}, \frac{\cos\theta_0\sin\phi_0}{c(\mathbf{x_s})}, \frac{-\sin\theta_0}{c(\mathbf{x_s})}\right), \tag{2.31}$$

$$\frac{\partial \mathbf{p}}{\partial \phi_0} = \left(\frac{-\sin\theta_0\sin\phi_0}{c(\mathbf{x_s})}, \frac{\sin\theta_0\cos\phi_0}{c(\mathbf{x_s})}, 0\right). \tag{2.32}$$

In order to compute the amplitude and travel time along the ray paths we need to solve eight differential equations (four kinematic ray equations and four dynamic ray equations) in 2-D and 18 differential equations (six kinematic ray equations and 12 dynamic ray equations) in 3-D. The solution to the wave equation for a given source and receiver pair $(\mathbf{x_s}, \mathbf{x_r})$ using raytracing is from equation (2.8) given as:

$$p(\mathbf{x_s}, \mathbf{x_r}, \omega) = \int g(\mathbf{x_s}, \mathbf{x_r}, \omega) S(\omega) d\mathbf{x} d\omega \tag{2.33}$$

where $g(\mathbf{s}, \mathbf{r}, \omega)$ is (see equation (2.13)):

$$g(\mathbf{x_s}, \mathbf{x_r}, \omega) = \frac{A(\mathbf{x_s}, \mathbf{x_r}) e^{(-i\omega T(\mathbf{x_s}, \mathbf{x_r}) - i\frac{\pi}{4})}}{\omega}. \tag{2.34}$$

and in 3-D (from equation (2.9)) given as:

$$g(\mathbf{x_s}, \mathbf{x_r}, \omega) = A(\mathbf{x_s}, \mathbf{x_r}) e^{-i\omega T(\mathbf{x_s}, \mathbf{x_r})}. \tag{2.35}$$

By using geometrical ray theory, one replaces the partial differential equations of the wave equation that are solved for a volume by ordinary differential equations that are solved along a line. The method gives insight into wave propagation by separating the wavefield into a set of individual rays and allows for the possibility to track paths through a smooth medium in a simple, fast and intuitive way. The disadvantage of the method is that it requires the medium to be smoothly varying over the distance of a seismic wavelength. If the medium has sharp interfaces, the ray paths generated from geometrical ray theory will be incorrect. A second issues is that the amplitudes of the wavefield are incorrectly computed in media where ray paths overlap each other and multipathing occur.

2.5 Ray-Born Approximation

It is often convenient to split the seismic velocity model into a slowly varying part c_0 and a rapidly varying part c_1.

$$c(\mathbf{x}) = c_0(\mathbf{x}) + c_1(\mathbf{x}). \tag{2.36}$$

The Born approximation is a simple method that can be used to solve the wave equation (2.6) for such media. The traveltime and amplitude are computed in the smoothly varying background model c_0 using raytracing, while scattering is generated from the contrast between the smoothly varying background model and the small perturbations in the rapid varyingly part c_1. This will reduce the complexity of the forward modelling problem and thus lowering the computation time of the problem. The derivation of the Born approximation is as follows from Hudson (1977), (Cerveny, 2005, p. 93) and Moser (2012). The Born approximation is derived by assuming that the Green function of the slowly varying background model c_0 satisfying equation (2.7):

$$\frac{\omega^2}{c_0^2(\mathbf{x})} g_0(\mathbf{x}, \mathbf{x_s}, \omega) + \Delta g_0(\mathbf{x}, \mathbf{x_s}, \omega) = \delta(\mathbf{x} - \mathbf{x_s}), \tag{2.37}$$

is known and available. Our goal is to find a solution to the wave equation (2.6) in the form:

$$p = p_0 + p_1. \tag{2.38}$$

p_0 is the solution to wave equation (2.6) when $c_1 \equiv 0$. Given a source $s(\mathbf{x_s}, \omega)$, the background wave is given as:

$$p_0(\mathbf{x}, \omega) = \int g_0(\mathbf{x}, \mathbf{x_s}, \omega) s(x_s, \omega) d\mathbf{x}. \tag{2.39}$$

We can now insert equation (2.38) in equation (2.6) and subtract the background wave:

$$\omega^2 c_0^{-2}(\mathbf{x})[p(\mathbf{x}, \omega) - p_0(\mathbf{x}, \omega)] + \mathbf{\Delta}[p(\mathbf{x}, \omega) - p_0(\mathbf{x}, \omega)] = \omega^2 [c_0^{-2}.(\mathbf{x}) - c^{-2}(\mathbf{x})] p(\mathbf{x_s}, \omega) \tag{2.40}$$

Using the right hand side of ((2.40)) as the source and adding the background wave leads to:

$$p(\mathbf{x}, \omega) = p_0(\mathbf{x}, \omega) + \omega^2 \int g_0(\mathbf{x}, \mathbf{x_s}, \omega)[c_0^{-2}(\mathbf{x_s}) - c^{-2}(\mathbf{x})] p(\mathbf{x_s}, \omega) d\mathbf{x}. \tag{2.41}$$

This equation is called the Lippmann-Schwinger equation for the scattering of a wavefield p by a scatterer $c_0^{-2}(\mathbf{x}) - c^{-2}(\mathbf{x})$: It is an exact, but implicit equation for the complete wavefield p. An approximate solution to the wavefield can be found by linearization. From the Lippman Schwinger equation we have that the complete wavefield p can be expressed as:

$$p = p_0 + Lp. \tag{2.42}$$

By rearranging the equation we arrive at:

$$p = (L - I)^{-1} p_0, \tag{2.43}$$

where I is the identity matrix. The equation can be linearized by performing a Taylor series expansion and ignoring the quadratic and higher order terms, resulting in the following equation:

$$p \cong p_0 + Lp_0, \tag{2.44}$$

where $Lp_0 = p_1$ is expressed as:

$$p_1(\mathbf{x}, \omega) = \omega^2 \int g_0(\mathbf{x}, \mathbf{x_s}, \omega)[c_0^{-2}(\mathbf{x_s}) - c^{-2}(\mathbf{x})]p_0(\mathbf{x_s}, \omega)d\mathbf{x}. \tag{2.45}$$

The term on the right-hand side is the first order Born approximation for the scattered wave. For a point source $\mathbf{x_s}$ and a receiver at point $\mathbf{x_r}$ the Born approximation is given as:

$$p_1(\mathbf{x_s}, \mathbf{x_r}, \omega) = 2\omega^2 s(\omega) \int g_0(\mathbf{x_s}, \mathbf{x}, \omega) g_0(\mathbf{x_r}, \mathbf{x}, \omega) c_1(\mathbf{x}) c_0^{-3}(\mathbf{x}) d\mathbf{x}, \tag{2.46}$$

where $p_1(\mathbf{x_s}, \mathbf{x_r}, \omega)$ is the pressure field created by the scatterer $c_1(\mathbf{x})$ given a source $\mathbf{x_s}$ and a receiver $\mathbf{x_r}$ as shown in figure 2.3, $\omega = 2\pi f$, f is the frequency, and $s(\omega)$ is the source wavelet. It is often useful to use geometrical ray theory to compute the Green functions $g_0(\mathbf{x_s}, \mathbf{x}, \omega)$ and $g_0(\mathbf{x_r}, \mathbf{x}, \omega)$ in the background medium c_0. If the amplitude $A(\mathbf{x_s}, \mathbf{x})$ and travel times $T(\mathbf{x_s}, \mathbf{x})$ are computed using geometrical ray theory, the Born approximation is called the ray-Born approximation. If the travel times and amplitudes are computed using straight line distance in a homogenous velocity model it is called the Born approximation. The ray-Born/Born approximation (2.46) is only valid for small scatterers c_1 relative to the background model c_0.

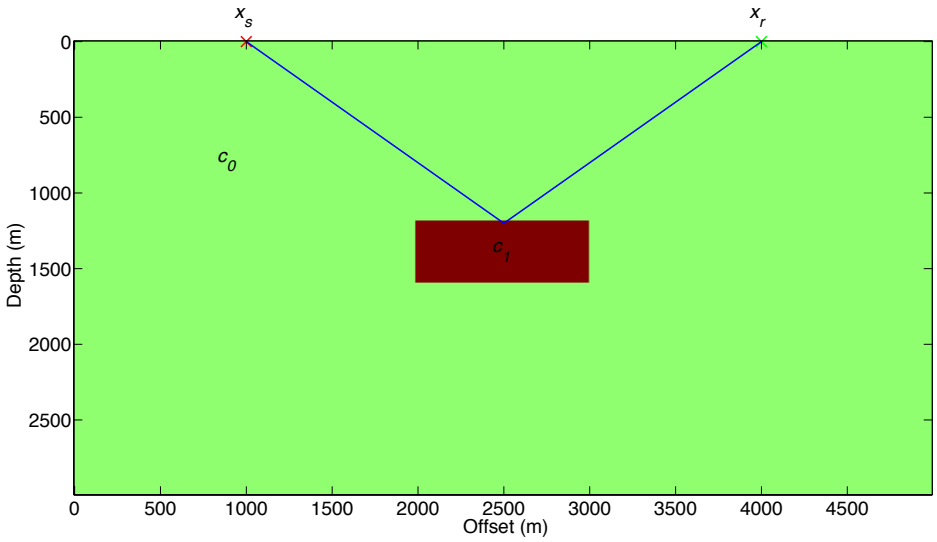

Figure 2.3: The Born approximation

Chapter 3

Forward Modelling: Numerics

3.1 Outline

The purpose of this chapter is to perform a comparison between three different forward modelling methods, geometrical ray theory, the ray-Born approximation and the finite difference method. The implementation of each method will be discussed as a part of the comparison. The methods are used to solve the wave equation in both homogenous and heterogenous media, but with different accuracy and cost. The comparison is performed because the more accurate finite difference method is computationally more expensive. The comparison will allow us to evaluate the accuracy and cost of the ray-Born approximation relative to the finite difference method and it will give a good indication on when the ray-Born approximation can be used as a replacement instead of the finite difference method. The comparison between the finite difference method and the ray-Born approximation that is presented in this chapter has not previously been performed.

The comparison is performed for four different velocity models; three basic ones and one complex one. The three basic models that have been chosen are a model with a single Gaussian scatterer, a layered medium and a random Gaussian medium. Each of the three basic models have been evaluated using a constant velocity background model and a 1-D linearly increasing velocity model. The complex model is the SEG/EAGE overthrust model.

3.2 Implementation of Geometrical Ray Theory

In order to perform raytracing we must solve the kinematic ray equations ((2.18) and (2.19)) and the dynamic ray equations ((2.26) and (2.27)) with their respective initial conditions. These equations can be solved using the Runge-Kutta method that is used to advance the solution of the equations one step at the time (e.g Kincaid and Cheney (2002)). Let us first consider the differential equation:

$$\frac{dx}{dt} = f(t, x), \tag{3.1}$$

with the initial condition $x(t_0) = x_0$. The taylor series of $x(t + h)$ is given as:

$$x(t + h) = x(t) + h\frac{dx}{dt} + \frac{h^2}{2!}\frac{d^2x}{dt^2} + \frac{h^3}{3!}\frac{d^3x}{dt^3} + \cdots. \tag{3.2}$$

From equation (3.1) the second order partial derivative of x can be defined as:

$$\frac{d^2x}{dt^2} = \frac{\partial f(t, x)}{\partial t} + \frac{\partial f(t, x)}{\partial x}\frac{dx}{dt}. \tag{3.3}$$

By inserting equation (3.3) into equation (3.2) and truncating the Taylor series, the first three terms can be written as:

$$x(t + h) = x + hf + \frac{1}{2}h^2\Big(\frac{\partial f(t, x)}{\partial t} + \frac{\partial f(t, x)}{\partial x}\frac{dx}{dt}\Big) + O(h^3), \tag{3.4}$$

and rewritten as:

$$x(t+h) = x + \frac{1}{2}hf + \frac{1}{2}h\Big[f + h\frac{\partial f(t,x)}{\partial t} + h\frac{\partial f(t,x)}{\partial x}\frac{dx}{dt}\Big] + O(h^3). \tag{3.5}$$

The partial derivatives in the third term can now be eliminated by computing the Taylor series of $f(t+h, x+hf)$:

$$f(t+h, x+hf) = f + h\frac{\partial f(t,x)}{\partial t} + h\frac{\partial f(t,x)}{\partial x}\frac{dx}{dt} + O(h^2). \tag{3.6}$$

By inserting equation (3.6) into equation (3.5) the equation is reduced to:

$$x(t+h) = x(t) + \frac{h}{2}f(t,x) + \frac{h}{2}f(t+h, x+hf(t,x)). \tag{3.7}$$

Solving differential equations in the way seen in equation (3.7) is called a second order Runge-Kutta method. The derivation shown is performed using a scaler $x(t)$, but holds equally well for a vector $\mathbf{x}(t)$ with components $[x(t), y(t), z(t)]$. The Runge-Kutta method is used to solve differential equations by advancing the solution one step at the time. The advantage of the method is that ones does not have to determine formula's for $\frac{d^2x}{dt^2}$, $\frac{d^3x}{dt^3}$ and $\frac{d^4x}{dt^4}$ by successive differentiation of equation (3.1) as is the case when using the Taylor series method. The ode23 function in Matlab is used to solve differential equations using the Runge-Kutta method and will select the proper time steps required in order to solve the ray equations accurately. While keeping the source position constant and changing the takeoff angles it is possible to trace rays originating from the source position throughout the entire model as seen in figure 3.1. In order to get a good coverage of rays throughout the entire model, the takeoff angle is increased by 0.5 degrees for each ray originating from the source position. The travel time, amplitude and position are computed along the ray path of each ray and stored in a vector.

3.3 The Ray-Born Approximation

In order to compute the ray-Born approximation one needs to divide a velocity model into a background velocity model $c_0(\mathbf{x})$ and a scatterer $c_1(\mathbf{x})$, where $c(\mathbf{x}) = c_0(\mathbf{x}) + c_1(\mathbf{x})$. Raytracing is performed in the background velocity model and the traveltime and amplitude is computed along the ray path of each ray. The traveltime and amplitude along the ray paths are thereafter interpolated onto a square grid $\mathbf{x}$. The interpolation is performed using Delaunay triangulation. Delaunay triangulation will divide data into a grid consisting of triangles. Using these triangles, interpolation onto a square grid can be performed. Delaunay triangulation was chosen due to its ability to accurately perform interpolation on scattered grids. This process is repeated for each source and receiver in the model. In figure 3.2 and figure 3.3, it is possible to see the traveltime and amplitude at all grid points given the source position and ray paths seen in figure 3.1. Using the traveltimes and amplitudes computed for all grid points for each source and receiver it is possible to compute synthetic seismograms using the ray-Born approximation. The ray-Born approximation was derived in section 2.5 and is given as:

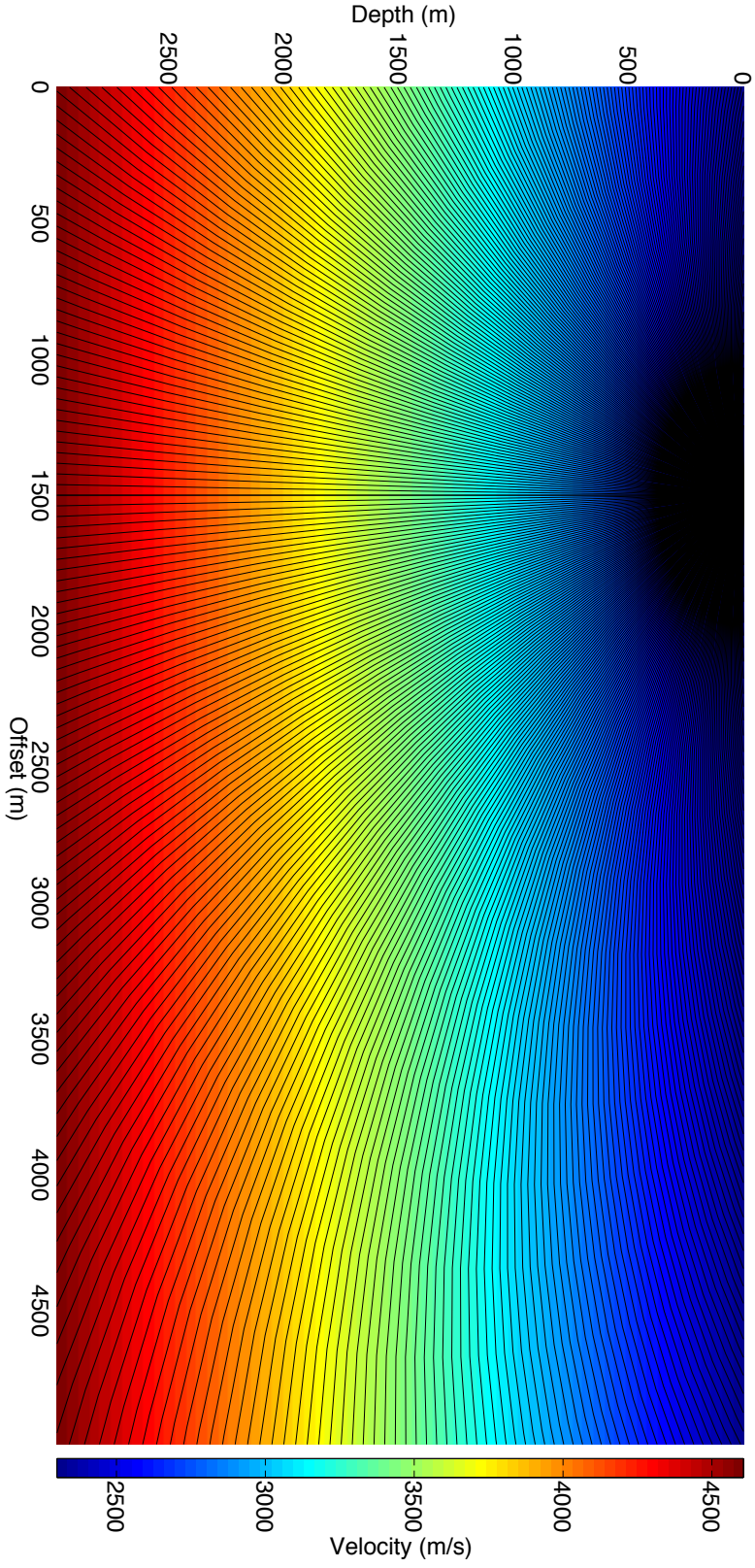

Figure 3.1: Raytracing through a 1-D velocity model

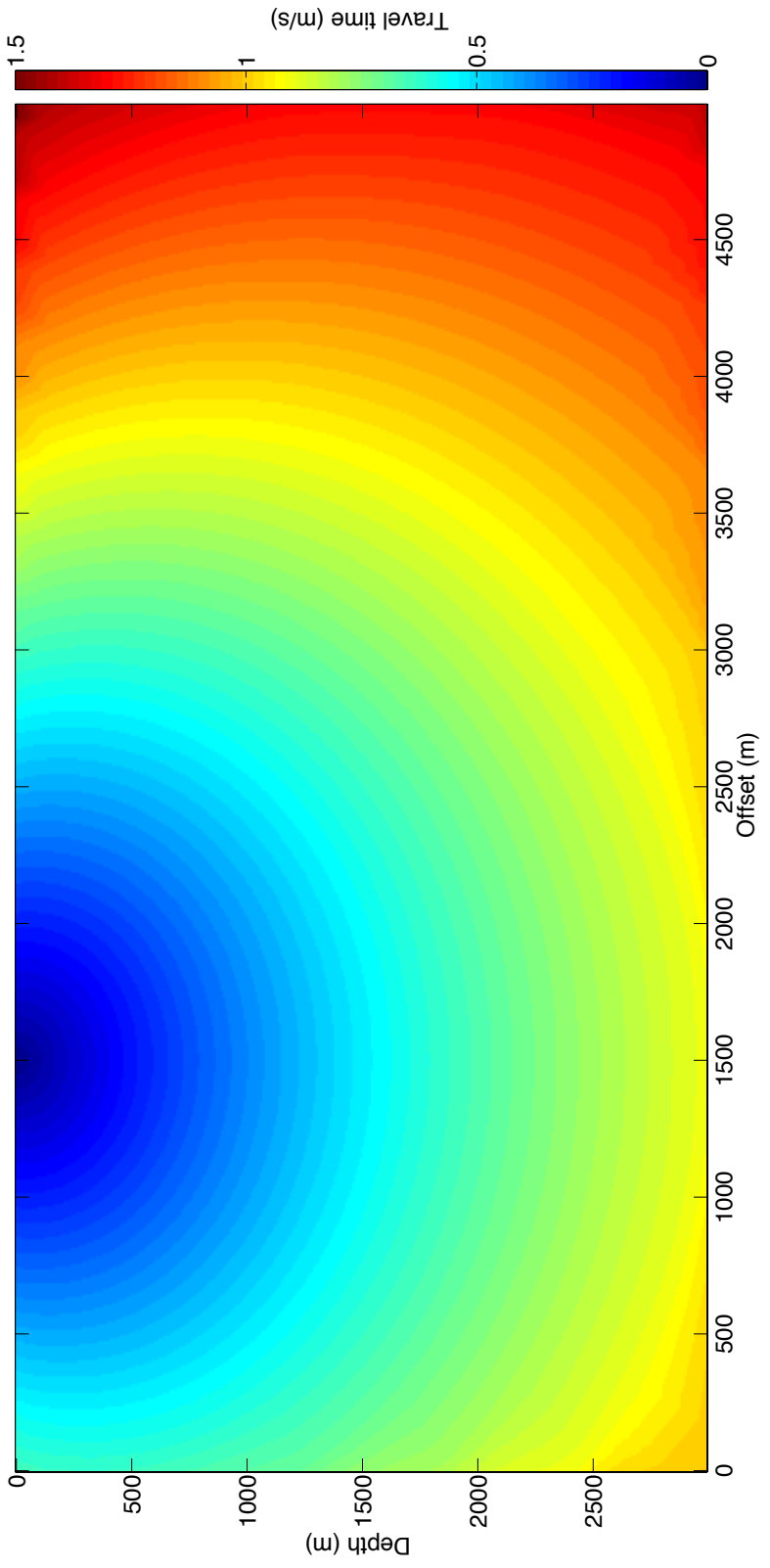

Figure 3.2: The traveltime to each grid point in the 1-D velocity model has been computed with the use of delauney interpolation after the raytracing.

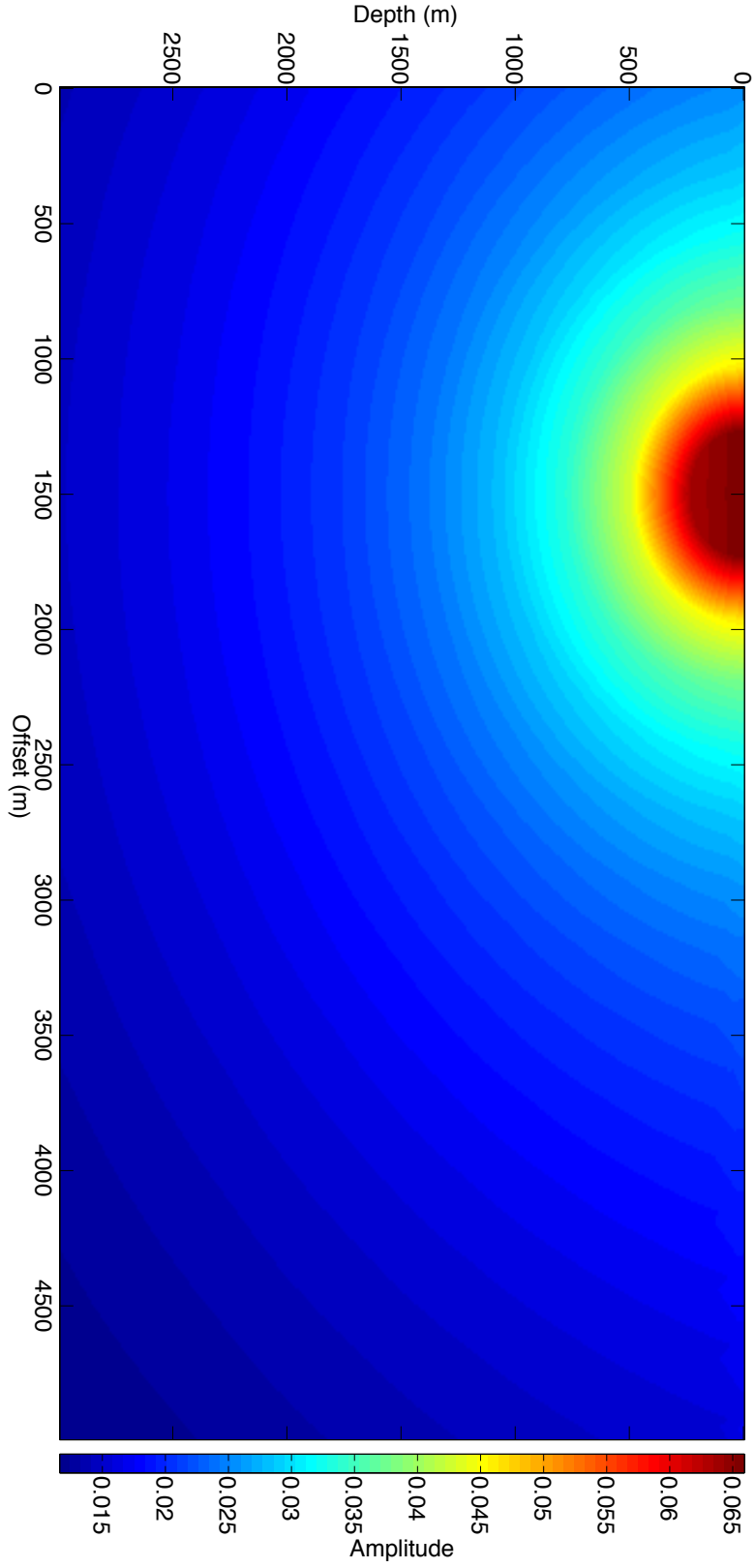

Figure 3.3: The amplitude to each grid point in the 1-D velocity model has been computed with the use of delauney interpolation after the raytracing.

$$p_1(\mathbf{x_s}, \mathbf{x_r}, \omega) = 2\omega^2 s(\omega) \int g_0(\mathbf{x_s}, \mathbf{x}, \omega) g_0(\mathbf{x_r}, \mathbf{x}, \omega) c_1(\mathbf{x}) c_0^{-3}(\mathbf{x}) d\mathbf{x}. \tag{3.8}$$

For each ω, the synthetic seismogram for the scatterers c_1 can be computed for all source/receiver pairs. When the synthetic seismogram for all ω has been computed, an inverse Fourier transformation can be performed. This will yield the time domain synthetic seismograms for all source/receiver pairs. It can be noted that it is possible to choose which $\mathbf{x}$ the synthetic seismogram is computed for. This means that it is possible to target a specific area or reflector in the model and compute the synthetic seismogram only for that area or reflector. This will reduce the computation time of the ray-Born approximation.

3.4 Finite Difference Method

The finite difference method is a method that is used to solve partial differential equations. Instead of finding the exact solution at any point in the function, one attempts to find an approximate solution at discrete points in the function. The second order central finite difference solution of the wave equation is computed by using the second order numerical derivative. The derivation of the second order numerical derivative follows Kincaid and Cheney (2002). Taylor expansion is performed on $f(x+h)$ and $f(x-h)$:

$$f(x+h) = f(x) + hf'(x) + \frac{h^2}{2} f''(x) + \frac{h^3}{3!} f'''(\xi) + \frac{h^4}{4!} f''''(\xi), \tag{3.9}$$

$$f(x-h) = f(x) - hf'(x) + \frac{h^2}{2} f''(x) - \frac{h^3}{3!} f'''(\xi) + \frac{h^4}{4!} f''''(\xi). \tag{3.10}$$

By adding one of these equations to the other and rearranging, we obtain the second order numerical derivative:

$$f''(x) = \frac{1}{h^2}\big[f(x+h) - 2f(x) + f(x-h)\big] - \frac{h^2}{12} f''''(\xi). \tag{3.11}$$

We assume that $h \to 0$, which results in $\frac{h^2}{12} f''''(\xi) \to 0$. Yielding the second order central finite difference:

$$f''(x) = \frac{1}{h^2}\big[f(x+h) - 2f(x) + f(x-h)\big]. \tag{3.12}$$

The equation is easily expanded into 2-D by adding another term:

$$f''(x,y) = \frac{1}{h^2}\big[f(x+h,y) - 2f(x,y) + f(x-h,y)\big] + \frac{1}{h^2}\big[f(x,y+h) - 2f(x,y) + f(x,y-h)\big]. \tag{3.13}$$

We can now replace $\frac{\partial^2 \mathbf{p}}{\partial t^2}$ with (3.13) in the wave equation (2.1) (e.g Youzwishen and Margrave (1999),

Geiger and Daley (2003), and Lehtinen (2003)):

$$\frac{p_{i,j}^{n+1} - 2p_{i,j}^{n} + p_{i,j}^{n-1}}{\Delta t^2 v^2} - \nabla^2 p_{i,j}^{n} = 0, \tag{3.14}$$

and rearrange the equation in order to find the pressure field for the next time step:

$$p_{i,j}^{n+1} = 2p_{i,j}^{n} - p_{i,j}^{n-1} + \Delta t^2 v^2 \nabla^2 p_{i,j}^{n}, \tag{3.15}$$

where

$$\nabla^2 p = \frac{p_{i+1,j}^{n} - 2p_{i,j}^{n} + p_{i-1,j}^{n}}{\Delta x} + \frac{p_{i,j+1}^{n} - 2p_{i,j}^{n} + p_{i,j-1}^{n}}{\Delta z}, \tag{3.16}$$

and $p_{i,j}^{n+1}$, $p_{i,j}^{n}$, $p_{i,j}^{n-1}$ are the pressure fields at the time steps $n+1$, n and $n-1$, Δt is the sampling frequency in time and $\Delta x, \Delta z$ is the grid spacing in the **x** and **z** direction. The accuracy of the finite difference solution of equation (3.15) depends both on the grid spacing Δx and the sampling rate Δt in order for the solution to be accurate. The advantage of the finite difference method is that the entire wave field will be computed accurately. The equation is solved iteratively for each time step Δt by first updating the pressure field and then inserting the amplitude at the nth element in the Ricker wavelet (2.4) , R^n at the source position $\mathbf{x_s}$. This is performed for as many time steps as needed. The entire wave field will be computed, including effects such as multiple scattering.

3.4.1 Absoring Boundary Conditions

One of the problems with the finite difference method is the boundaries of the model. When using the finite difference method, the wavefield will be reflected at the boundaries and back into the model. These reflections affect the synthetic seismograms and will create a systematic error in the seismograms. This problem is normally solved by expanding the boundaries and adding absorbing boundary conditions that absorb the energy and prevents it from being reflected back into the model. The choice that has been taken in this thesis is however to expand the boundaries so much that the reflections from the boundaries do not occur within the set recording time. This choice was taken as it is impossible for the absorbing boundary conditions to absorb all of the energy an some effect will still be seen at the synthetic seismograms. The solution taken in this thesis is therefore slower but more accurate than using absorbing boundary conditions.

3.5 Accuracy and Cost

When performing forward modelling it is essential that the result that is obtained is accurate and that the computation is as computationally inexpensive as possible. This section will discuss the accuracy of the ray-Born approximation and the finite difference method as well as how the computational cost changes for different modelling parameters.

3.5.1 Accuracy

There are several factors that decide whether or not the finite difference method will yield an accurate result. These factors are the grid spacing Δx and the time step Δt. In order for the finite difference method to remain stable the time step must satisfy the criteria shown in Lines et al. (1999):

$$\Delta t < \eta \frac{\Delta x}{v_{max}}, \tag{3.17}$$

where η is set as 0.3 and v_{max} is the maximum velocity of the velocity model. If the time step Δt exceeds this value the finite difference method will not be reliable and give inaccurate results. The gridspacing Δx must satisfy the criteria (e.g Alford et al. (1974)):

$$\Delta \mathbf{x} < \frac{v_{min}}{6 f_{max}}, \tag{3.18}$$

where v_{min} is the minimum velocity of the velocity model and f_{max} is the maximum frequency of the source wavelet. If the gridspacing Δx exceeds this value numerical dispersion will take place and the wavefield after a reflection will be distorted. Assuming that the time step and grid spacing is sufficiently small, the accuracy of the finite difference method is very high. It will effectively reproduce direct arrivals, reflections, refractions, diffraction, multiple scattering.

Assuming that the time step and grid spacing is sufficiently small, the ray-Born approximation will generally not be as accurate as the finite difference method. There are two reasons why this is not possible. The Green functions are computed in the background model, giving inaccuracy in the traveltime and amplitude from reflections from scatterers c_1. In addition the ray-Born approximation only computes first order scattering and not multiple scattering. This means that the ray-Born approximation will not reproduce the full wavefield and can therefore not be completely accurate.

3.5.2 Cost

The criteria for the time step (3.17) and gridspacing (3.18) can be used to say something about the computation time of the finite difference method. If the maximum frequency of the source wavelet was increased by a factor of two, the gridspacing Δx would have to be halved in order to avoid numerical dispersion. In a 2-D model this would result in an increase of grid points by a factor of four. In a 3-D model this would increase the number of grid points by a factor of eight. As the time step is also dependent on the grid spacing Δx, the time step Δt would need to be halved. This means that increasing the maximum frequency of the source wavelet by a factor of two would result in an increase of computation time of a factor of eight in a 2-D model and a factor of 16 in a 3-D model. The significant increase in computation time with increasing frequency sets limits the maximum frequency that we can use in forward modelling.

The ray-Born method is less strictly dependent on these criteria than the finite difference method.

The raytracing does not need to be performed in the exact velocity model, but can be performed in a coarse model with larger grid spacing. The ray paths can be computed in a coarse model with larger grid spacing because the velocity and direction of the ray path is determined through linear interpolation along the ray path. The accuracy of interpolation should not decrease unless the velocity model is very complex. When all the ray paths are computed, the traveltime and amplitude can be interpolated onto a denser grid that is used with the ray-Born approximation. The raytracing is the computationally most expensive part of the ray-Born approximation and performing raytracing on a coarser grid will therefore greatly reduce the cost. Another advantage of the ray-Born approximation is that it is possible to target a specific part of a model and generate synthetic seismograms for only that area. This allows for very fast forward modelling for small target areas. These advantages allow for a quicker solution of the wave equation when using the ray-Born approximation compared to the finite difference method, especially for larger models with a high cost. Although the ray-Born approximation has a lot of advantages compared to the finite difference methods it also has a drawback. When using the ray-Born approximation we have to compute the Green function for all the sources and all the receivers. When using the finite difference method we only have to solve for the sources. If we have very many receivers relative to the number of sources the ray-Born approximation might be a bit slower than the finite difference method. This is because when using the ray-Born approximation we need to compute the Green functions for all of the receivers, while when using the finite difference method we only have to consider the sources. The computation time of the the finite difference method is given as a function of number of sources and number of grid points:

$$C_{fd} = f(n_s, n), \tag{3.19}$$

where C_{fd} is the computation time of the finite difference method, n_s is the number of sources and n is the number of grid points. The computation time of the ray-Born approximation is given as a function of the number of sources, number of receivers, number of grid points and a factor ξ that is dependent on the roughness of the raytracing model.

$$C_{rb} = f(n_s, n_r, n, \xi), \tag{3.20}$$

where C_{rb} is the computation time of the ray-Born approximation and n_r is the number of receivers.

3.6 Models

In this section we will discuss the different models that have been used in this thesis. The three basic models that have been chosen are a model with a single Gaussian scatterer, a layered medium and a random Gaussian medium. Each of the three basic models are evaluated using a constant velocity background model and a 1-D linearly increasing velocity model. In addition to the basic models, the accuracy of the ray-Born approximation is evaluated for one complex velocity model resembling an overthrust fault. Modelling will be performed for each of the three basic models with a velocity

contrast from the background model of 23 m/s to 230 m/s. The velocity contrasts were defined as one to ten percent of the constant velocity background model. This velocity contrast will hereafter be referred to as the perturbation strength.

3.6.1 Background Models

In order to reproduce the scatterers from the three basic scattering models, two different background models have been used. The first background model is a constant velocity model that can be seen in figure 3.4. The second background model is a 1-D linearly increasing velocity model shown in figure 3.5. In each of the figures the source position is marked with a red cross and the receiver array marked with a green cross. This also holds for all models shown in this thesis. When performing forward modelling in the 1-D background model it is expected that the accuracy of the ray-Born approximation relative to the finite difference method is less accurate than in the constant background velocity model. The reason for this is that in the constant background velocity model the ray paths will be straight and it is therefore possible to compute the exact traveltime and amplitude for each grid point when using the Born approximation. The Green function used for the 1-D background velocity model is not exact but approximate. Doing this comparison with the same scatterer and two different background models will show us how much the background model will affect the results from the ray-Born approximation. It will give us an idea on whether or not the ray-Born approximation is an alternative to the finite difference method in seismic exploration as well as acoustics oceanography.

3.6.2 Gaussian Model

The first model is a model with a Gaussian scatterer. The Gaussian model has been generated using the following formula:

$$m = c_1 \, e^{-\frac{\mathbf{r}^2}{r_0^2}}, \tag{3.21}$$

where c_1 is the maximum amplitude of the Gaussian, r_0 is the radius of the Gaussian and $\mathbf{r}$ is given as:

$$\mathbf{r} = \sqrt{\lambda_x (x - x_1)^2 + \lambda_z (z - z_1)^2}. \tag{3.22}$$

x and z is the position, x_1 and z_1 is the centre position of the Gaussian and λ_x and λ_z define the shape of the Gaussian. Forward modelling for this model is performed for perturbation strengths (c_1) ranging from 23 m/s to 230 m/s. In figure 3.6 the model is plotted with a maximum perturbation strength of 230 m/s. In figures 3.7 and 3.8 the relative difference between the scatterer and the two background models can be observed. The maximum relative difference is 10 percent in the constant velocity background model and 7.5 percent in the 1-D velocity background model. The model is designed to see how well the ray-Born approximation could reproduce the wavefield caused by a single small and smooth scatterer relative to the finite difference method. This is the most basic model in

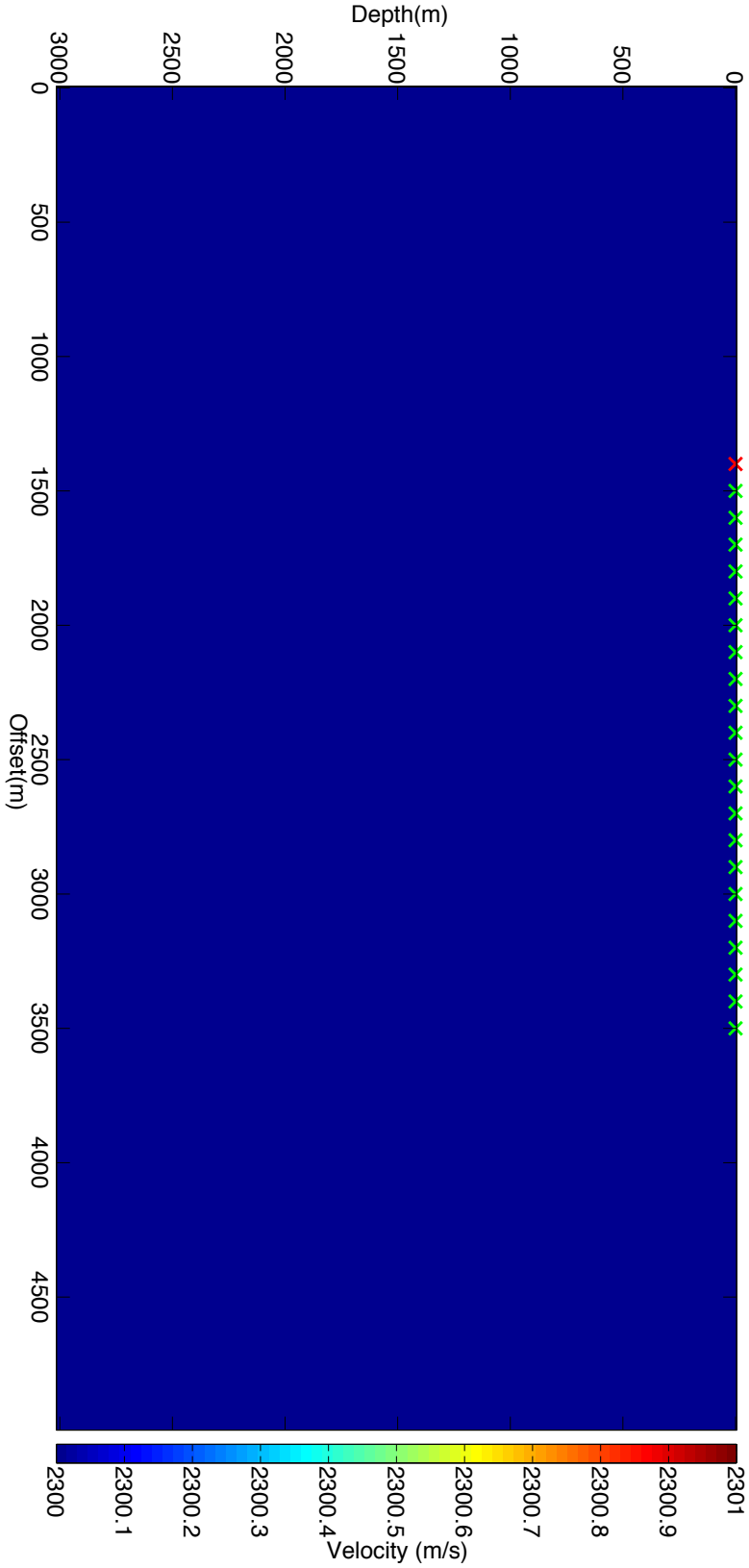

Figure 3.4: Constant background Velocity Model

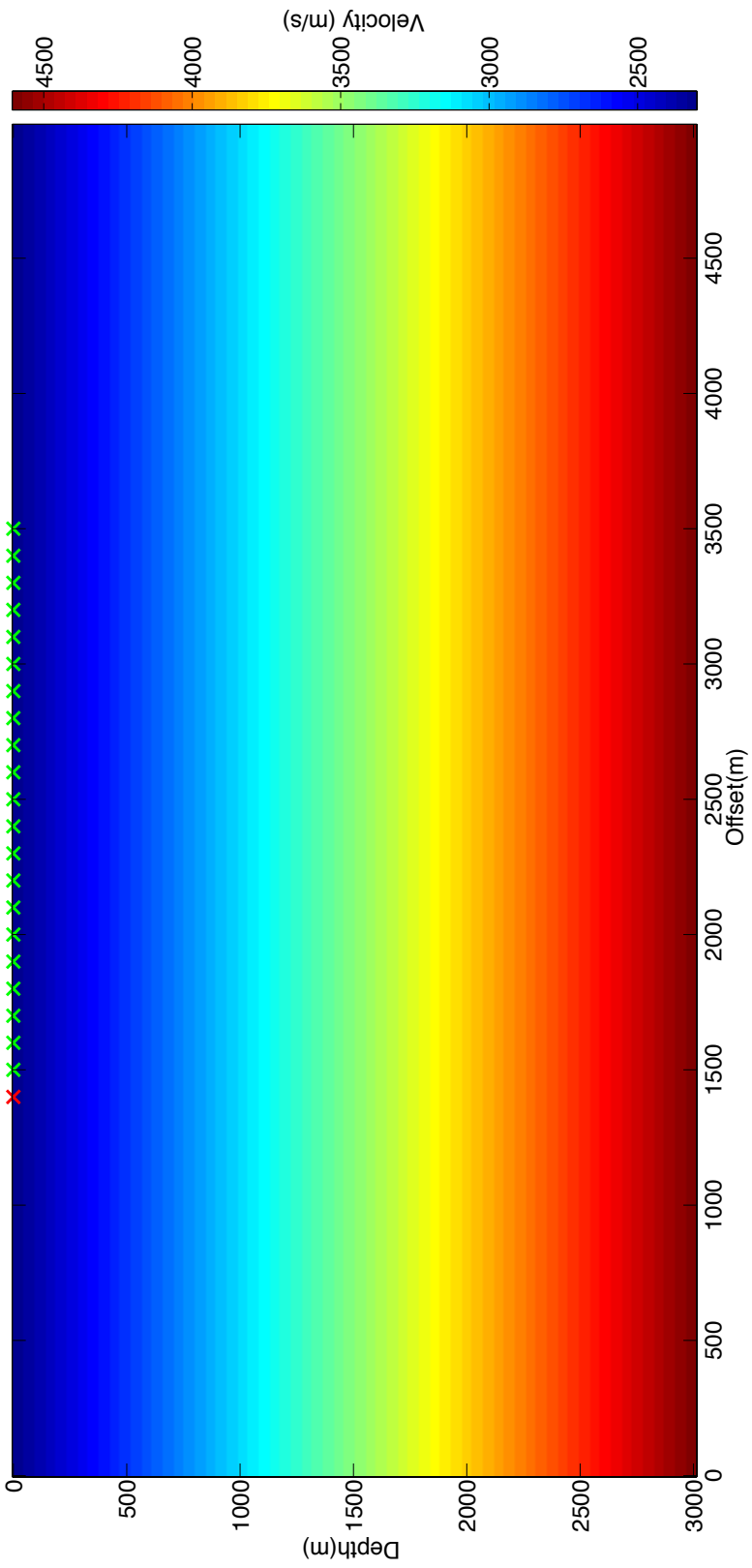

Figure 3.5: 1D background Velocity Model

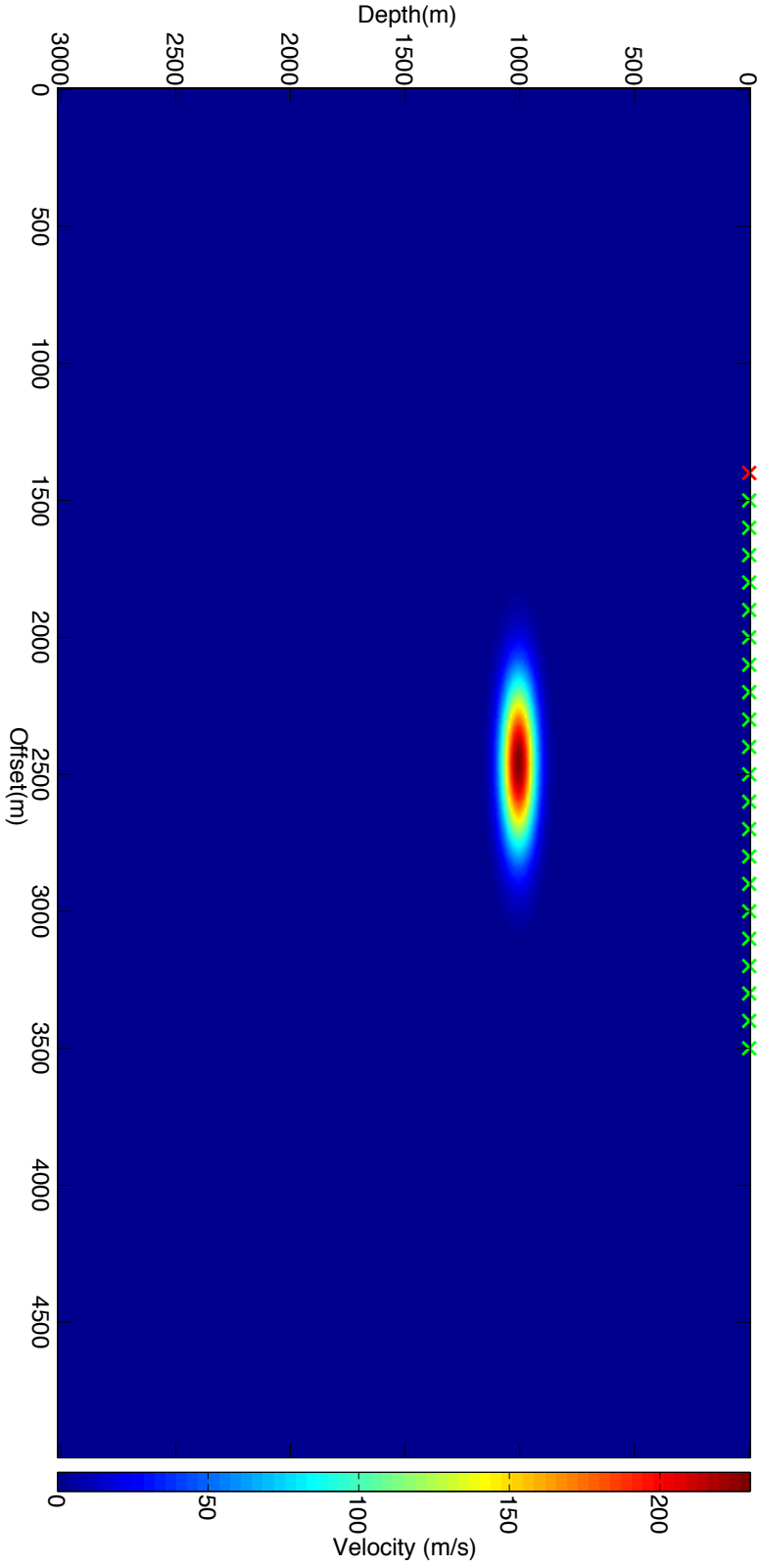

Figure 3.6: Velocity model with a single Gaussian scatterer

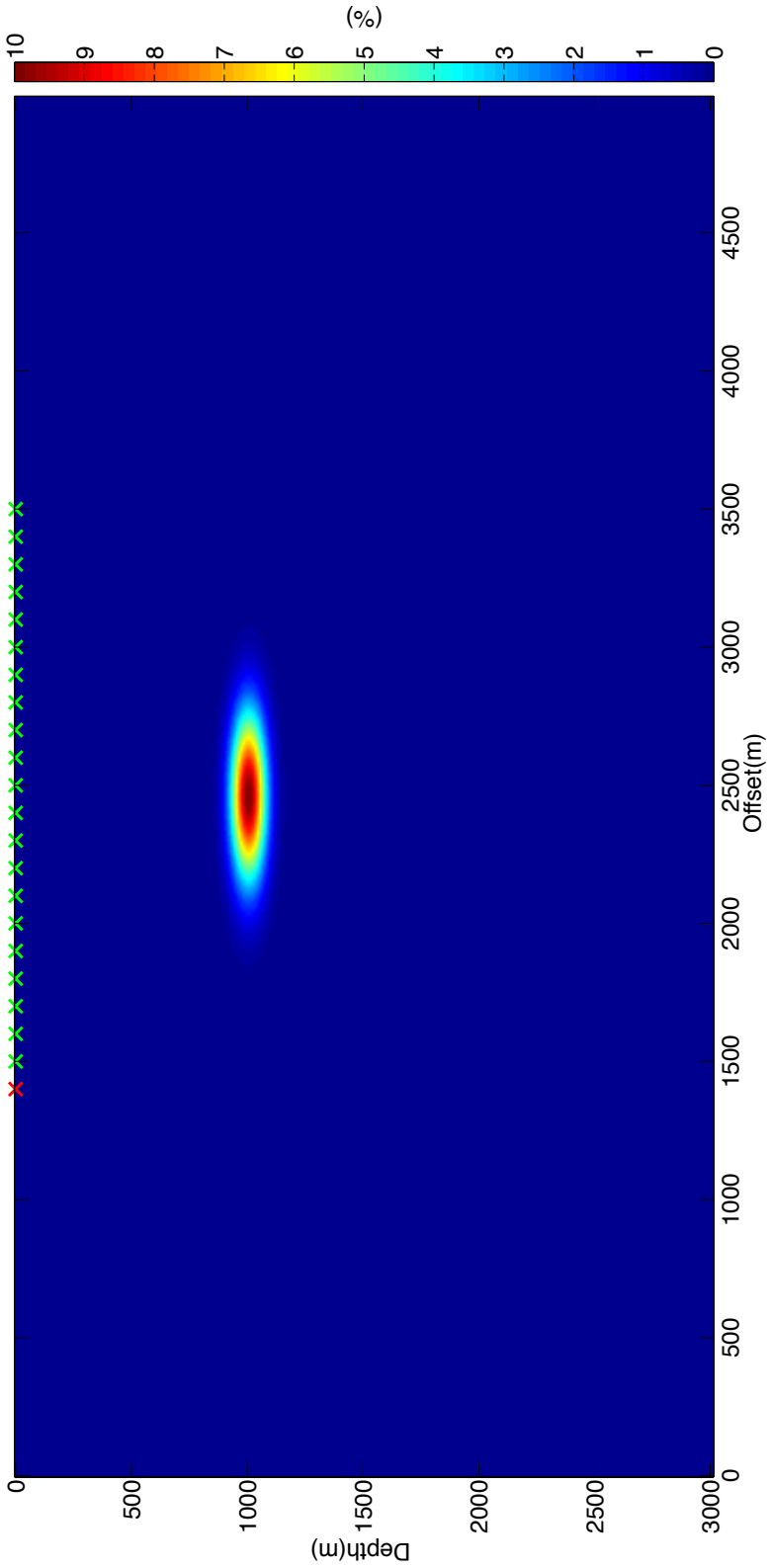

Figure 3.7: Relative difference between the constant velocity background model and the Gaussian scatterer

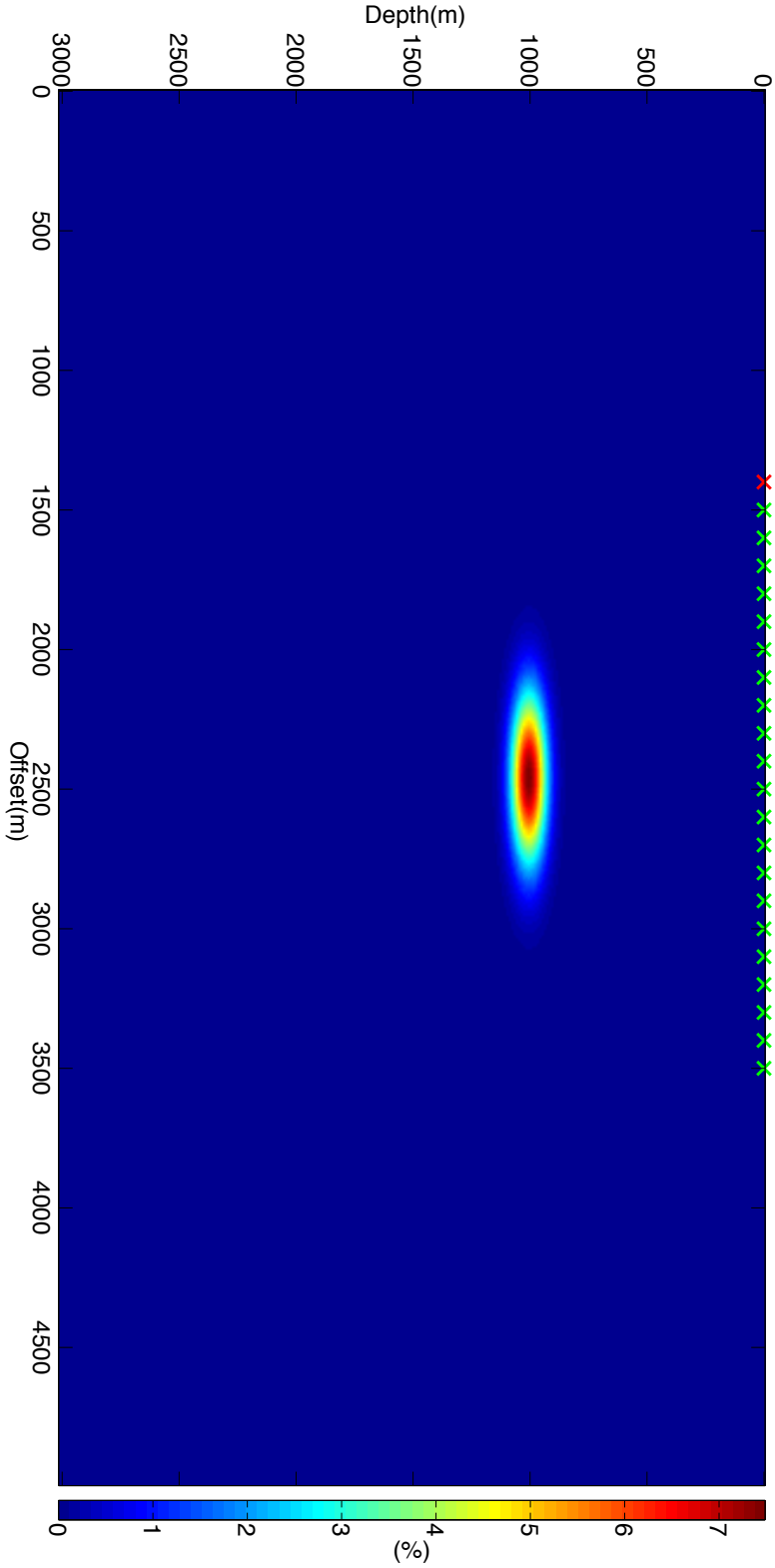

Figure 3.8: Relative difference between the 1-D velocity background model and the Gaussian scatterer

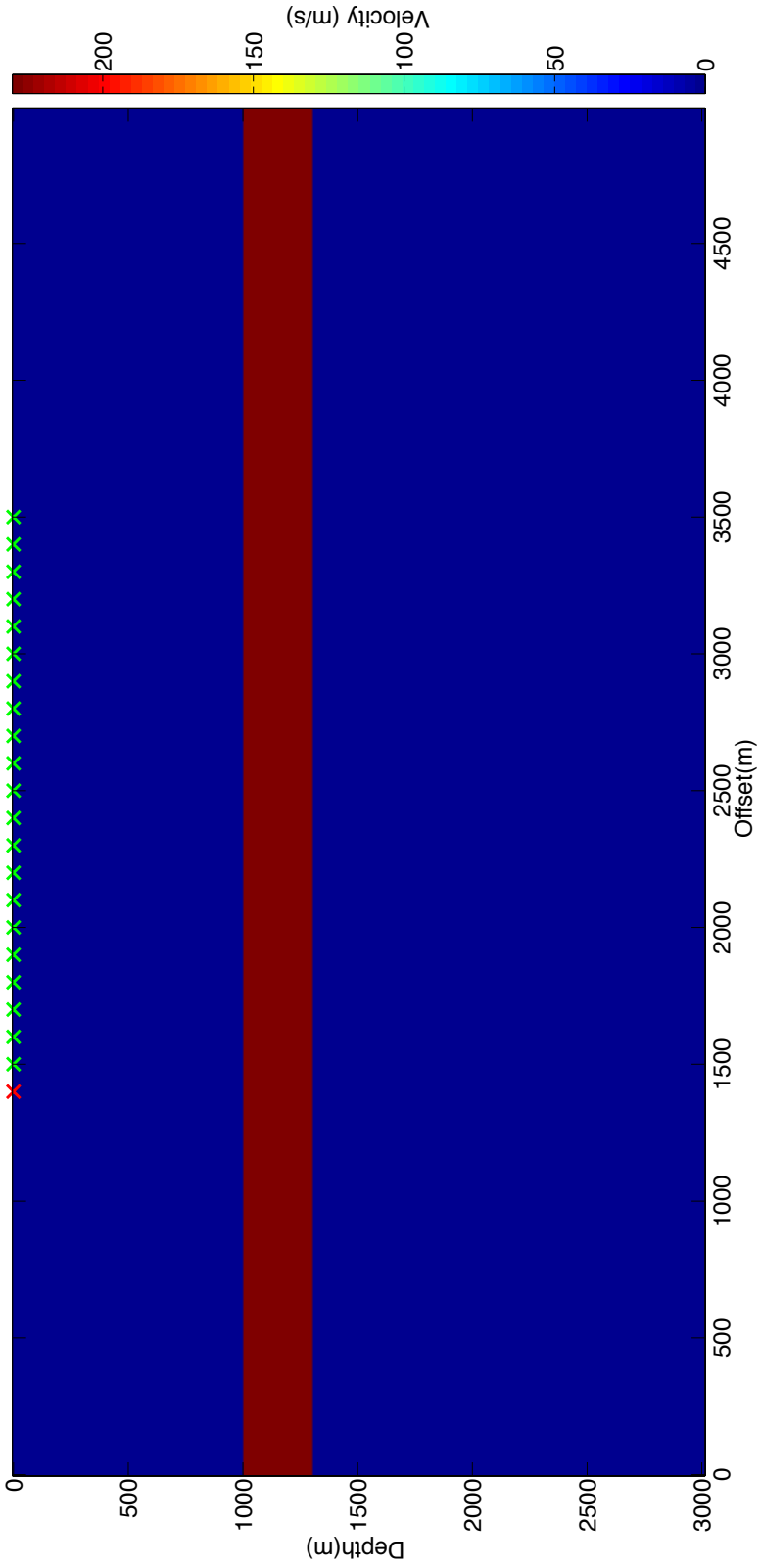

Figure 3.9: A velocity model with a layer

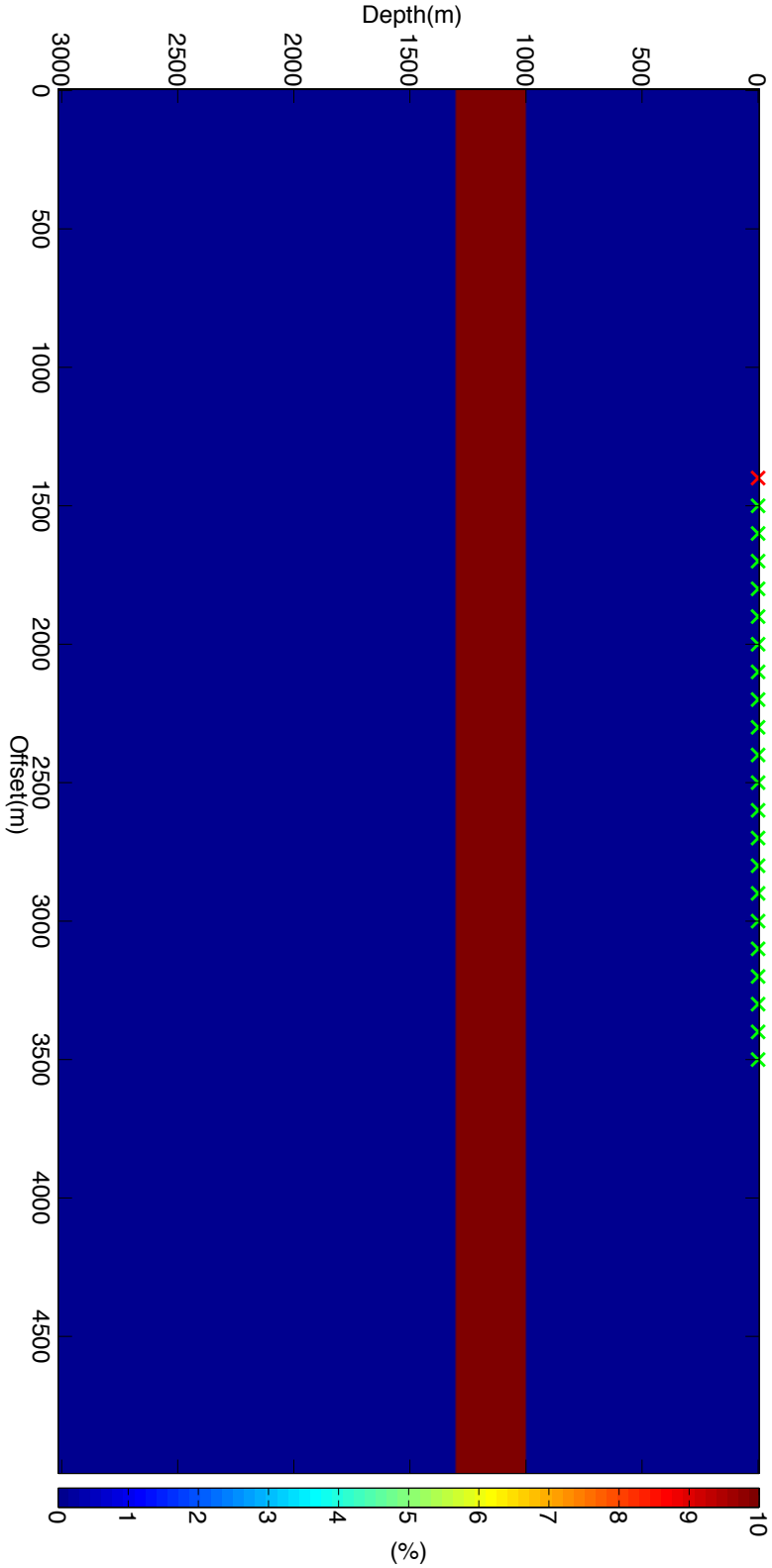

Figure 3.10: Relative difference between the constant velocity background model and velocity model with a layer

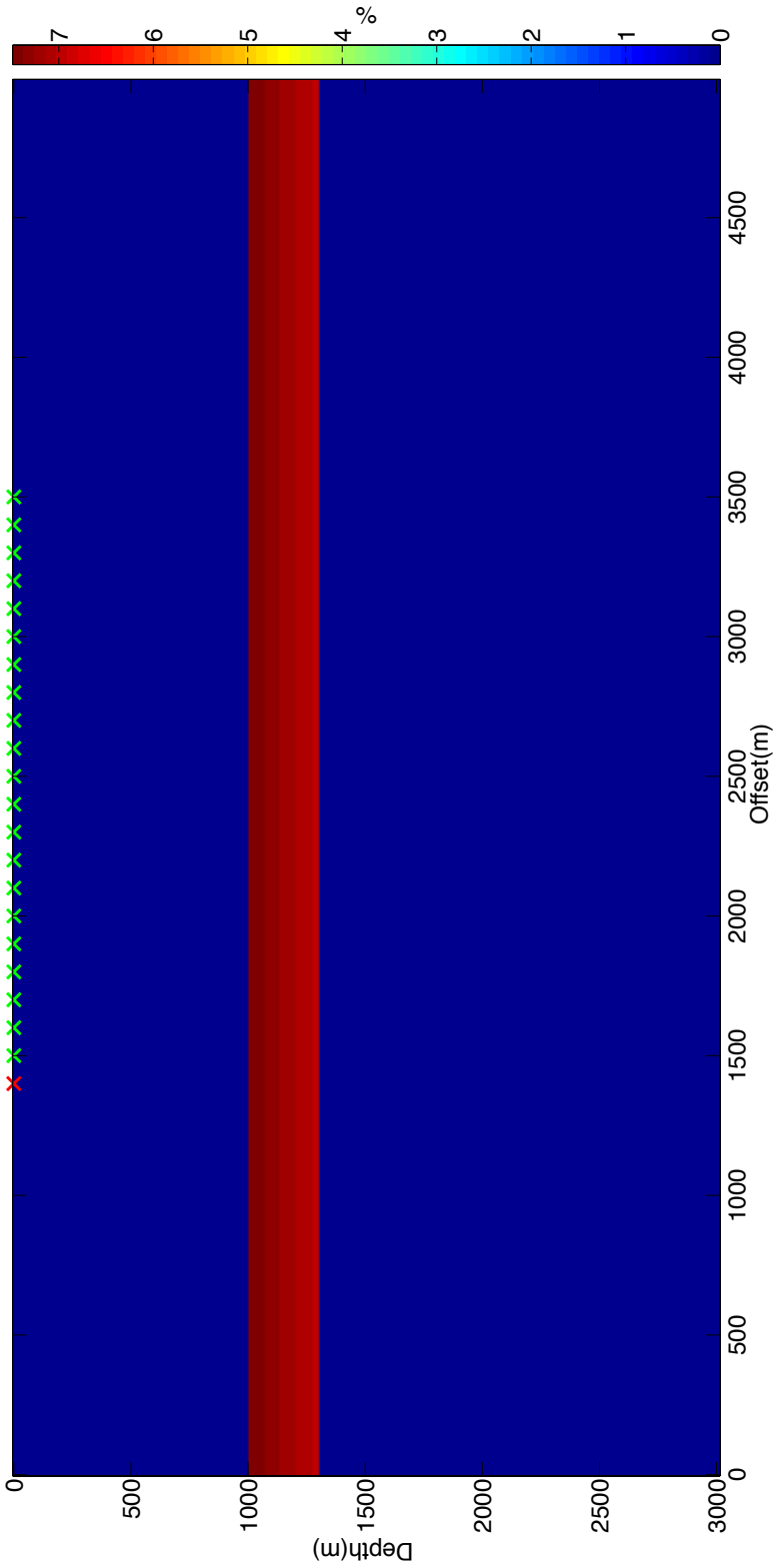

Figure 3.11: Relative difference between the 1-D velocity background model and velocity model with a layer

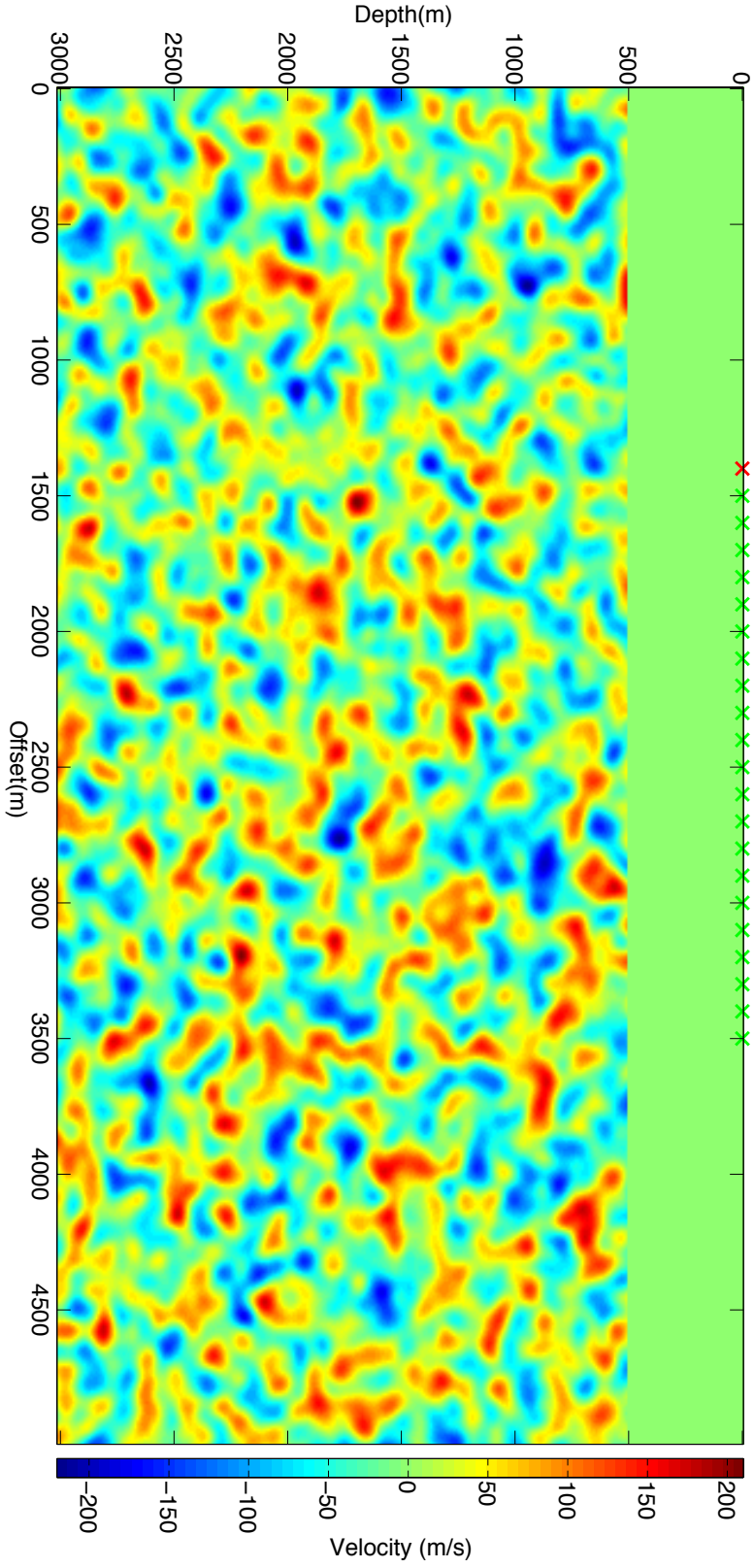

Figure 3.12: Velocity model with a random Gaussian media with a correlation length of 50 m

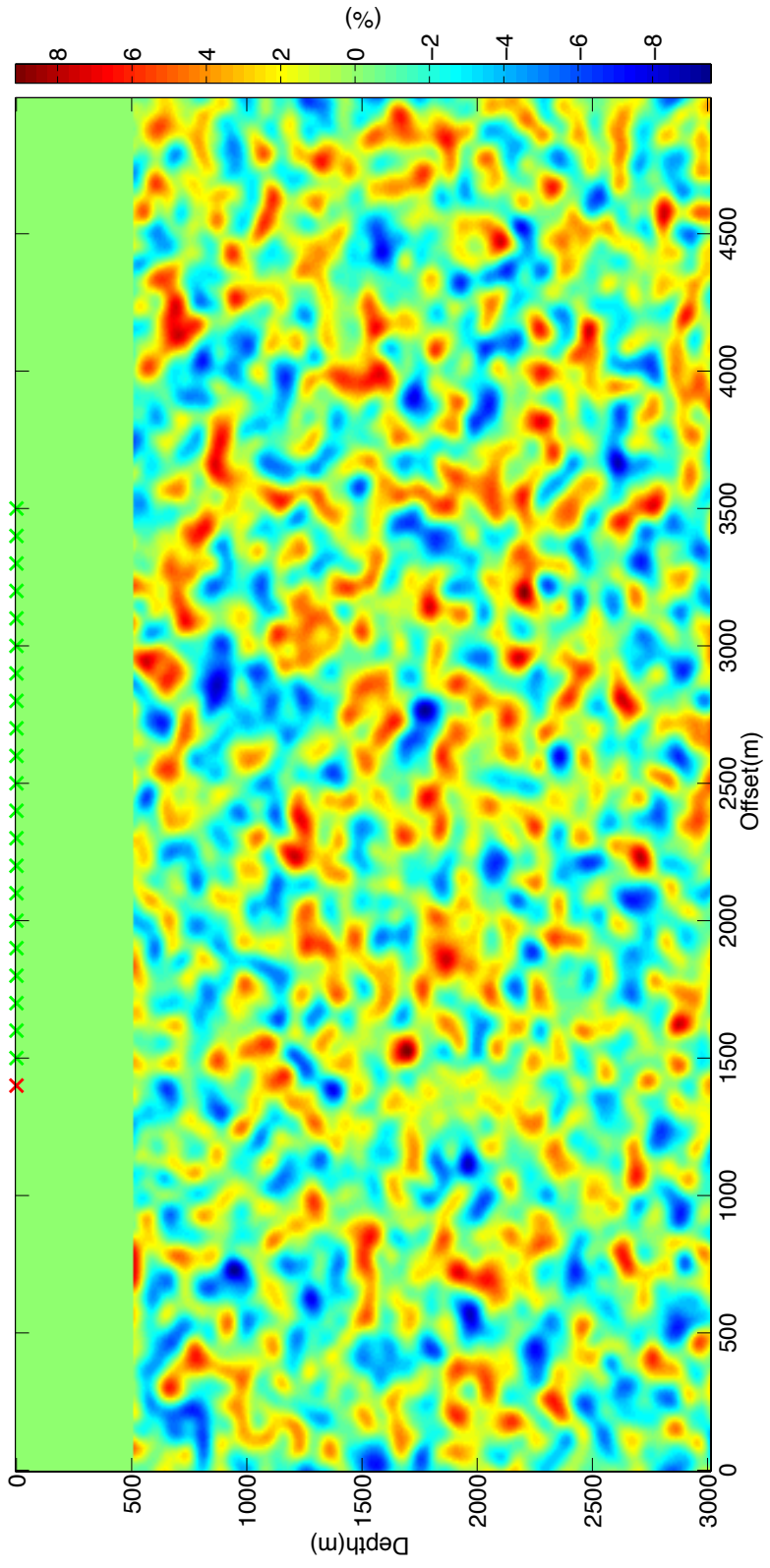

Figure 3.13: Relative difference between the constant velocity background model and the random Gaussian media with a correlation length of 50 m

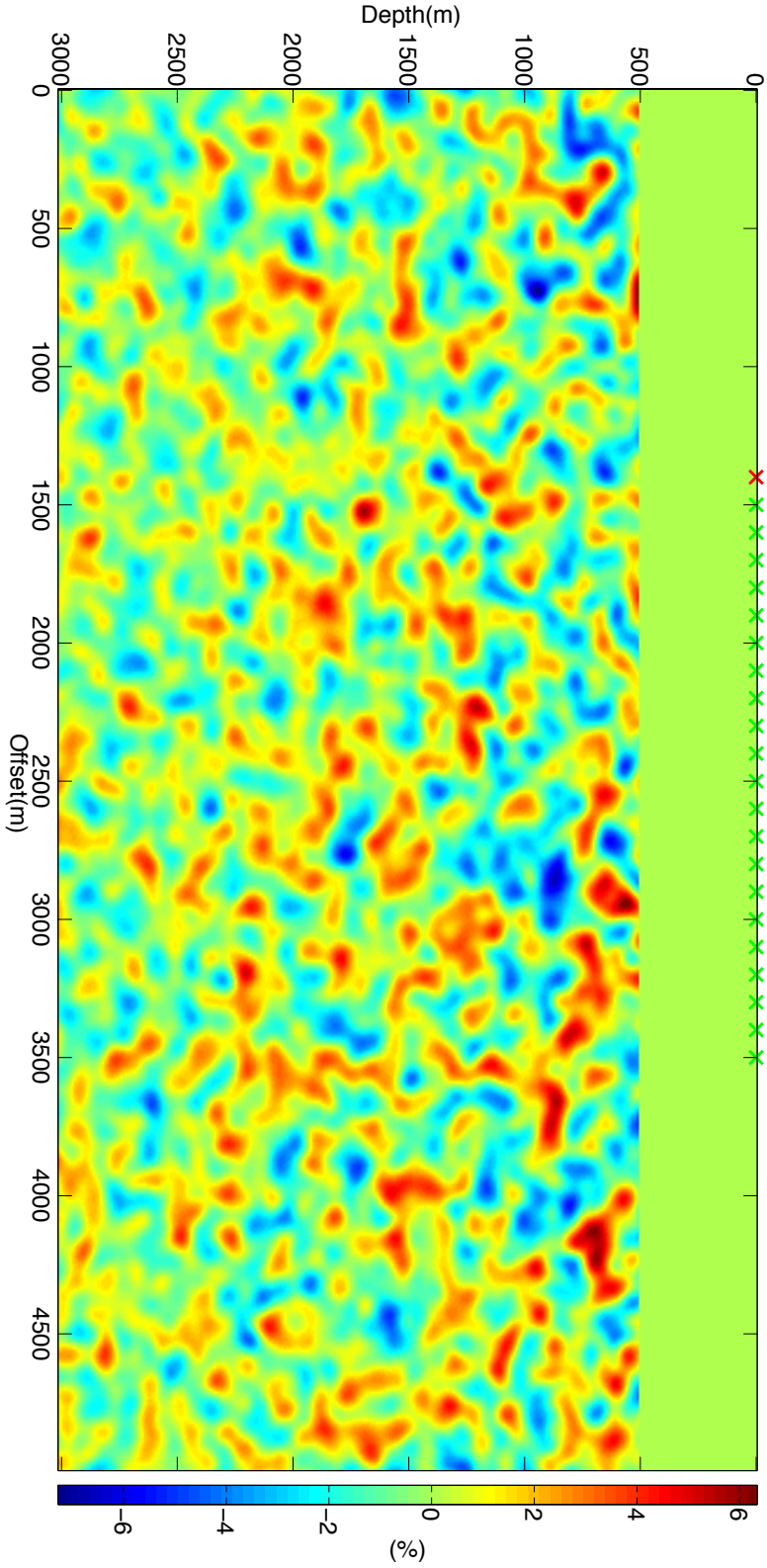

Figure 3.14: Relative difference between the 1-D velocity background model and the random Gaussian media with a correlation length of 50 m

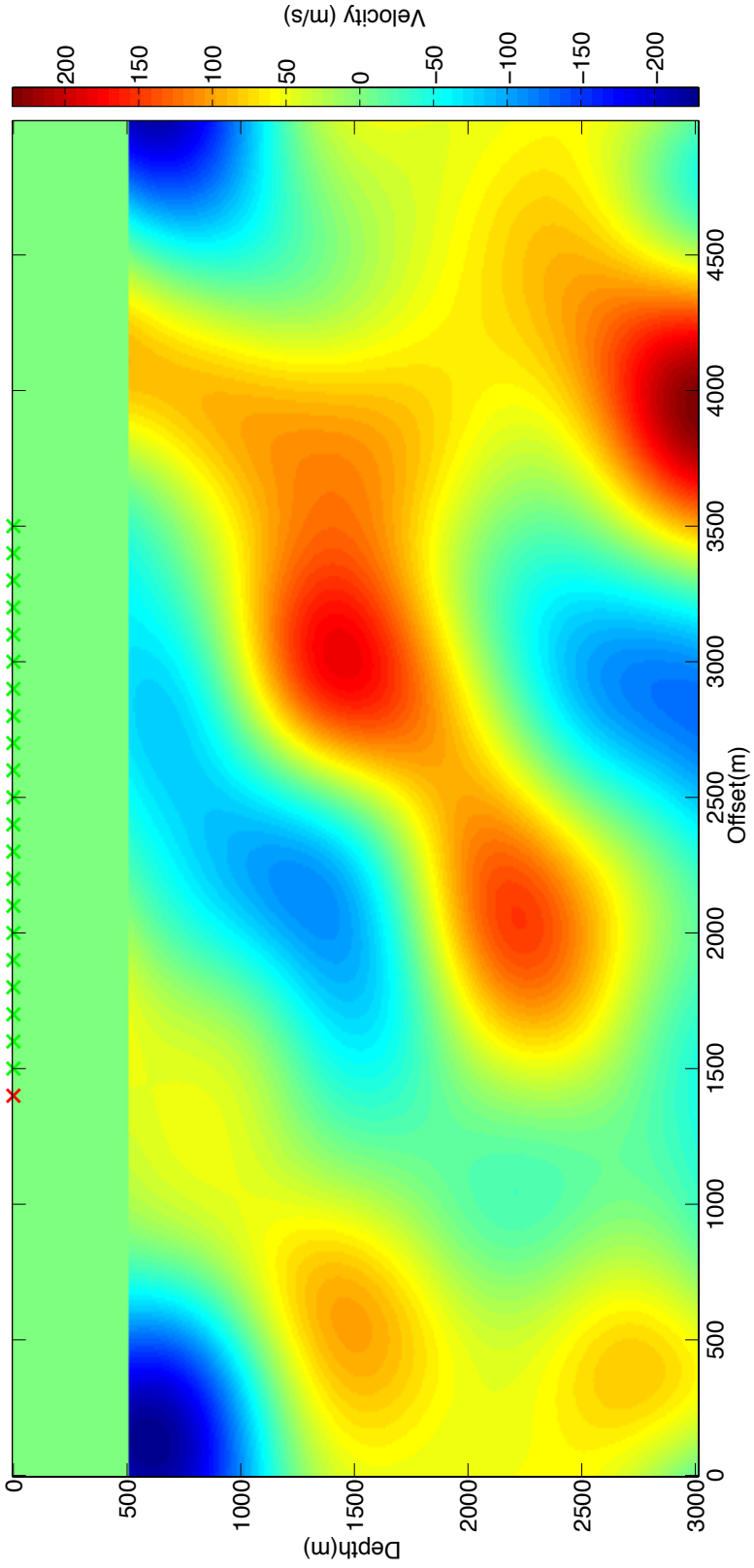

Figure 3.15: Velocity model with a random Gaussian media with a correlation length of 500 m

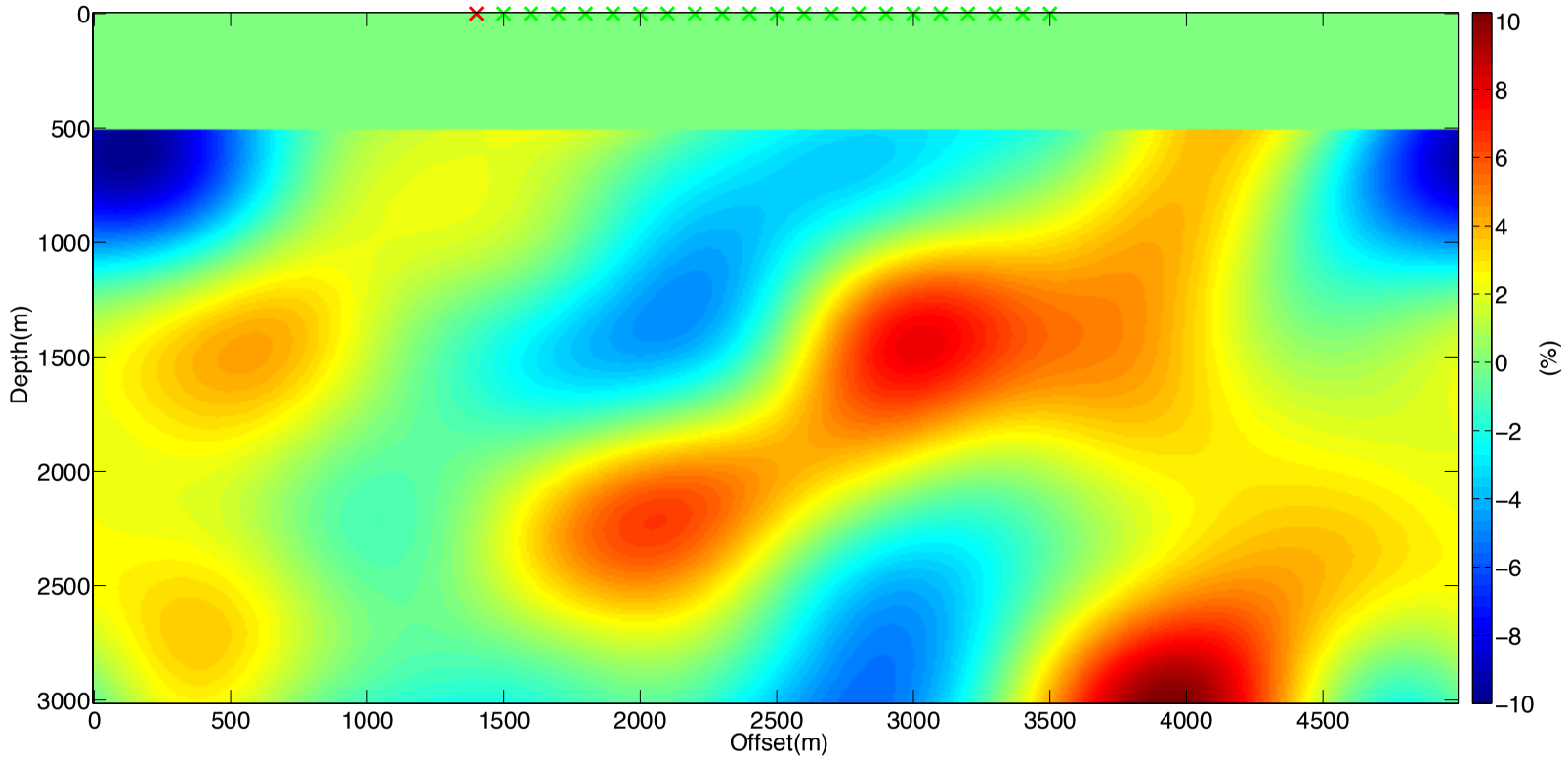

Figure 3.16: Relative difference between the constant velocity background model and the random Gaussian media with a correlation length of 500 m

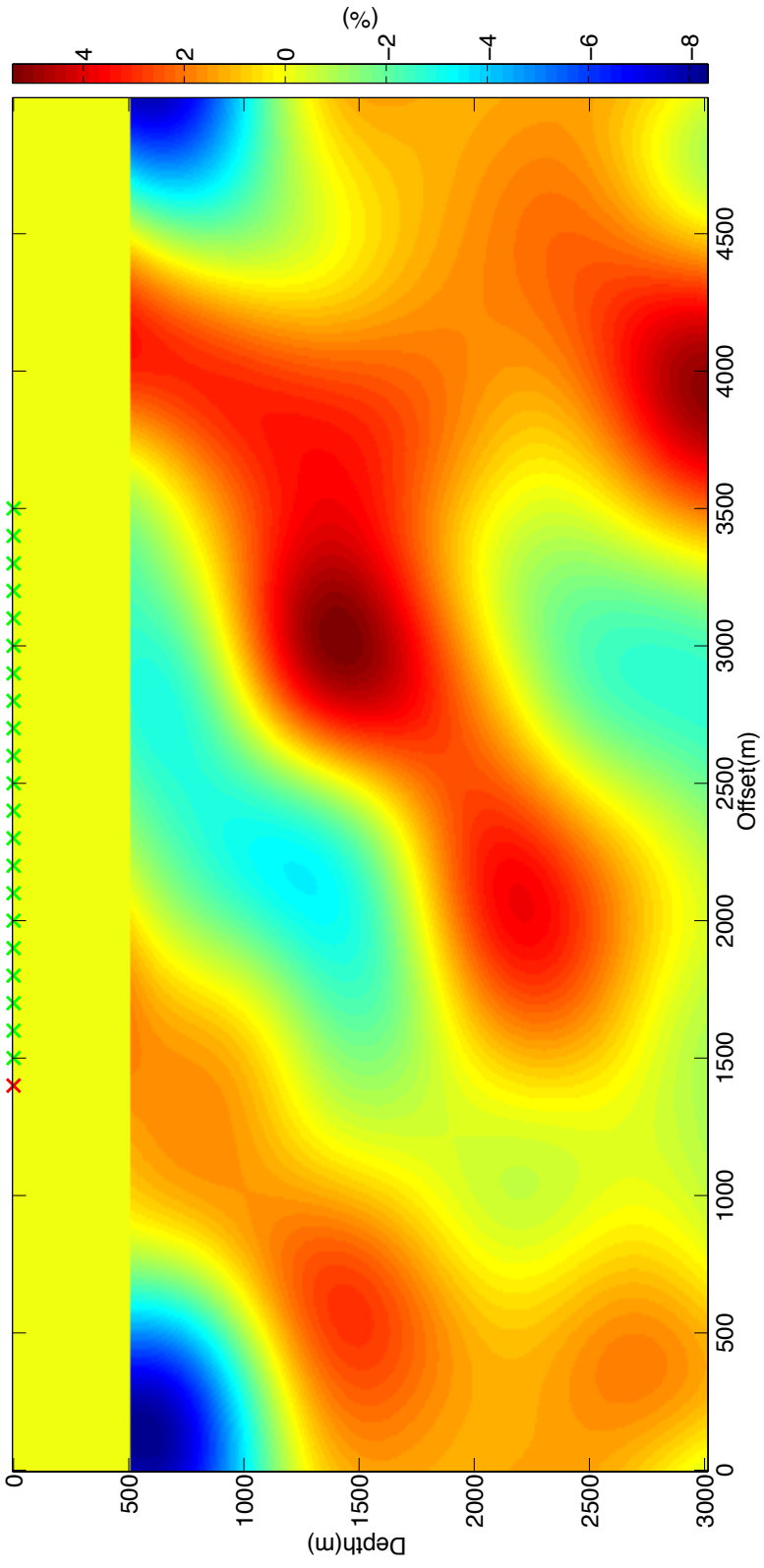

Figure 3.17: Relative difference between the 1-D velocity background model and the random Gaussian media with a correlation length of 500 m

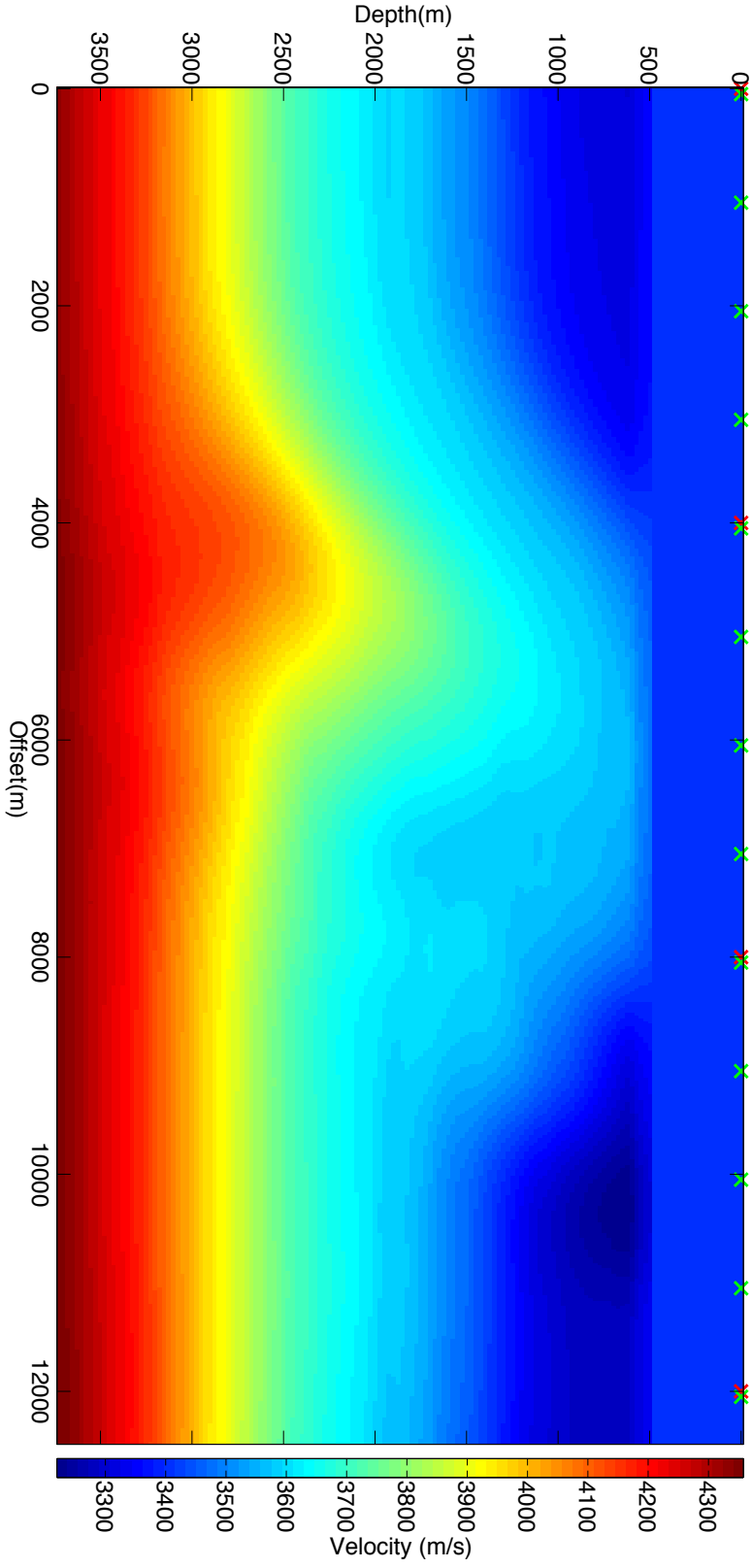

Figure 3.18: Background model for the SEG/EAGE Overthrust model from Aminzadeh et al. (1997)

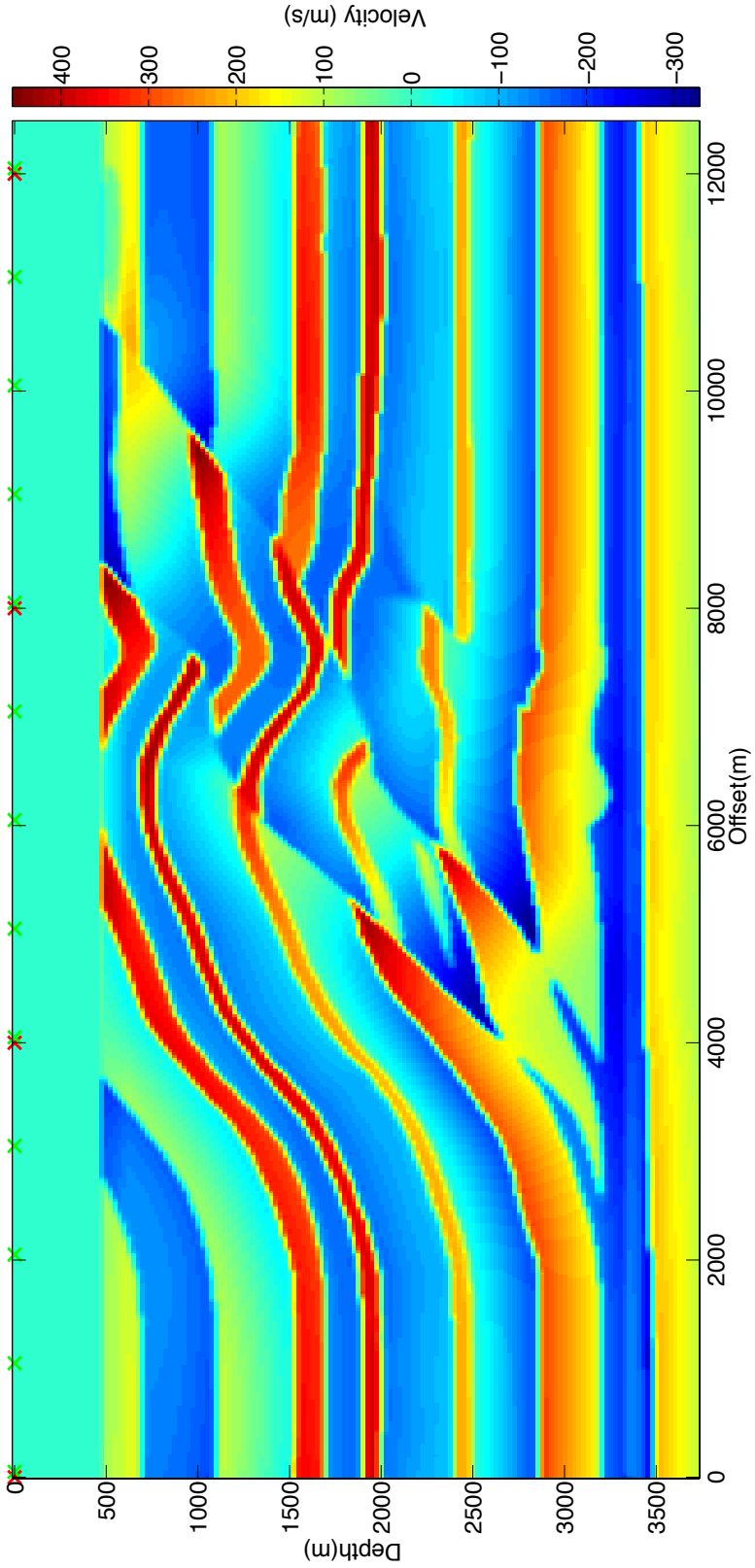

Figure 3.19: Scatterer for the SEG/EAGE Overthrust model from Aminzadeh et al. (1997)

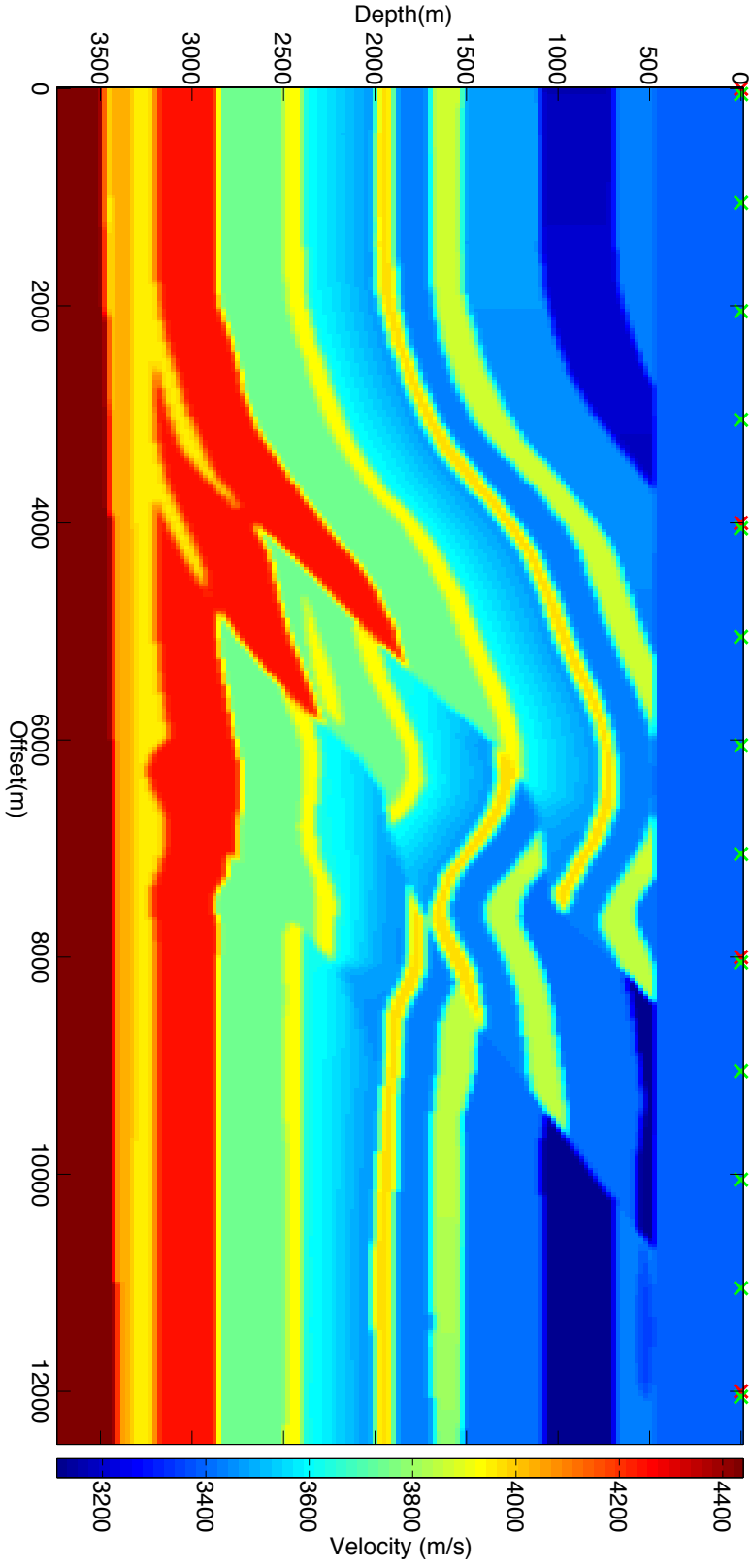

Figure 3.20: SEG/EAGE Overthrust model from Aminzadeh et al. (1997)

the thesis and it is therefore expected that the results from the ray-Born approximation will be very close to the results from the finite difference method for this model. The model will therefore only produce one reflection and no multiple scattering.

3.6.3 One-Layer Model

The second model is a model with a sharp discontinuous layer. Forward modelling for this model is performed for perturbation strengths ranging from 23 m/s to 230 m/s. The velocity model is plotted with a perturbation strength of 230 m/s in figure 3.9. In figures 3.10 and 3.11 the relative difference between the one-layer model and the two background models can be observed. The maximum relative difference is 10 percent in the constant background velocity model and 7.5 percent in the 1-D background velocity model. The model was designed for two different purposes. The first purpose was to see how well the ray-Born approximation can reproduce reflections from sharp interfaces. The second purpose was to identify how much the reflection from the lower boundary of the layer is timeshifted when using the ray-Born approximation relative to the finite difference method. The ray-Born approximation is expected to accurately reproduce the reflection from the upper boundary of the layer, while the reflections from the lower boundary are shifted in time. The timeshift from the lower boundary is expected to increase with increasing perturbation strength.

3.6.4 Random Gaussian Model

The third model is a model that has been generated with a Gaussian correlation function that is presented in Baig and Dahlen (2004) as:

$$m(||\mathbf{x}-\mathbf{x}'||) = \epsilon^2\sigma^2 \exp^{-\frac{||\mathbf{x}-\mathbf{x}'||}{a^2}}, \tag{3.23}$$

where ϵ is the RMS strength of the heterogeneity given as:

$$\epsilon = \frac{\delta\sigma^2(\mathbf{x})}{\sigma^2}. \tag{3.24}$$

a is the correlation length, which determines the distance between two uncorrelated points, ϵ is the slowness of the background velocity model c_0 and $\delta\sigma$ is the slowness of the scatterer. Forward modelling for this model is performed for perturbation strengths ranging from 23 m/s to 230 m/s. Models have been created with increasing correlation length from 50 to 500 m. In figure 3.12 a Gaussian medium with a correlation length of 50 m and a perturbation strength of 230 m/s is plotted. In figure 3.13 and 3.14 the relative difference between the model and the two background models can be observed. The maximum relative difference is 10 percent in the constant background velocity model and 7.5 percent in the 1-D background velocity model. In figures 3.15 a Gaussian medium with a correlation length of 500 m and a perturbation strength of 230 m/s has been plotted. In figure 3.16 and 3.17 the relative difference between the model and the two background models can be observed. The maximum relative difference is 10 percent in the constant background velocity model and 8 percent in the 1-D background

velocity model. These models have been used for several reasons. The first reason is the possibility to see if the second order scattering produced by the finite difference method has a significant effect on the relative difference between the ray-Born approximation and the finite difference method. It is expected that significant second order scattering will be observed at higher perturbation strengths while almost no second order scattering will be observed at low perturbation strengths. The second reason is to observe how the size of the scatterer will influence the error of the ray-Born approximation relative to the finite difference method. The larger scatterers will result in greater timeshifts, especially at higher perturbation strengths.

3.6.5 Overthrust Model

The fourth model is a 2-D slice of the SEG/EAGE 3-D overthrust model from Aminzadeh et al. (1997). Due to the fact that the raytracer used in this thesis does not compute amplitudes accurately in the case of multipathing, the SEG/EAGE Overthrust model has been slightly modified in order to reduce the multipathing effects. The model consists of a smoothly varying background model that shown in figure 3.18 and a scatterer seen in figure 3.19. The sum of the background model and the scatterer becomes the overthrust model seen in figure 3.20. The background velocity model increases very smoothly with depth. Towards the centre of the model the velocity is higher and the velocity increases more with depth. Due to the variations in the background model, multipathing will exist for larger offset and the amplitudes and traveltimes that are computed will not be correct in areas with multipathing. The scatterer is very complex with layers of varying thicknesses, perturbation strengths and dip. The relative velocity difference to the background model is roughly 10-15 percent with a maximum of 20 percent. It is expected that multipathing and second order scattering will make it difficult for the ray-Born approximation to give accurate results for the entire model.

3.7 Results

In this section we will for the two background models and the four scattering models discussed in the previous section perform a comparison between the finite difference method and the ray-Born approximation. The comparison consists of comparing the synthetic seismograms generated by raytracing and the ray-Born approximation with the synthetic seismograms generated by the finite difference method. The difference between the methods will be evaluated using the RMS (root mean square) error given as:

$$\epsilon_{rms} = \sqrt{\frac{\sum_{t=0}^{n}(x_{1,t} - x_{2,t})^2}{n}}, \tag{3.25}$$

where $x_{1,t}$ and $x_{2,t}$ are two time series and n is the number of samples in each time series. The comparison is performed for centre frequency of the source wavelet between 5 and 15 Hz. For each frequency, perturbation strength and offset, the RMS (root mean square) error of each trace will be computed in order to evaluate how these parameters affect the accuracy of the ray-Born approximation.

In order to increase the accuracy of the RMS error ϵ_{rms} computation and accurately evaluate the error of the ray-Born approximation a few adjustments have been made. The first adjustment scales the synthetic seismograms so that the maximum amplitude of each trace is equal to one. This scaling is performed for several reasons: The first reason is that higher perturbation strengths will create stronger reflections than weak perturbation strengths. Stronger reflections will create larger error between the ray-Born approximation and the finite difference method even if the relative difference between the methods do not change. With the scaling it is possible to compare the relative difference between the methods for different perturbation strengths. The second reason is that due to geometrical spreading, the amplitude will be lower at higher offset than at low offset. The error can therefore be seen as less at higher offset, while the relative difference between the methods is higher. The second adjustment that has been taken is that only the nonzero values of the traces have been used when computing the RMS error. The reflections are longer in time for low frequencies than for high frequencies. If we were to select the whole trace, the low frequency source wavelets would have less zeroes than high frequencies and would therefore show higher error than high frequencies while the relative difference was less.

3.7.1 Direct Arrival

A seismic trace consists of the direct arrival u_0 and a scattered arrival u_1 where $u = u_0 + u_1$. Before we attempt to compare the scattered arrivals u_1 computed by the ray-Born approximation and the finite difference method we need to do a comparison between the direct arrival produced by raytracing and the finite difference method. The direct arrival will not be influenced by the perturbation c_1, but will be generated from the background model only. In figure 3.21 a comparison between the finite difference method and raytracing has been performed in the constant background velocity model 3.4 and the 1-D background velocity model 3.5. In the seismogram comparison a source wavelet with a center frequency of 15 Hz has been used. In figure 3.21a the direct arrival in the constant velocity background model has been plotted. The raytracing seismogram perfectly overlaps with the finite difference seismogram. In figure 3.21b the direct arrival in the 1-D velocity background model has been plotted. At the receivers closest to the source, the synthetic seismograms overlap quite well, but at receivers further from the source it is seen that the amplitude of the raytracing seismograms is less than the amplitude of the finite difference seismograms. In addition, there is a phase shift in the finite difference seismogram relative to the raytracing seismogram. In figure 3.21c it can be seen how the RMS error of the raytracing increases with increasing frequency and offset in the constant velocity background model. In figure 3.21d it can be seen how the RMS error of the raytracing increases with frequency and offset in a 1-D velocity background model. in both cases the RMS error increases with both frequency and offset. The RMS error is however more strongly dependent on the offset in the 1-D velocity background model. A higher error is also observed when using the 1-D velocity background model. These tests show that the direct arrival is accurately reproduced in the constant velocity background model, but due to the amplitude decay of the raytracing and the phase shift of

the finite difference method, the raytracing is unable to reproduce the pressure field in the 1-D velocity background model at larger offsets. It is unknown whether or not it is the finite difference method or the raytracing that is inaccurate.

3.7.2 Gaussian Model

In figure 3.22 a comparison between the finite difference method and the ray-Born approximation is shown for the constant background model (figure 3.4) with a Gaussian scatterer (figure 3.6). In figure 3.22a the seismograms, generated using the ray-Born approximation and the finite difference method are plotted on top of each other. A perturbation strength of 230 m/s and a centre frequency of 15 Hz has been used. The relative perturbation strength between the background model and the scatterer can be seen in figure 3.7. The second half of the reflection is slightly shifted in time in the ray-Born approximation relative to the finite difference method. This timeshift is due to the fact that the travel times and amplitudes used in the ray-Born approximation are generated from the background model. At low offset the reflections are very weak, indicating that not much energy is reflected back towards the source position. In figure 3.22b the RMS error is plotted as a function of frequency and perturbation strength in order to see how these parameters affect the RMS error. The RMS error has been summed over all offset in order to use as much data as possible for the comparison. The RMS error increases with both frequency and perturbation strength, indicating a reduction in accuracy of the ray-Born approximation. One should therefore be cautious when using high frequencies and large perturbation strengths. In figure 3.22c and 3.22d I show how the offset affects the accuracy of the ray-Born approximation. In 3.22c the highest error is observed with a Ricker wavelet centre frequency of 15 Hz at offset 200m. The error increases again at roughly 2 km offset. In 3.22d the highest error is observed at 230 m/s perturbation strength at 200 m offset. The error increases again at higher offset. The result from these figures implicate that the ray-Born approximation is having problems with weak reflections. At high offset the RMS error increases, indicating that the error is increasing with offset with the exception of the weak reflections at low offset. Even though there is a large relative difference between the ray-Born approximation and the finite difference method at low offset, this error can be disregarded due to the low amplitude of the seismograms at this offset.

The same comparison has been performed with a 1-D background model (figure 3.5) and a Gaussian scatterer (figure 3.6). In figure 3.23a the seismogram, generated using the ray-Born approximation and the finite difference method are plotted on top of each other. A perturbation strength of 230 m/s and a centre frequency of 15 Hz has been used. The relative perturbation strength between the background model and the scatterer can be seen in figure 3.8. The second half of the reflection is slightly shifted in time when using the ray-Born approximation relative to the finite difference method. This timeshift is caused bythe fact that the travel times and amplitudes used are the ray-Born approximation is generated from the background model. At low offset the reflections are very weak, indicating that not much energy is reflected back towards the source position. The velocity in the 1-D background

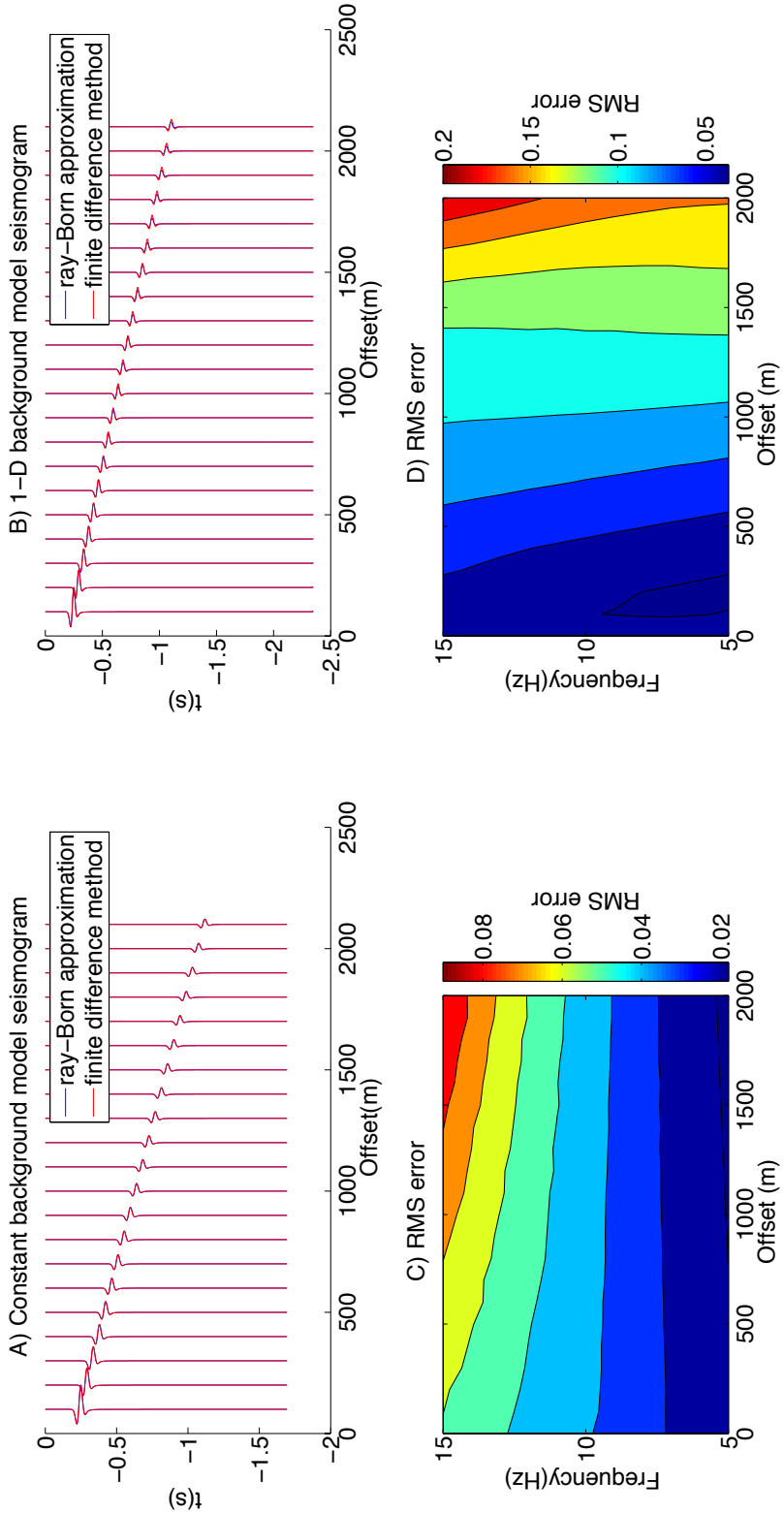

Figure 3.21: The synthetic seismogram produced by performing raytracing and the finite difference method have been computed in the constant velocity background model and the 1-D velocity background model. a) Synthetic seismogram comparison for the direct arrival in the constant velocity background model. b) Synthetic seismogram comparison for the direct arrival in the 1-D velocity background model. c) RMS error of the raytracing with increasing frequency and offset summed over all perturbation strengths for the constant velocity background model. d) RMS error of the raytracing with increasing frequency and offset summed over all perturbation strengths for the 1-D velocity background model.

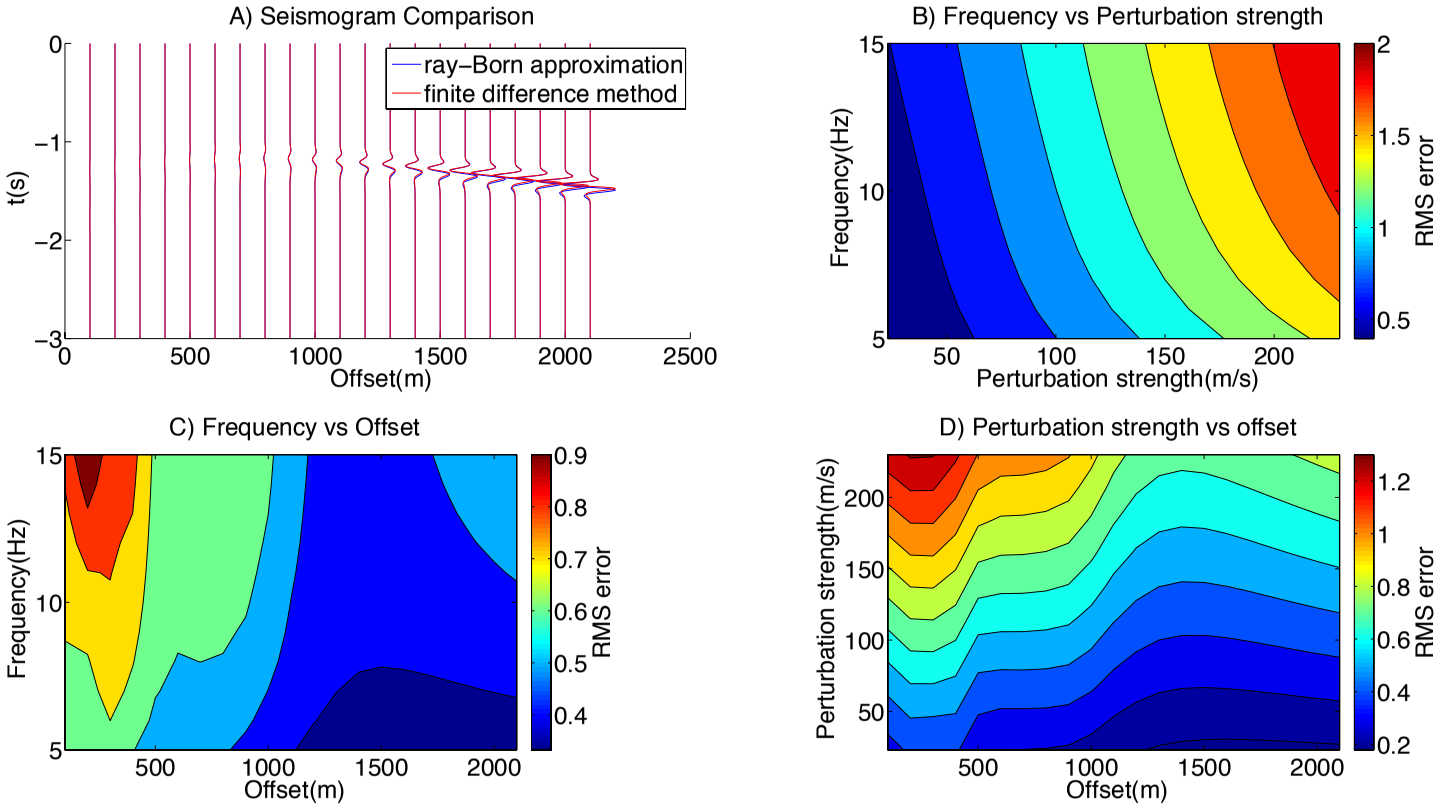

Figure 3.22: The synthetic seismogram produced by the ray-Born approximation and the finite difference method have been compared for a constant background velocity model with a Gaussian scatterer. a) Synthetic seismogram generated using a source wavelet with 15 Hz centre frequency and a scatterer with perturbation strength 230 m/s. b) RMS error between the ray-Born approximation with increasing frequency and perturbation strength summed over all offset. c) RMS error between the ray-Born approximation with increasing frequency and offset summed over all perturbation strengths. d) RMS error between the ray-Born approximation with increasing perturbation strength and offset summed over all frequency.

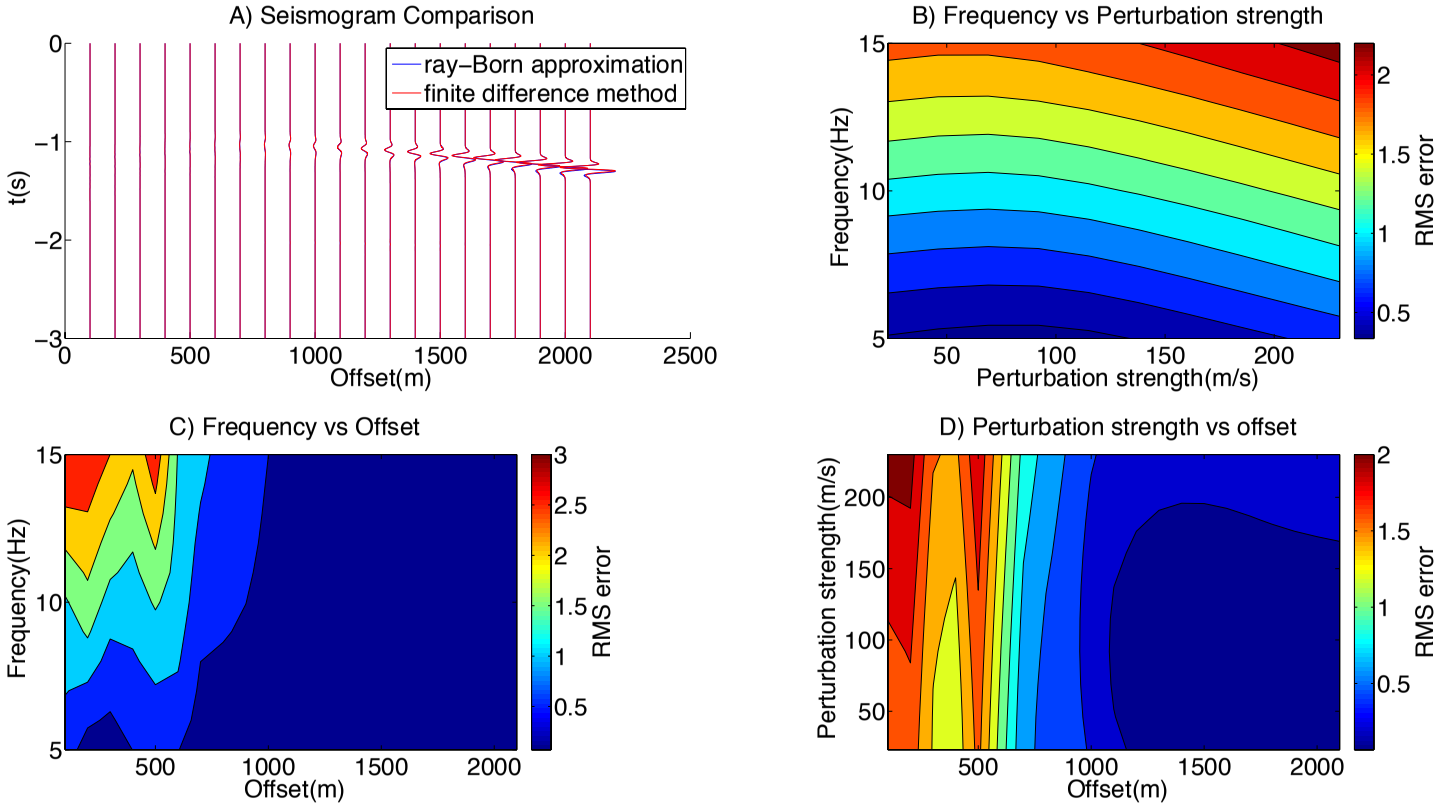

Figure 3.23: The synthetic seismogram produced by the ray-Born approximation and the finite difference method have been compared for a 1-D background velocity model with a Gaussian scatterer. a) Synthetic seismogram generated using a source wavelet with 15 Hz centre frequency and a scatterer with perturbation strength 230 m/s. b) RMS error between the ray-Born approximation with increasing frequency and perturbation strength summed over all offset. c) RMS error between the ray-Born approximation with increasing frequency and offset summed over all perturbation strengths. d) RMS error between the ray-Born approximation with increasing perturbation strength and offset summed over all frequency.

model is linearly increasing, the reflection is therefore registered at a earlier time than in the constant velocity background model. It can also be observed that the reflection is shorter in time for the 1-D background model, which occurs as an effect of having a smooth scatterer and a smooth background model. In figure 3.23b the RMS error is plotted as a function of frequency and perturbation strength in order to see how these parameters affect the RMS error. The RMS error increases with both frequency and perturbation strength, indicating a reduction in accuracy of the ray-Born approximation. The figure shows the same trend as seen in figure 3.22b. Some differences are however observed: in the 1-D model the perturbation strength of the scatterer is lower relative to the background model. As a result, the RMS error does not increase as strongly with increasing perturbation strength compared to the frequency. In figures 3.23c and 3.23d I show how the offset affects the accuracy of the ray-Born approximation. In 3.23c the highest error is observed with a source wavelet centre frequency of 15 Hz at offset 200m. In 3.23d the highest error is observed at 230 m/s perturbation strength at 200 m offset. The results follow the same trend seen in figures 3.22c and 3.22d. The error is however larger when using the 1-D velocity background model than when using the constant velocity background model.

3.7.3 Layer Model

In figure 3.24 a comparison between the finite difference method and the ray-Born approximation is shown for the constant background velocity model (figure 3.4) with a layer scatterer (figure 3.9). In figure 3.24a the seismogram generated from both the ray-Born approximation and the finite difference method are plotted on top of each other. A perturbation strength of 230 m/s and a centre frequency of 15 Hz is used. The relative perturbation strength between the background model and the scatterer can be seen in figure 3.10. The reflection from the upper boundary of the layer is accurately reproduced when comparing the ray-Born approximation traces to the finite difference method traces. The reflection from the lower boundary is shifted in time due to inaccurate traveltimes and amplitudes when using the ray-Born approximation. This timeshift is increasing with increasing offset due to the fact that at higher offsets a longer time is spent in the layer relative to smaller offsets, increasing the traveltime error of the ray-Born approximation. Some smaller arrivals can be seen later in the seismogram, these are produced by the edges of the layer. The smaller arrivals are not taken into account in the error plots. These reflections are poorly reproduced by the ray-Born approximation compared to the finite difference method for all offset. In figure 3.24b the RMS error is plotted as a function of frequency and perturbation strength in order to see how these parameters affect the RMS error. The RMS error has been summed over all offset in order to use as much data as possible for the comparison. The RMS error increases with both frequency and perturbation strength, indicating a reduction in accuracy of the ray-Born approximation. The error depends most strongly on the perturbation strength. In figures 3.24c and 3.24d I show how the offset affects the accuracy of the ray-Born approximation for the layer model. In both figures it is seen that the RMS error increases with offset, frequency and perturbation strength. These results confirm our observations from the seismograms.

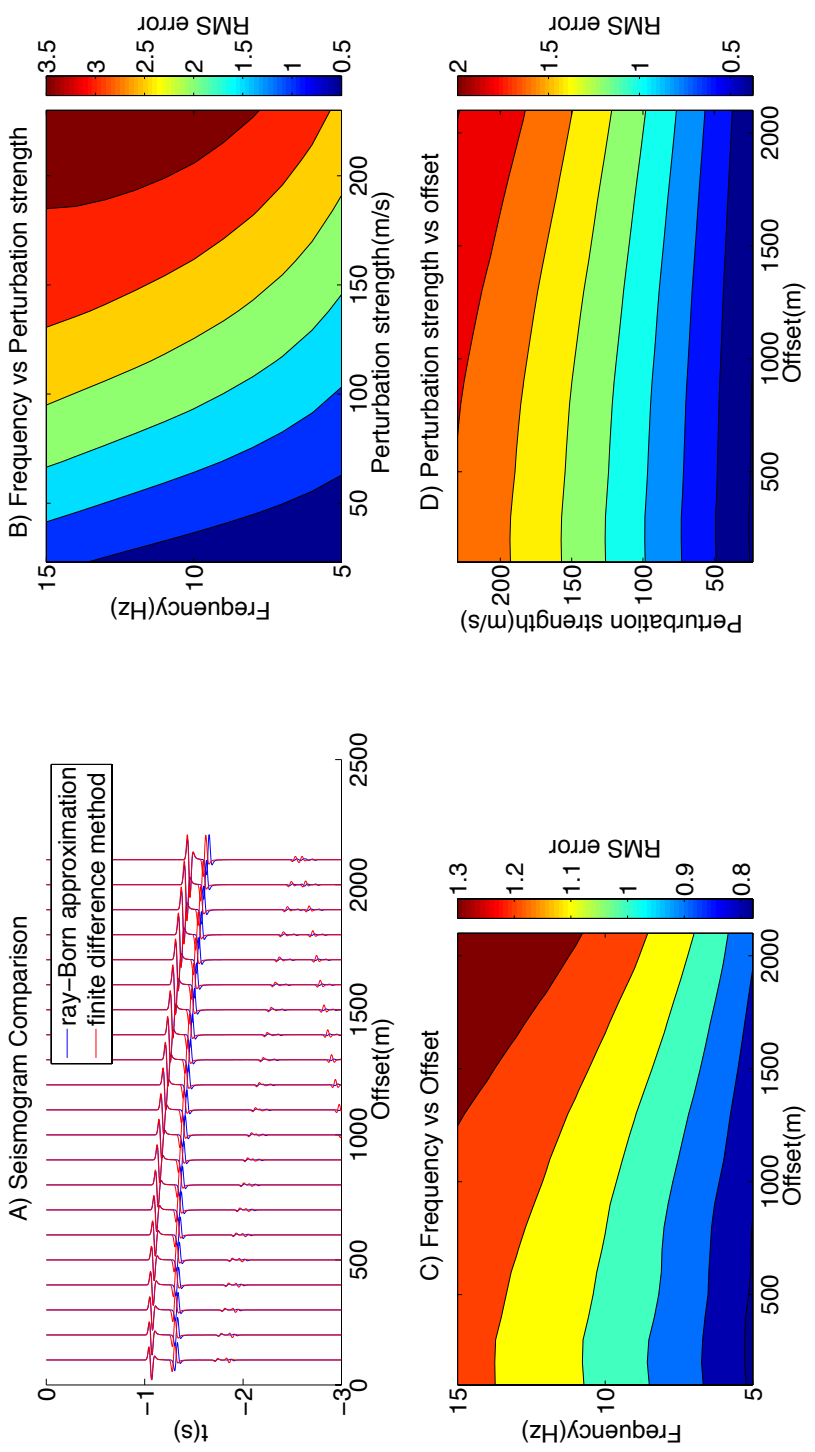

Figure 3.24: The synthetic seismogram produced by the ray-Born approximation and the finite difference method have been compared for a constant background velocity model with a layer scatterer. a) Synthetic seismogram generated using a source wavelet with 15 Hz centre frequency and a scatterer with perturbation strength 230 m/s. b) RMS error between the ray-Born approximation with increasing frequency and perturbation strength summed over all offset. c) RMS error between the ray-Born approximation with increasing frequency and offset summed over all perturbation strengths. d) RMS error between the ray-Born approximation with increasing perturbation strength and offset summed over all frequency.

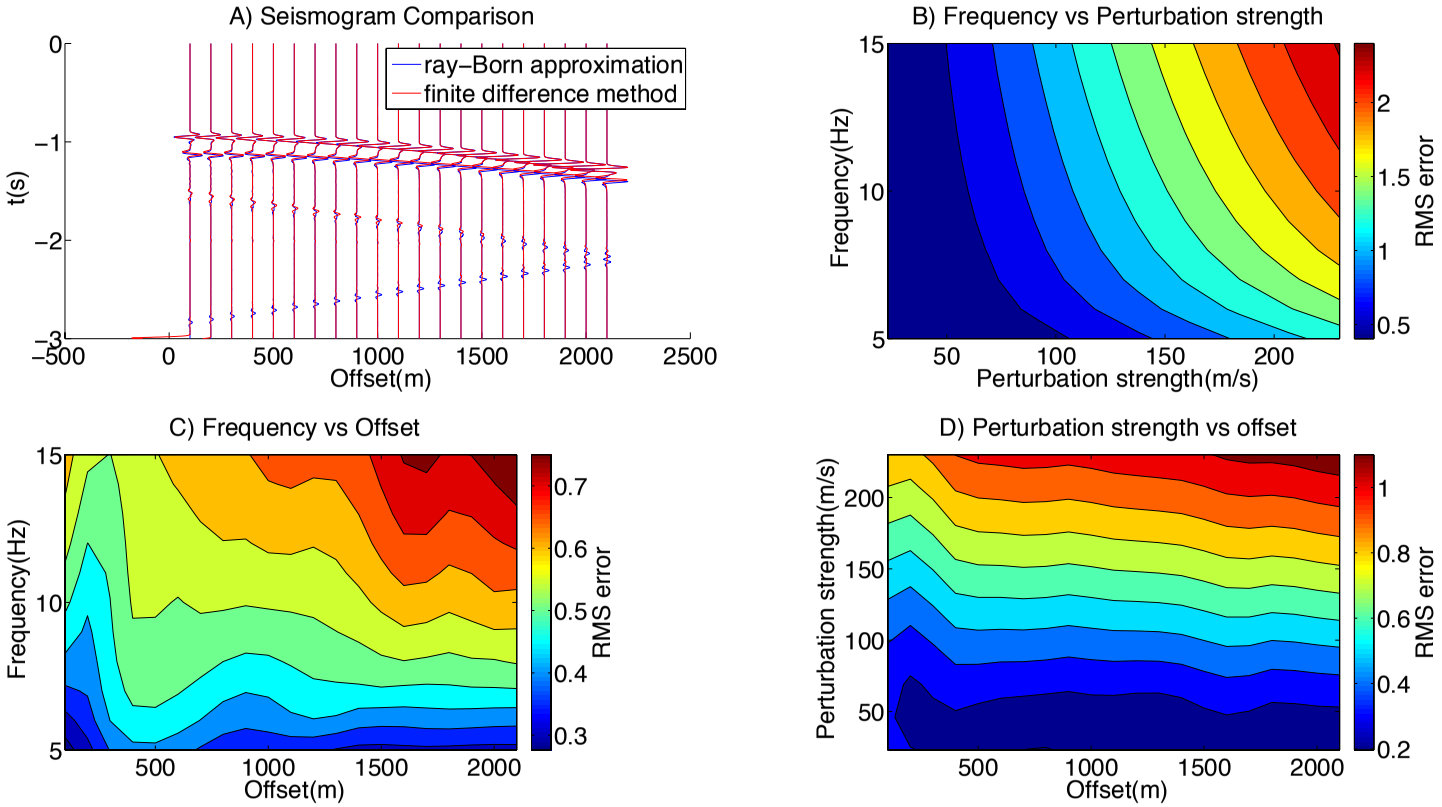

Figure 3.25: The synthetic seismogram produced by the ray-Born approximation and the finite difference method have been compared for a 1-D background velocity model with a layer scatterer. a) Synthetic seismogram generated using a source wavelet with 15 Hz centre frequency and a scatterer with perturbation strength 230 m/s. b) RMS error between the ray-Born approximation with increasing frequency and perturbation strength summed over all offset. c) RMS error between the ray-Born approximation with increasing frequency and offset summed over all perturbation strengths. d) RMS error between the ray-Born approximation with increasing perturbation strength and offset summed over all frequency.

The same comparison was performed for the 1-D background velocity model (figure 3.5) and the layer scatterer (figure 3.9). In figure 3.25a the seismogram generated from both the ray-Born approximation and the finite difference method are plotted on top of each other. A perturbation strength of 230 m/s and a centre frequency of 15 Hz has been used. The relative perturbation strength between the background model and the scatterer is shown in figure 3.11. The reflection from the upper boundary of the layer is accurately reproduced when comparing the ray-Born approximation traces to the finite difference method traces. The reflection from the lower boundary is shifted in time due to inaccurate traveltimes and amplitudes when using the ray-Born approximation. This timeshift increases with offset due to the fact that at higher offsets a longer time is spent in the layer relative to smaller offsets. This increases the traveltime error of the ray-Born approximation. Since the velocity in the 1-D background model increases linearly, the reflection occurs at a earlier time than in the constant velocity background model. The timeshift is less for the 1-D background velocity model than for the constant velocity background model for the same reason. Some smaller arrivals can be seen later in the seismogram, these are produced by the edges of the layer. These reflections are not considered in the RMS error computation. These reflections are poorly reproduced by the ray-Born approximation compared to the finite difference method for all offset. The reflections from the edges are even more poorly reproduced in the case of the 1-D background velocity model when compared to the constant velocity background model. In figure 3.25b the RMS error is plotted as a function of frequency and perturbation strength in order to see how these parameters affect the RMS error. The RMS error has been summed over all offset in order to use as much data as possible for the comparison. The RMS error increases with both frequency and perturbation strength, indicating a reduction in accuracy of the ray-Born approximation. The figure shows the same trend as seen in figure 3.24b. Some differences are however observed; in the 1-D model the perturbation strength of the scatterer is lower relative to the background model. The RMS error does therefore not increase as strongly with increasing perturbation strength compared to the frequency. In figures 3.24c and 3.24d I show how the offset affects the accuracy of the ray-Born approximation for the layer model. In both figures it is seen that the RMS error is increasing with offset, frequency and perturbation strength. At the receivers closest to the source it is possible to observe an increase in error that is present for all frequencies and perturbation strengths. The reason for this is most likely the inaccuracy of the 2-D Green function in the near field.

3.7.4 Random Gaussian Model

Random Gaussian models have been generated with correlation lengths ranging from 50 m to 500 m. The models were generated with different correlation lengths in order to see how the size of the scatterers affect the RMS error with different perturbation strengths and frequencies. The figures presented in this subsection are for random Gaussian media with correlation lengths of 50 and 500 m.

In figure 3.26 a comparison between the finite difference method and the ray-Born approximationis

shown for the constant velocity background model 3.4 with a random Gaussian media scatterer with a correlation length of 50 m (figure 3.12). In figure 3.26a the seismograms generated from both the ray-Born approximation and the finite difference method are plotted in top of each other. A perturbation strength of 230 m/s and a centre frequency of 15 Hz is used. The relative perturbation strength between the background model and the scatterer is shown in figure 3.13. Observations from the seismogram show that the ray-Born approximation accurately reproduces most of the wavefield for all offsets. Some traces are however more accurately reproduced than others. This effect occurs due to the random nature of the velocity model. At some areas there is a higher velocity relative to the background velocity model and in other areas this is a of lower velocity relative to the background velocity model. This effect will cause positive/negative traveltime errors at some offset while at other offset the traveltime is correct. A second effect that occur is multiscattering. This means that the reflections from the Gaussian scatterers are reflected from other Gaussian scatterers. This effect is not modelled by the ray-Born approximation. This effect is strongest for the strongest scatterers and will therefore not be seen at all offsets. Figures 3.26c and 3.26d confirm the observations seen in the seismogram and the error can be seen to become high at offsets 100 m, 300 m, 1000 m, 1500, and 1800 m. It is important to note that this effect is unique for this particular realisation of a random Gaussian media. If the error was averaged over many random Gaussian media, some pattern might be observed. This means that the error is only valid for the model used in this thesis and not all models. In figure 3.26b it can be seen that the error is increasing with both perturbation strength and frequency. Of these factors, the perturbation strength appear to be more dominant because the error is more steeply increasing with increasing perturbation strength than frequency.

The same comparison was performed while using the 1-D background model and the same random Gaussian media with a correlation length of 50 m. In figure 3.27 a comparison between the finite difference method and the ray-Born approximation has been performed for the 1-D velocity background model (figure 3.5) with a random Gaussian media scatterer with a correlation length of 50 m (figure 3.12). In figure 3.27a the seismogram generated from both the ray-Born approximation and the finite difference method are plotted in top of each other. A perturbation strength of 230 m/s and a centre frequency of 15 Hz is used. The relative perturbation strength between the background model and the scatterer is shown in figure 3.14. The seismogram follows the same trend as in figure 3.26a. The ray-Born approximation accurately reproduces the wavefield for some offsets while at other offsets the wavefield is less accurately reproduced. Figures 3.27c and 3.27d confirm the observations seen in the seismogram and the error can be seen to become high at offsets 100 m, 300 m, 1000 m, 1500, and 1800 m. It is important to note that this effect is unique for this particular realisation of a random Gaussian media. If the error was averaged over many random Gaussian media, some pattern might be observed. In figure 3.27b it can be seen that the error is increasing with both perturbation strength and frequency. Of these factors, the perturbation strength appear to be more dominant because the error is more steeply increasing with increasing perturbation strength than frequency. The error is less strongly dependant on the perturbation strength than when using the constant velocity background

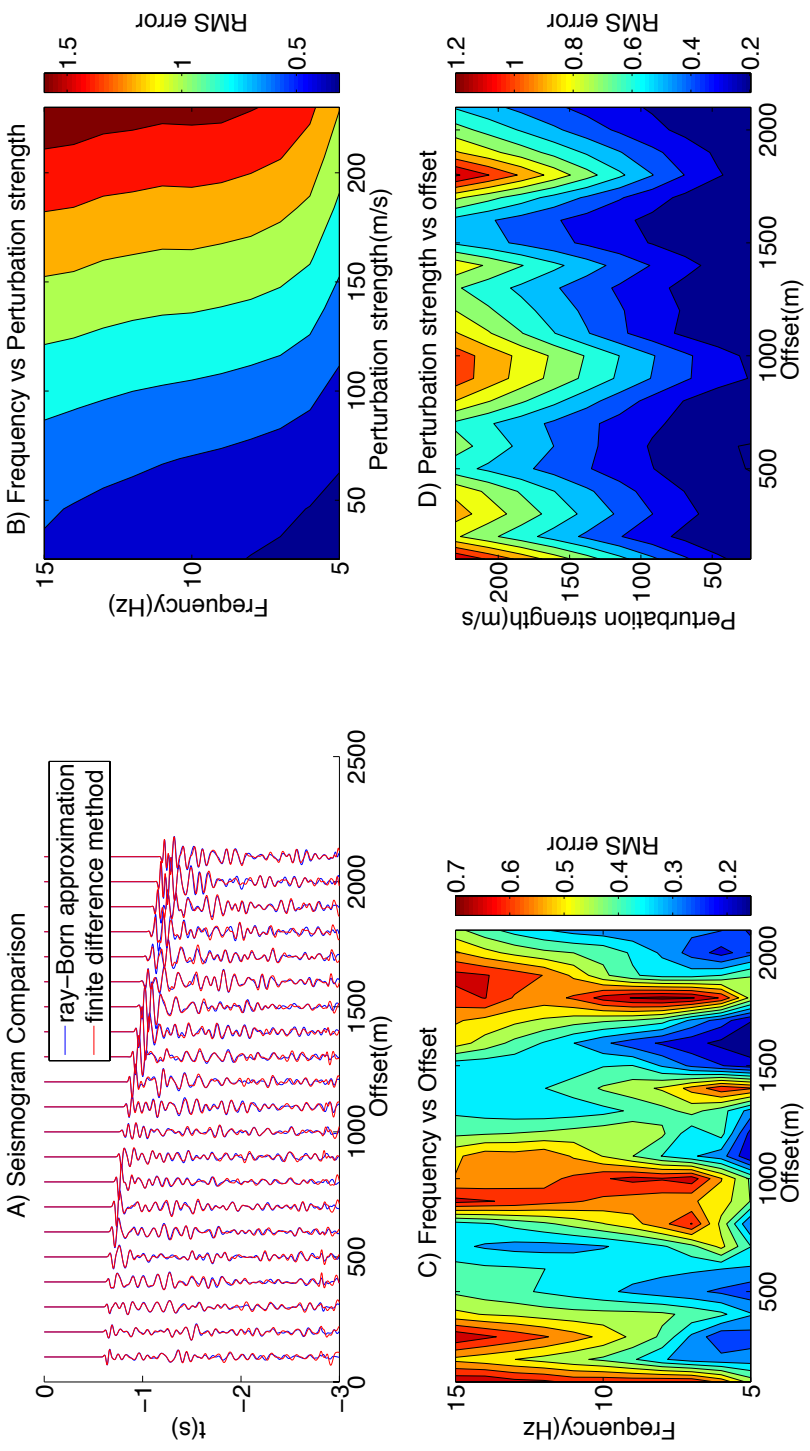

Figure 3.26: The synthetic seismogram produced by the ray-Born approximation and the finite difference method have been compared for a constant background velocity model with a Random Gaussian media scatterer with a correlation length of 50 m. a) Synthetic seismogram generated using a source wavelet with 15 Hz centre frequency and a scatterer with perturbation strength 230 m/s. b) RMS error between the ray-Born approximation with increasing frequency and perturbation strength summed over all offset. c) RMS error between the ray-Born approximation with increasing frequency and offset summed over all perturbation strengths. d) RMS error between the ray-Born approximation with increasing perturbation strength and offset summed over all frequency.

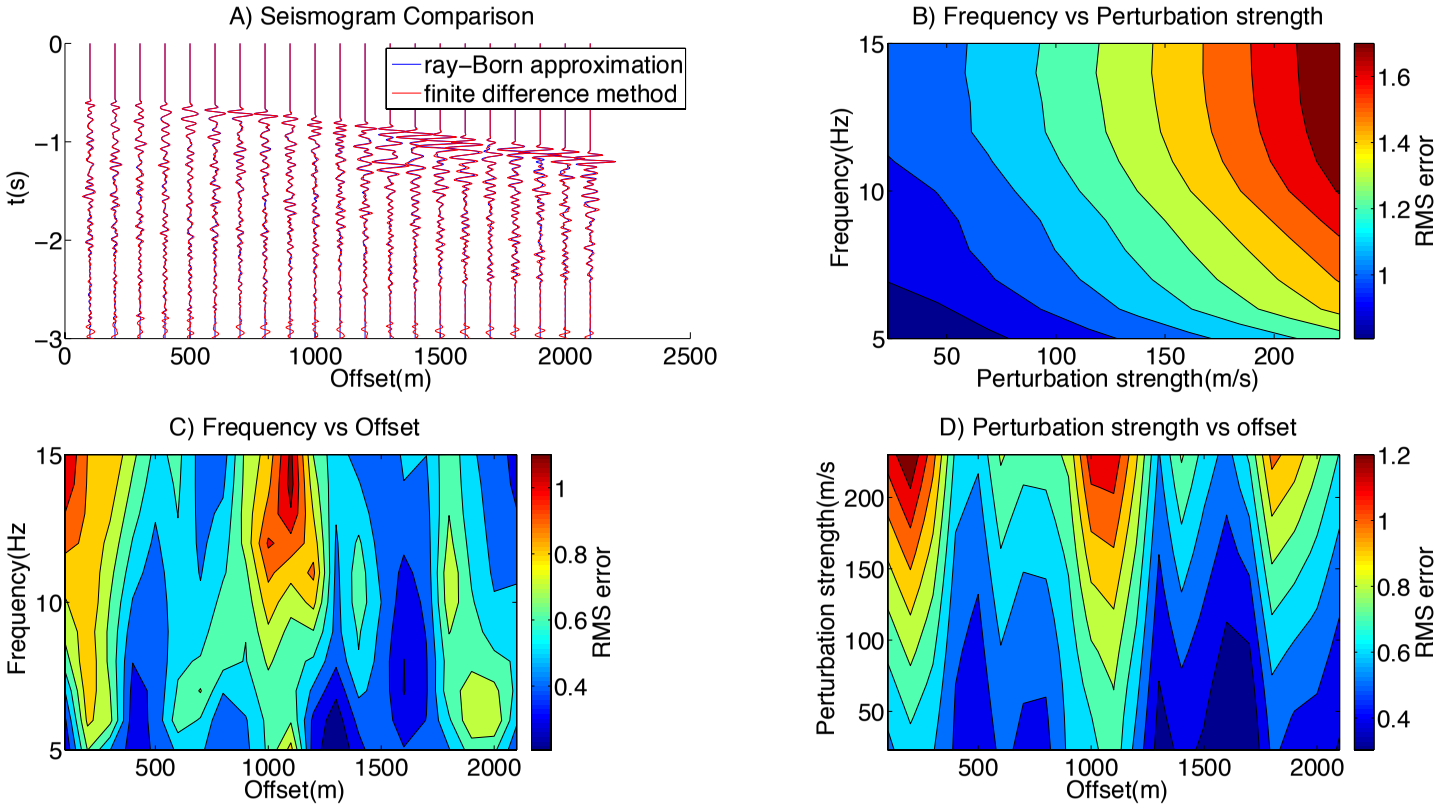

Figure 3.27: The synthetic seismogram produced by the ray-Born approximation and the finite difference method have been compared for a 1-D background velocity model with a Random Gaussian media scatterer with a correlation length of 50 m. a) Synthetic seismogram generated using a source wavelet with 15 Hz centre frequency and a scatterer with perturbation strength 230 m/s. b) RMS error between the ray-Born approximation with increasing frequency and perturbation strength summed over all offset. c) RMS error between the ray-Born approximation with increasing frequency and offset summed over all perturbation strengths. d) RMS error between the ray-Born approximation with increasing perturbation strength and offset summed over all frequency.

model as the error appear to increase more with frequency. This is an effect of having a lower velocity contrast relative to the background velocity model.

In figure 3.28 a comparison between the finite difference method and the ray-Born approximation has been performed for the constant velocity background model (figure 3.4) with a random Gaussian medium scatterer with a correlation length of 500 m (figure 3.15). In figure 3.28a the seismogram generated from both the ray-Born approximation and the finite difference method are plotted on top of each other. A perturbation strength of 230 m/s and a centre frequency of 15 Hz is used. The relative perturbation strength between the background model and the scatterer can be seen in figure 3.16. Observations from the seismogram show that the upper reflections are reproduced perfectly for all frequencies and offsets. This reflection is produced from a sharp interface at the top of the random Gaussian media and will therefore be disregarded in this comparison. The ray-Born approximation has problems reproducing the reflections in this model and the error is significantly higher than in any of the other scattering models. The increase in error does not appear in the random Gaussian medium with a correlation length of 50 m. The ray-Born approximation seismogram does not appear to be timeshifted relative to the finite difference method. Figure 3.28b show that the error increases with both perturbation strength and frequency. It appears that the frequency and perturbation strength are equally important factors when it comes to increase in error because the error increases equally with both frequency and perturbation strength. In figures 3.28c and 3.28d it is seen that the highest error is observed at low offset. It is important to note that this effect is unique for this particular realisation of a random Gaussian media. If the error was averaged over many random Gaussian media, some pattern might be observed.

In figure 3.29 a comparison between the finite difference method and the ray-Born approximation has been performed for the 1-D velocity background model (figure 3.4) with a random Gaussian medium scatterer with a correlation length of 500 m (figure 3.15). In figure 3.29a the seismogram generated from both the ray-Born approximation and the finite difference method are plotted on top of each other. A perturbation strength of 230 m/s and a centre frequency of 15 Hz is used. The relative perturbation strength between the background model and the scatterer can be seen in figure 3.17. The observations are very similar to what was observed in figure 3.28. Observations from the seismogram show that the upper reflections is reproduced perfectly for all frequencies and offsets. This reflection is however produced from a sharp interface at the top of the random Gaussian media and will therefore be disregarded in this comparison. The ray-Born approximation has problems reproducing the reflections in this model and the error is significantly higher than in any of the other scattering models. The increase in error does not appear in the random Gaussian medium with a correlation length of 50 m. The ray-Born approximation seismogram does not appear to be timeshifted relative to the finite difference method. Figure 3.28b show that the error is increasing with both perturbation strength and frequency. It appears that the frequency and perturbation strength are equally important factors when it comes to increase in error because the error increases equally with both frequency and perturbation

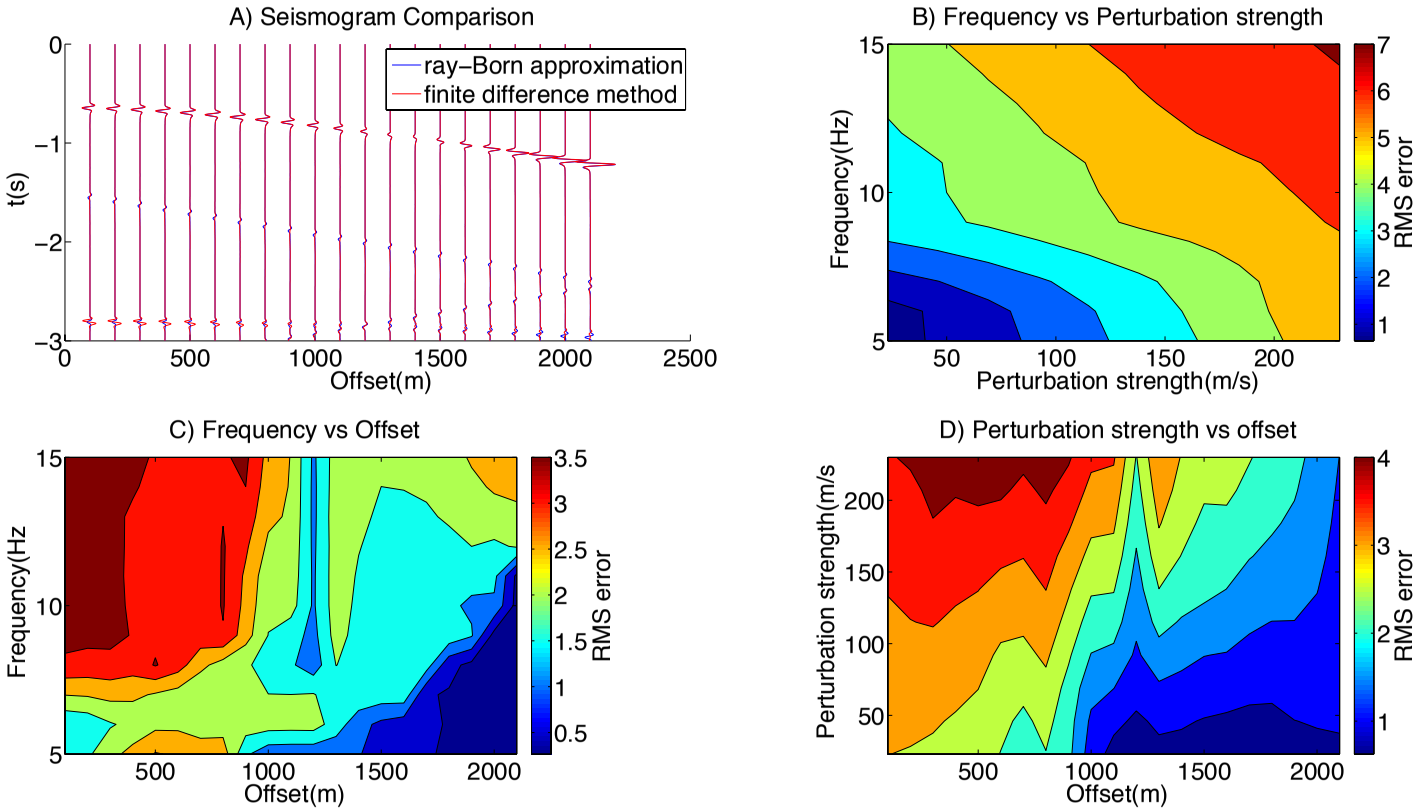

Figure 3.28: The synthetic seismogram produced by the ray-Born approximation and the finite difference method have been compared for a constant background velocity model with a Random Gaussian media scatterer with a correlation length of 500 m. a) Synthetic seismogram generated using a source wavelet with 15 Hz centre frequency and a scatterer with perturbation strength 230 m/s. b) RMS error between the ray-Born approximation with increasing frequency and perturbation strength summed over all offset. c) RMS error between the ray-Born approximation with increasing frequency and offset summed over all perturbation strengths. d) RMS error between the ray-Born approximation with increasing perturbation strength and offset summed over all frequency.

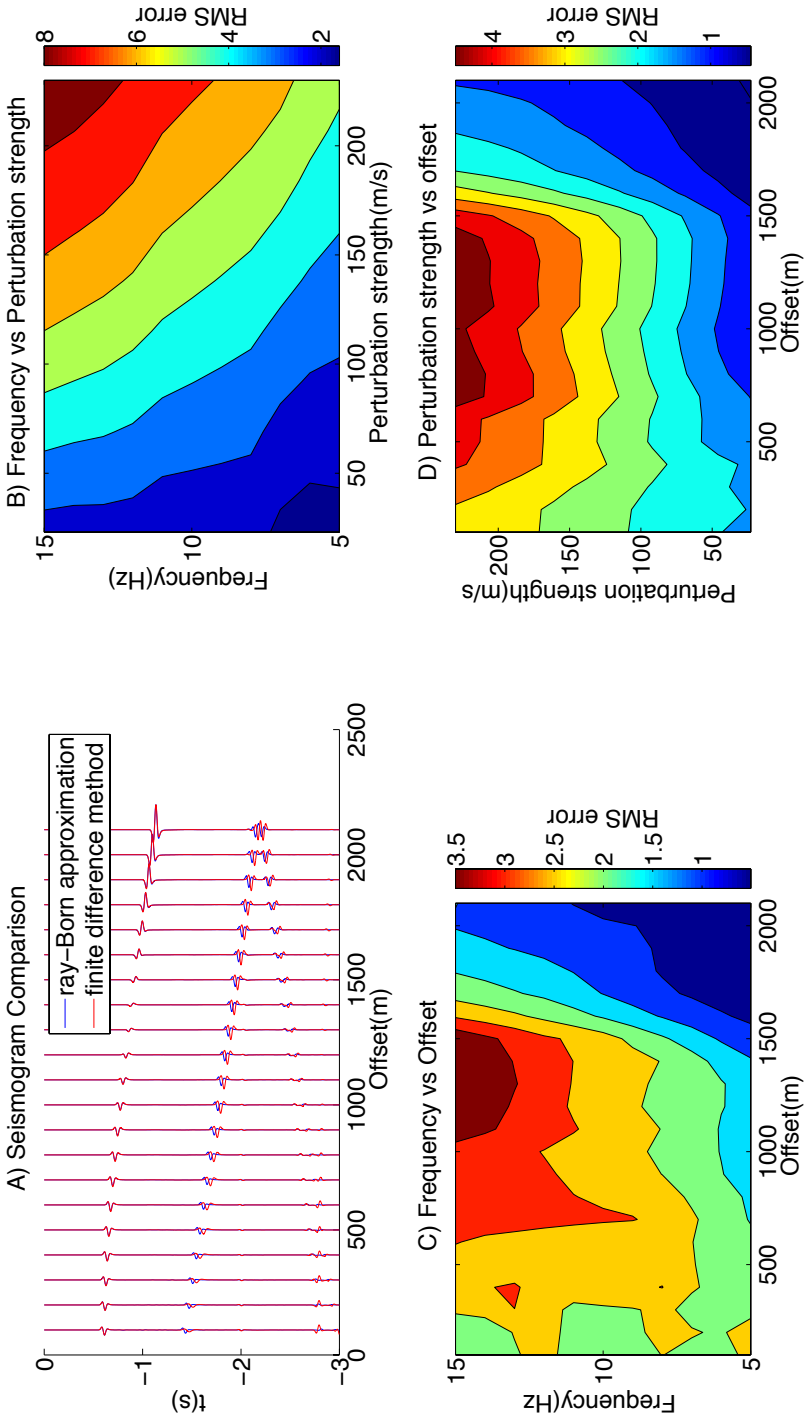

Figure 3.29: The synthetic seismogram produced by the ray-Born approximation and the finite difference method have been compared for a 1-D background velocity model with a Random Gaussian media scatterer with a correlation length of 500 m. a) Synthetic seismogram generated using a source wavelet with 15 Hz centre frequency and a scatterer with perturbation strength 230 m/s. b) RMS error between the ray-Born approximation with increasing frequency and perturbation strength summed over all offset. c) RMS error between the ray-Born approximation with increasing frequency and offset summed over all perturbation strengths. d) RMS error between the ray-Born approximation with increasing perturbation strength and offset summed over all frequency.

strength. In Figures 3.29c and 3.29d it is seen that the highest error is seen at low offsets. It is important to note that this effect is unique for this particular realisation of a random Gaussian media. If the error was averaged over many random Gaussian media, some pattern might be observed.

When considering the results obtained for different correlation lengths it is possible to observe a trend in the error distribution. For small correlation lengths the perturbation strength is the dominant factor that leads to increase in error between the ray-Born approximation and the finite difference method. As the correlation length increases, the influence of the frequency becomes increases. With a correlation length of 500 m the frequency and perturbation strength are equally significant factors when it comes to increase in error of the ray-Born approximation. The error between the ray-Born approximation appears to increase with increasing correlation length, indicating that the large scatterers relative to the background model will reduce the accuracy of the ray-Born approximation relative to the finite difference method.

3.7.5 Modified SEG/EAGE Overthrust Model

The forward modelling comparison between the ray-Born approximation and the finite difference method has been performed for four different sources in the modified SEG/EAGE overthrust model. The background model can be seen in figure 3.18 while the scatterer is seen in figure 3.19. As usual, the sources are marked with a red cross while the receivers are marked with a green cross. The Ricker wavelet with a centre frequency of 10 Hz has been used in this modelling. In figure 3.30 the ray paths for a source located at 0 km offset are shown. After 6 km offset from the source, multipathing occurs. In figure 3.31 the synthetic seismogram for the source located at 0 km offset with receivers between 0 and 12 km offset is plotted. When comparing the ray-Born approximation with the finite difference method it is possible to see that near offset traces are very well reproduced, while the traces at offsets higher than 7 km are poorly reproduced. The reason for the decrease in accuracy when using the ray-Born approximation is most likely a result of incorrect amplitude computation due to multipathing when using raytracing. In figure 3.32 the synthetic seismogram for the source located at 4 km offset with receivers ranging between 0 and 12 km offset are shown. The traces from 4 km offset to 0 km and the traces from 4 km to 8 km offset are well reproduced by the ray-Born approximation while the traces from 9 km to 12 km offset are more poorly reproduced. In figure 3.33 the synthetic seismogram for the source located at 8 km offset with receivers between 0 and 12 km offset is shown. The traces from 4 km offset to 8 km and the traces from 8 km to 12 km offset are well reproduced by the ray-Born approximation while the traces from 4km to 0 km offset are more poorly reproduced. In figure 3.34 the synthetic seismogram for the source located at 12 km offset with receivers ranging from 0 to 12 km offset is plotted. The traces from 12 km offset to 2 km offset are well reproduced by the ray-Born approximation while the traces from 1km to 0 km offset are more poorly reproduced. The results from these figures show that the ray-Born approximation has problems reproducing the pressure field accurately at offset higher than 5 km from the source position for this velocity model

and frequency. As stated earlier, the reason for the decrease in accuracy with increasing offset is most likely caused by the multipathing that takes place when performing raytracing. The error could also be contributed to multiscattering which can be more prominent at higher offsets but this is unlikely for this model as the increase in error matches very well with where we see multipathing start to occur.

3.7.6 Computation Time

In this section I will perform a comparison between the computation time of the ray-Born approximation and the finite difference method for the velocity models that are used in this thesis. The computation time of the methods were computed for the two basic background models, the three basic scatterers, every perturbation strength and every frequency. The computation time of the finite difference method is constant for any scatterer, frequency and perturbation strength. An increase in computation time occurs when going from the constant velocity background model to the 1-D velocity background model. This increase in computation time occurs because the velocities in the 1-D velocity background model is higher than in the constant velocity background model and as a result a lower time step has to be used. The computation time of the ray-Born approximation varies with background model, scatterer and frequency. The computation time of the raytracing is however so large relative to the ray-Born approximation that the effect of changing the scatterer or frequency is miniscule. The computation time of the ray-Born approximation was computed to be roughly a factor of two lower than the computation time of the finite difference method. It should however be noted that the geometry used consists of one source and 20 receivers. The computation time of the finite difference method is linearly increasing with the number of sources while the computation time of the ray-Born approximation is linearly increasing with both sources and receivers. If the same number of sources and receivers were used, the computation time of the ray-Born approximation would be a factor of 40 times faster than the finite difference method. Several optimisations can be applied to each method, and especially the finite difference method would get a great reduction in cost with the introduction of effective absorbing boundary conditions.

3.8 Discussion

In this chapter a thorough comparison between the ray-Born approximation and the finite difference method has been performed. The results show that the accuracy of the ray-Born approximation is dependent on the background model, the size, shape and roughness of the scatterer and the perturbation strength. The accuracy of the ray-Born approximation diminishes with increasing frequency and perturbation size and strength but still remains sufficiently accurate for perturbation strengths below 10 percent. The largest limitation of the ray-Born approximation appears in cases where multipathing occur in the background model. In such cases the traveltime and amplitude generated by the ray-Born approximation will be inaccurate. Despite some inaccuracy for strong scatterers and background models where multipathing occur, the ray-Born approximation has many benefits. The

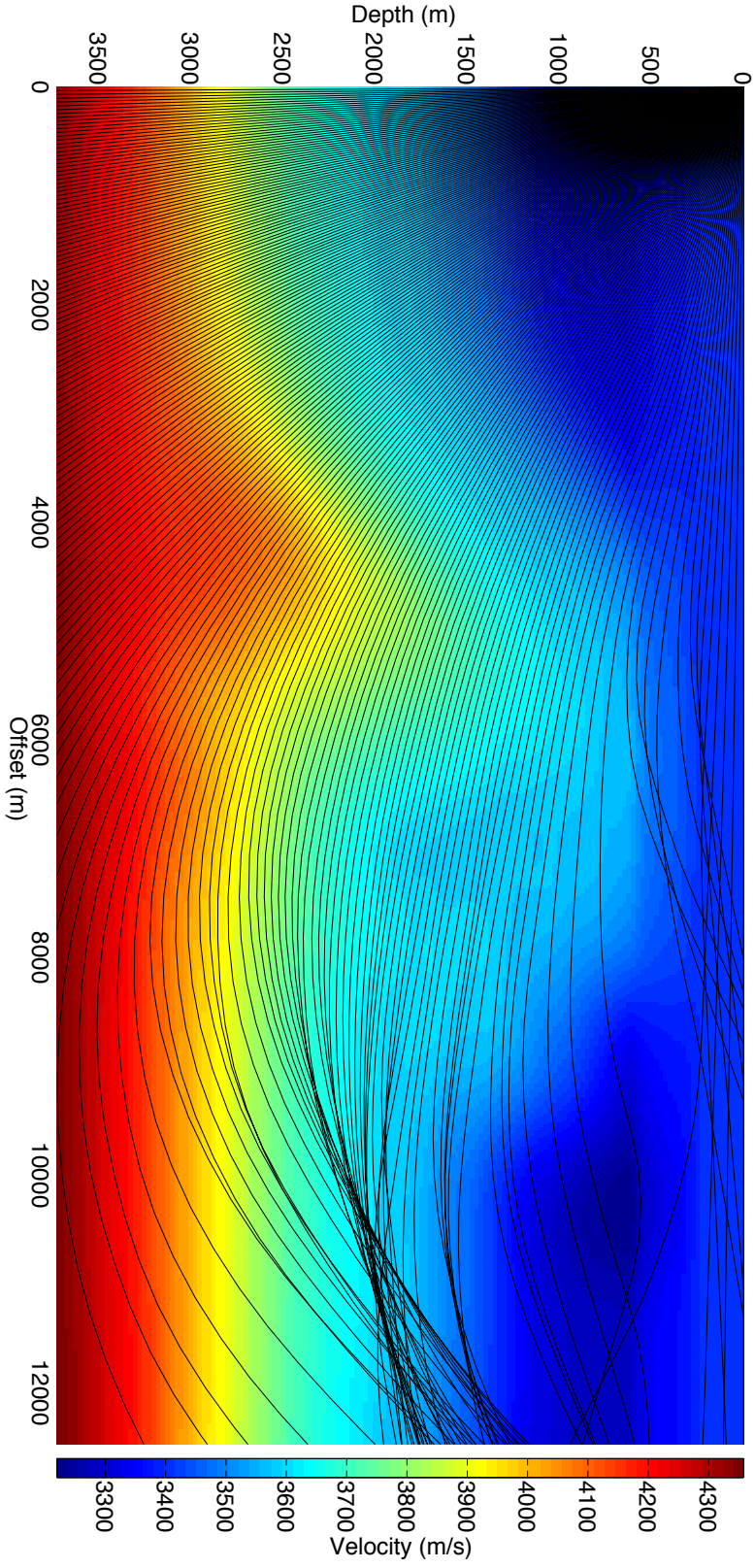

Figure 3.30: Raytracing in the SEG/EAGE Overthrust model

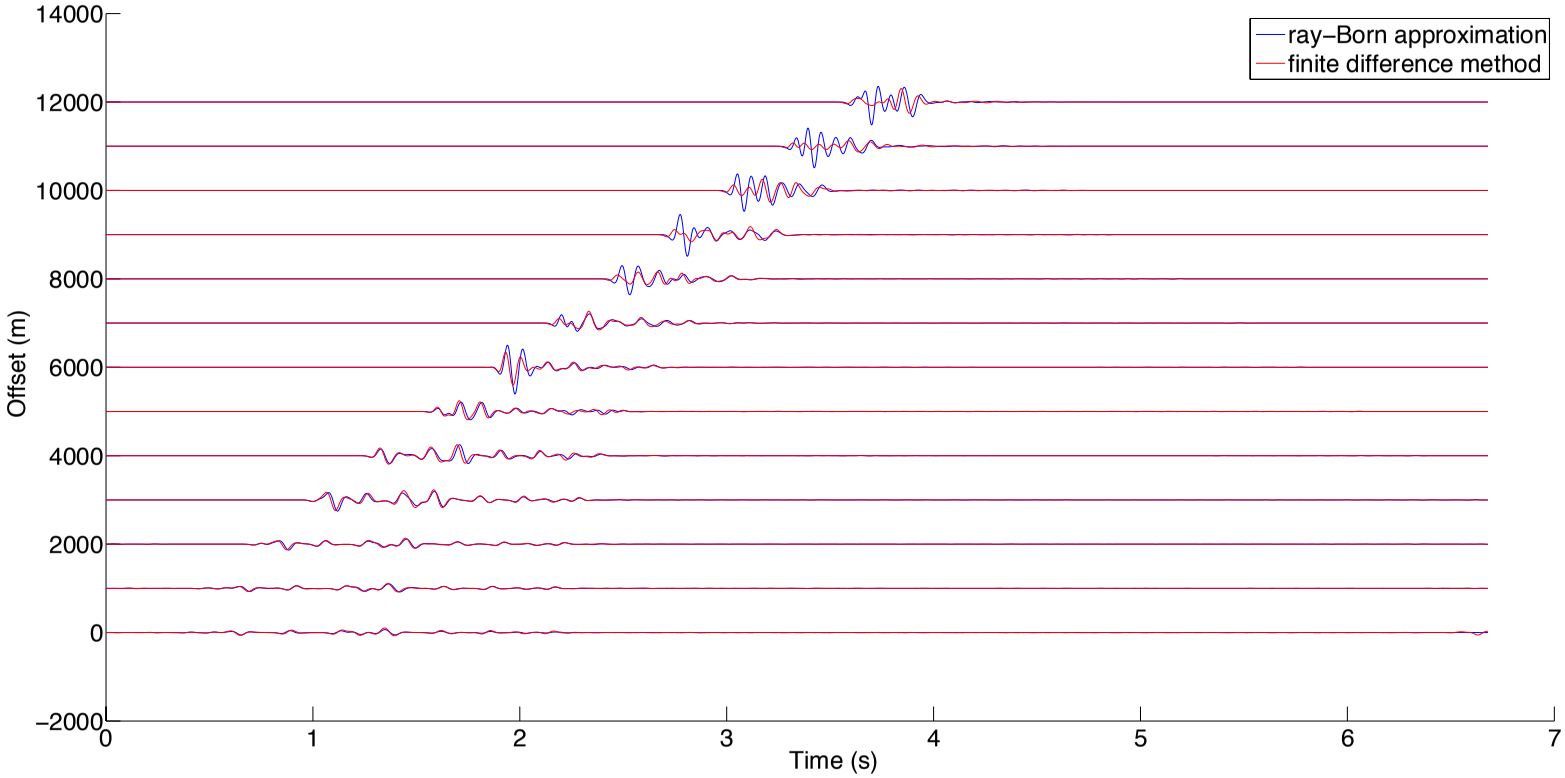

Figure 3.31: Comparison between the Ray-Born approximation and the finite difference method for the SEG/EAGE overthrust model. The source is located at 0 km offset while the receivers are located at offset ranging from 1 to 12 km.

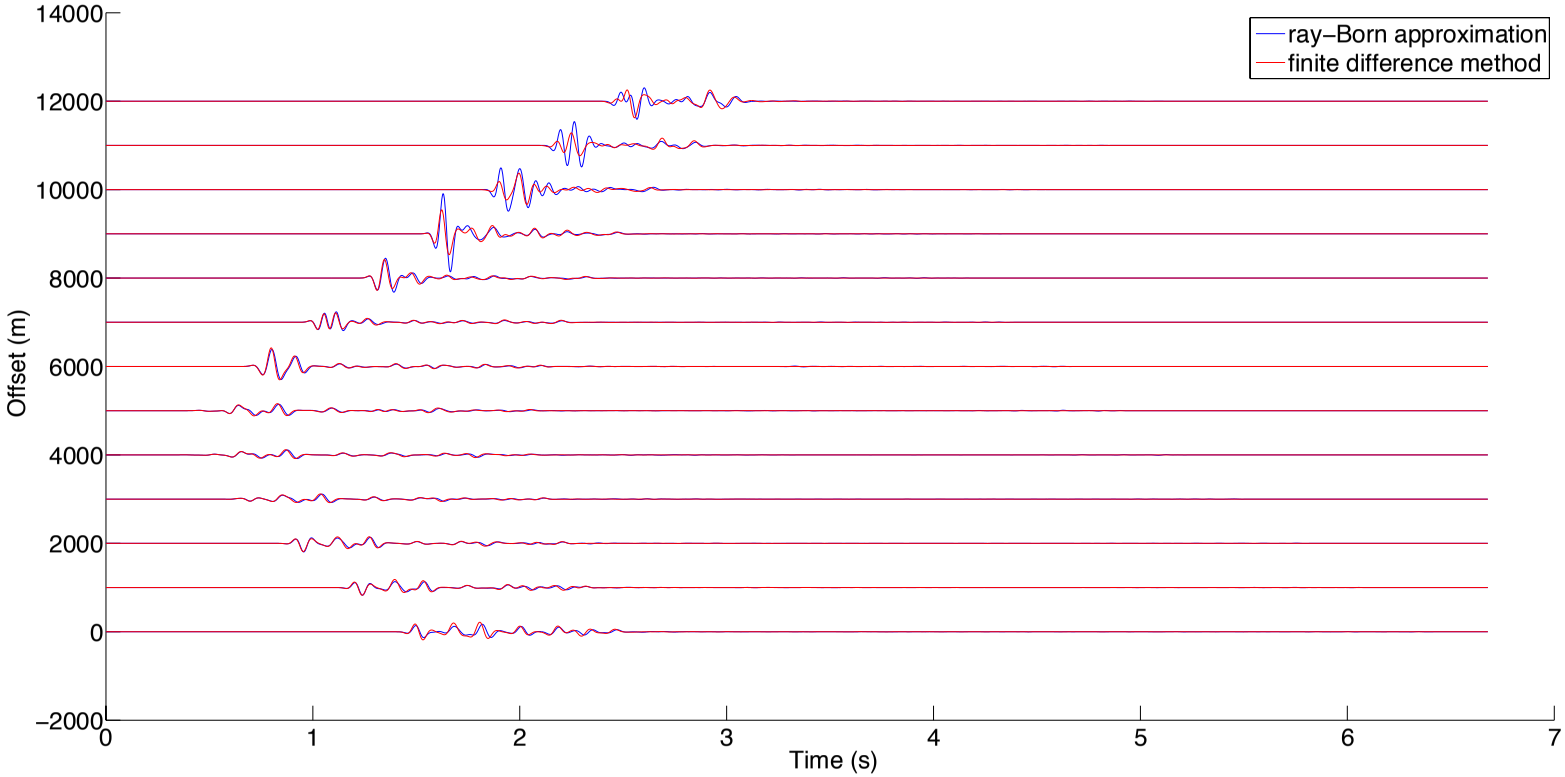

Figure 3.32: Comparison between the Ray-Born approximation and the finite difference method for the SEG/EAGE overthrust model. The source is located at 4 km offset while the receivers are located at offset ranging from 1 to 12 km.

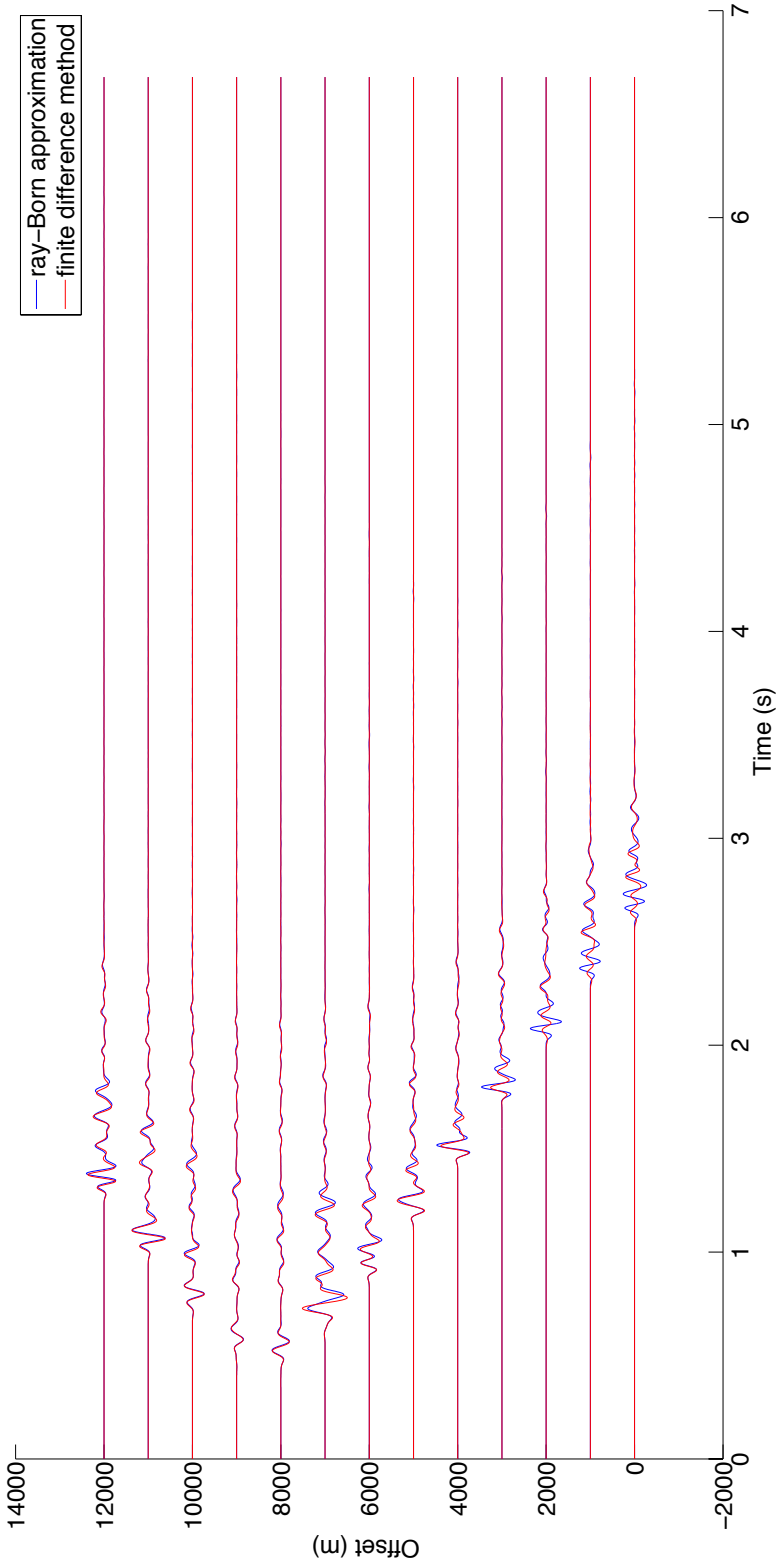

Figure 3.33: Comparison between the Ray-Born approximation and the finite difference method for the SEG/EAGE overthrust model. The source is located at 8 km offset while the receivers are located at offset ranging from 1 to 12 km.

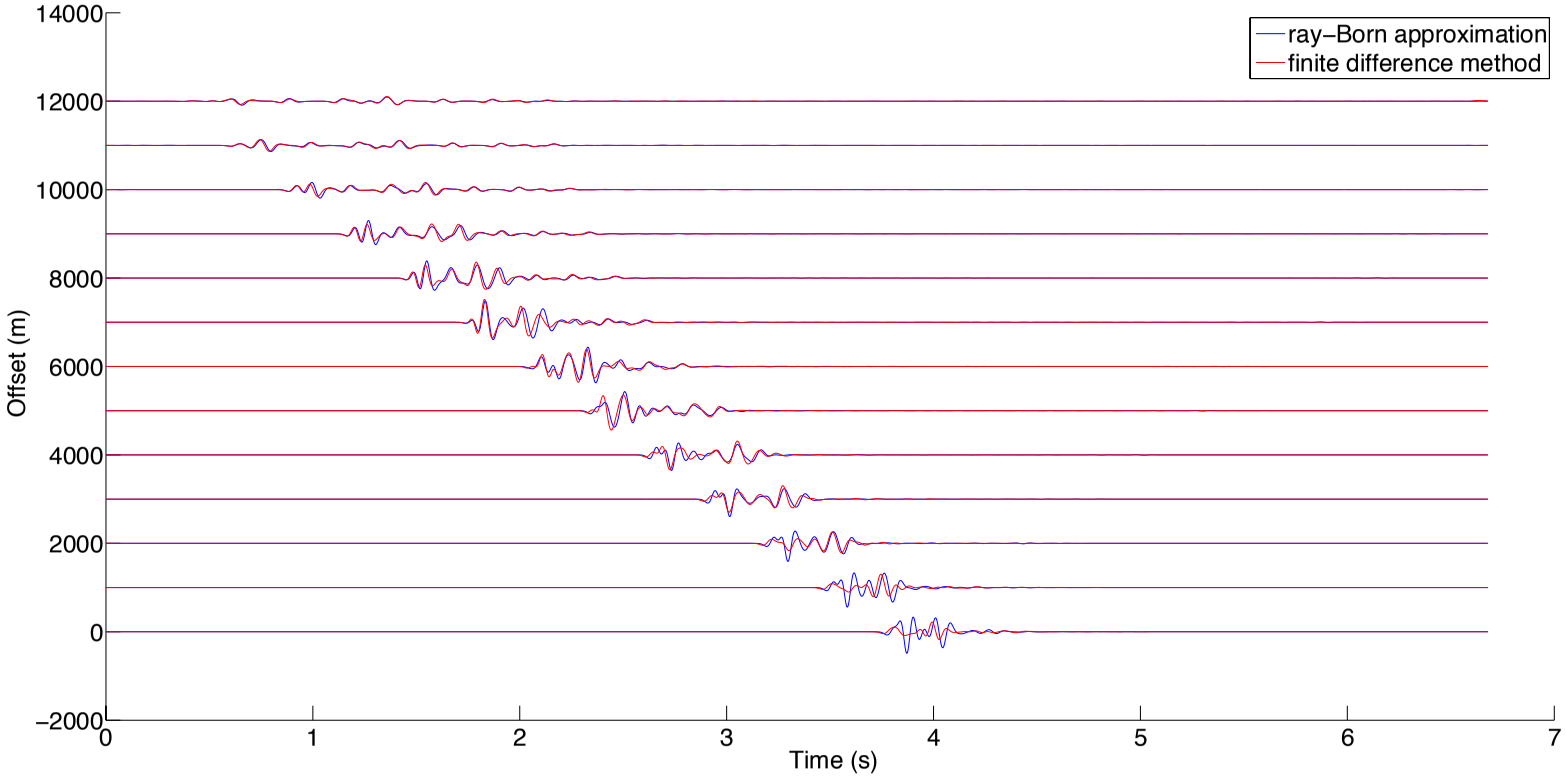

Figure 3.34: Comparison between the Ray-Born approximation and the finite difference method for the SEG/EAGE overthrust model. The source is located at 12 km offset while the receivers are located at offset ranging from 1 to 12 km.

cost of using the ray-Born approximation is a factor of two lower than the finite difference method for the specific geometries and models used in this thesis. In geometries where the same number of sources and receivers are present, the ray-Born approximation can be as much as a factor of 40 times faster. Another benefit is that raytracing only needs to be performed once for a given background model. This means that any number of scatterers could be reproduced in the same background model when using the ray-Born approximation, whereas the complete wavefield needs to be computed every time when using the finite difference method. Due to these properties, the ray-Born approximation is evaluated to be able to act as a good replacement for the finite difference method in forward modelling and in full waveform inversion.

Chapter 4

Inversion Theory

4.1 Outline

In this chapter I present the background theory for full waveform inversion. The act of performing full waveform inversion consists of finding a seismic velocity model given seismic data recorded at the surface. The method used to perform inversion as well as the regularization used to stabilise the result will be discussed.

4.2 Inversion

The derivation of inverse theory in this chapter follows Menke (1984), Tarantola (2005) and Aster et al. (2012). The forward modelling problem can be expressed in the following way:

$$G(\mathbf{m}) = \mathbf{d}, \tag{4.1}$$

where $\mathbf{m}$ is the model, $\mathbf{d}$ is the synthetic data and G is the forward modelling operator. The goal of the forward modelling problem is to compute the synthetic data, $\mathbf{d}$ given the model, $\mathbf{m}$ and the forward operator, G. Examples of models can be the seismic velocity models expressed in chapter 3 and examples of forward operators can be the ray-Born approximation discussed in chapter 2 or the finite difference method discussed in chapter 3. For a given velocity model, the synthetic seismogram can be computed by either of the forward modelling methods. For a given model and a given forward operator one unique solution exists. The forward modelling problem stated in equation (4.1) can be written in the form of a linear system of algebraic equations:

$$\mathbf{Gm} = \mathbf{d}, \tag{4.2}$$

where $\mathbf{G}$ is a forward modelling operator. The focus of this chapter is to solve the inverse problem which involves finding the model, $\mathbf{m}$, given the data, $\mathbf{d}$. The inverse problem is more difficult to solve than the forward modelling problem for several reasons; Due to the presence of noise in the data or because the forward operator is approximate there may not exist a model that exactly fits the data. Another problem is that there exists many models that satisfy the same data. As a result, the inverse problem does not have an unique solution and it is difficult to determine the accuracy of the result. In addition, small changes in the data can result in large changes in the estimated model. Inverse problems with these instabilities are referred to as ill-conditioned problems. In the following sections we will discuss how inverse problems are solved and how they can be made more stable by the use of regularization.

4.3 Least Squares Solution

A reasonable approach to solving the inverse problem is to find a best approximate solution to the model $\mathbf{m}$ that minimizes some misfit measure, computed from the differences between the observed

data and a theoretical prediction of the forward problem. The misfit between the observed data and the theoretical predicted data are called residuals. The most used strategy is to find the model that minimises the 2 norm (or least squares norm) of the residual vector:

$$||\mathbf{d} - G(\mathbf{m})||_2 = \sqrt{\sum_{i=1}^{m}(d_i - G(m)_i)^2}. \tag{4.3}$$

The least square solution of a linear system is used in cases where there is no solution $\mathbf{m}$ that satisfies equation (4.2) exactly. The problem arises in cases where the dimension of $\mathbf{G}$ in equation (4.2) is smaller than the dimension of the model, $\mathbf{m}$. The goal is then to find an approximate model $\hat{\mathbf{m}}$ that minimises $||\mathbf{d} - \mathbf{G}\hat{\mathbf{m}}||$. From Lay (1994) we have that the least squares solution is derived as follows. Given $\mathbf{G}$ and $\mathbf{d}$, let $\mathbf{d}$ be projected onto the subspace Col $\mathbf{G}$:

$$\hat{\mathbf{d}} = \mathbf{proj}_{Col\mathbf{G}}\mathbf{d}. \tag{4.4}$$

Since $\hat{\mathbf{d}}$ is in the column space of $\mathbf{G}$, the equation $\mathbf{G}\mathbf{m} = \hat{\mathbf{d}}$ is consistent and there exists an $\hat{\mathbf{m}}$ such that:

$$\mathbf{G}\hat{\mathbf{m}} = \hat{\mathbf{d}}. \tag{4.5}$$

If $\hat{\mathbf{m}}$ satisfies $\mathbf{G}\hat{\mathbf{m}} = \hat{\mathbf{d}}$, the projection $\hat{\mathbf{d}}$ has the property that $\mathbf{d} - \hat{\mathbf{d}}$ is orthogonal to the column Col $\mathbf{G}$, so $\mathbf{d} - \mathbf{G}\hat{\mathbf{m}}$ is orthogonal to each column of $\mathbf{G}$. If $\mathbf{G}_j$ is any column of $\mathbf{G}$, then $\mathbf{G}_j \cdot (\mathbf{d} - \mathbf{G}\hat{\mathbf{m}}) = 0$ and $\mathbf{G}_j^T \cdot (\mathbf{d} - \mathbf{G}\hat{\mathbf{m}}) = 0$. Since each $\mathbf{G}_j^T$is a row of $\mathbf{G}^T$,

$$\mathbf{G}^T \cdot (\mathbf{d} - \mathbf{G}\hat{\mathbf{m}}) = 0, \tag{4.6}$$

and

$$\mathbf{G}^T\mathbf{G}\mathbf{m} = \mathbf{G}^T\mathbf{d}. \tag{4.7}$$

The matrix equation represents a system of equations called the normal equations for $\mathbf{G}\mathbf{m} = \mathbf{d}$. An expression for the model $\mathbf{m}$ is from the normal equations given as:

$$\mathbf{m} = (\mathbf{G}^T\mathbf{G})^{-1}\mathbf{G}^T\mathbf{d}. \tag{4.8}$$

$\mathbf{G}^T\mathbf{G}$ has an inverse as it is square. $\mathbf{G}$ is not always square and does therefore not always have an inverse.

4.4 Regularization

The solution obtained from the least square solution can be made more stable by using Tikhonov regularization, which is a very easily implemented technique for regularizing discrete ill-conditioned

problems. When using Tikhonov regularization, we consider all the solutions with $||\mathbf{d} - \mathbf{Gm}||_{\mathbf{2}} \leq \delta$, and select the one that minimises the norm of $\mathbf{m}$. We wish to minimise the norm of $\mathbf{m}$ in order to arrive at a solution that contains sufficient model feature complexity but still manages to adequately fit the data. This minimisation is achieved by considering the problem as a damped least squares problem.

$$min||\mathbf{d} - \mathbf{Gm}||_2^2 + \alpha^2||\mathbf{m}||_2^2, \tag{4.9}$$

where α is a regularisation parameter between zero and one. For such problems, the normal equations can be expressed as:

$$(\mathbf{G}^T\mathbf{G} + \alpha^2\mathbf{I})\mathbf{m} = \mathbf{G}^T\mathbf{d}, \tag{4.10}$$

where $\mathbf{I}$ is the identify matrix and α is the regularization parameter controlling the damping. While the zeroth order Tikhonov regularization will minimise the norm of $\mathbf{m}$, higher order Tikhonov regularization can be used to minimise other features of the solution of $\mathbf{m}$. The least square problem will then take the following form:

$$min||\mathbf{d} - \mathbf{Gm}||_2^2 + \alpha^2||\mathbf{Lm}||_2^2. \tag{4.11}$$

$\mathbf{L}$ can be expressed as the first or second derivative of $\mathbf{m}$, reflecting a preference for either a flat or a smooth model. In this thesis, zeroth order and second order Tikhonov regularization has been used, resulting in the following formulation of the normal equations:

$$(\mathbf{G}^T\mathbf{G} + \alpha^2\mathbf{I} + \beta^2\mathbf{L})\mathbf{m} = \mathbf{G}^T\mathbf{d}. \tag{4.12}$$

The model $\mathbf{m}$ can then be expressed as:

$$\mathbf{m} = (\mathbf{G}^T\mathbf{G} + \alpha^2\mathbf{I} + \beta^2\mathbf{L})^{-1}\mathbf{G}^T\mathbf{d}, \tag{4.13}$$

where α is the regularisation parameter controlling the damping and β is regularization parameter controlling the smoothing of $\mathbf{m}$. α will allow us to control how much the model changes for each iteration of the inversion, making sure that the model does not change too much, too fast. β will allow us to control the smoothness of the model, which will decide how sharp features it is possible to resolve.

4.5 Iterative Method

When solving linearized inverse problems it is often convenient to use an iterative method to solve the problem. Iterative methods are used because the inversion result from one iteration is only an approximate solution due to the linearization. Iterative inversion methods consist of computing a sequence of trial solutions that gradually converge towards a final solution. One starts with a model

$\mathbf{m}^{(0)}$ and then move to the updated model $\mathbf{m}^{(1)}$. Similarly one starts with the data $\mathbf{d}_{(0)}$ that is computed as the contrast between the data from the real model and the the starting model $\mathbf{m}^{(0)}$, and then move to the updated data $\mathbf{d}_{(1)}$ that is computed as the contrast between the data from the real model and the updated model $\mathbf{m}^{(1)}$. The updated model is computed using the following equation:

$$\mathbf{m}^{i+1} = \mathbf{m}^{i} + (\mathbf{G}_i^T \mathbf{G}_i + \alpha^2 \mathbf{I} + \beta^2 \mathbf{L})^{-1} \mathbf{G}_i^T \mathbf{d}_i, \tag{4.14}$$

and the updated data is computed using:

$$\mathbf{d}_{i+1} = \mathbf{d}_{Real} - \mathbf{G}_{i+1} \mathbf{m}^{i+1}. \tag{4.15}$$

The process of computing the updated model and the updated data can be repeated for as many iterations as required to accurately retrieve the real model. Solving inverse problems by linear approximation is however not without disadvantages. If the starting model $\mathbf{m}^{(0)}$ is not sufficiently close to the real model $\mathbf{m}$, the linear approximation of the inverse may not be a good one. In such cases the the sequence of trial solutions will not converge towards the true solution and the solution obtained will be inaccurate. In the next chapter an iterative inversion algorithm using the regularised least squares solution will be presented and discussed.

Chapter 5

Inversion Implementation

5.1 Outline

In this chapter full waveform inversion using the ray-Born approximation will be discussed; Both the implementation as well as the cost and accuracy of the method. The method will be applied to the SEG/EAGE overthrust model and the optimal regularization parameters, source/receiver spacing and geometry will be identified. The result will be compared with a frequency domain finite difference waveform inversion that is discussed in Sourbier et al. (2009a) with numerical examples shown in Sourbier et al. (2009b). The results from the different methods will be compared and discussed.

5.2 Full Waveform Inversion Implementation

The goal of full waveform inversion is to reproduce a velocity model of the subsurface by using seismic data $P(\mathbf{x_s}, \mathbf{x_r}, t)$ from a seismic survey. In this section I will discuss how seismic waveform inversion can be performed by using the ray-Born approximation as the primary forward modelling method. The inversion algorithm holds some similarities to traditional full waveform inversion algorithms (e.g Pratt et al. (1998), Operto et al. (2006), Sourbier et al. (2009a) and Sourbier et al. (2009b)) but it is different in the way it performs the inversion and updates the model. The waveform inversion is implemented in the frequency domain, but some of the forward modelling has been performed in the time domain. Figure 5.1 shows a flowchart illustrating the implementation of the waveform inversion.

The data is simulated in velocity model $c(\mathbf{x})$ by using the finite difference method in the time domain. The forward modelling in the velocity model yields the synthetic data $P(\mathbf{x_s}, \mathbf{x_r}, t)$. Full waveform inversion uses the synthetic data $P(\mathbf{x_s}, \mathbf{x_r}, t)$ to compute a seismic velocity model that is as close to the real velocity model $c(\mathbf{x})$ as possible. In order to perform full waveform inversion, a background velocity model $c_0(\mathbf{x})$ which is our best guess to what we believe the subsurface structures look like needs to be created. The background velocity model is usually very smooth as we normally only have a rough idea about the subsurface structures. Forward modelling is then performed in the background velocity model by using the finite difference method to compute the modelled data $P_0(\mathbf{x_s}, \mathbf{x_r}, t)$. The finite difference method is used to compute the synthetic seismogram in the background velocity model because geometrical ray theory alone is unable accurately reproduce the direct wave and the scattering that occurs in the background model. We can now compute the data residual that is given as the difference between the real data and the data generated in the background model.

$$D(\mathbf{x_s}, \mathbf{x_r}, t) = P(\mathbf{x_s}, \mathbf{x_r}, t) - P_0(\mathbf{x_s}, \mathbf{x_r}, t). \tag{5.1}$$

In the frequency domain the data residual is expressed as $D(\mathbf{x_s}, \mathbf{x_r}, t) \rightarrow d(\mathbf{x_s}, \mathbf{x_r}, \omega)$. The data residual is on the same form as generated by the ray-Born approximation. The ray-Born approximation is used to generate synthetic data using a smoothly varying background model $c_0(\mathbf{x})$ and a scatterer $c_1(\mathbf{x})$ where the synthetic seismogram is generated from the contrast between the background model and the scatterer. It is possible to perform full waveform inversion by using the ray-Born approximation

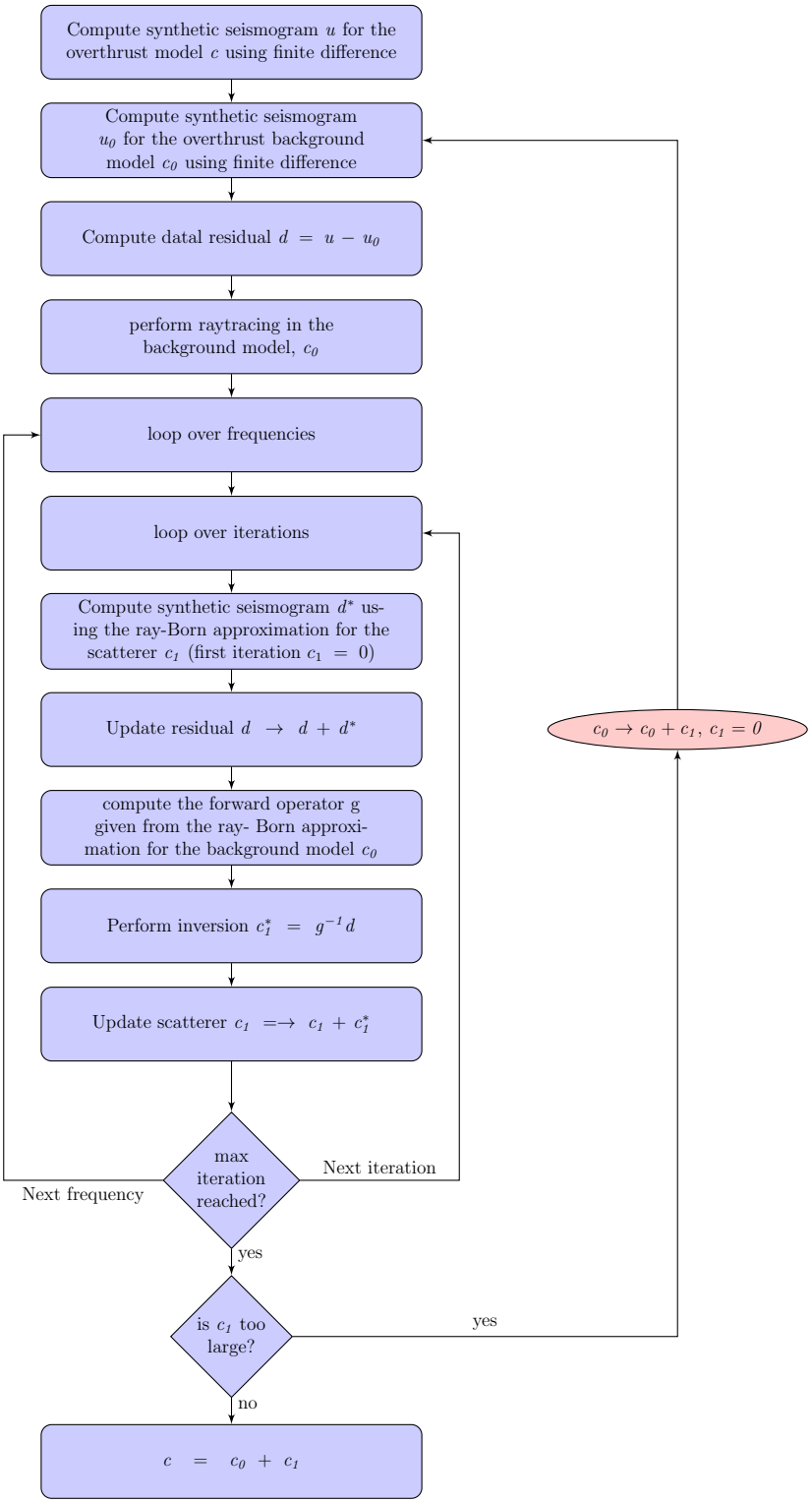

Figure 5.1: Implementation of full waveform inversion using the ray-Born approximation

and the data residual $d(\mathbf{x_s}, \mathbf{x_r}, \omega)$. The scattered wavefield can be written as (e.g Tarantola (1984b)):

$$d(\mathbf{x_s}, \mathbf{x_r}, \omega) = p(\mathbf{x_s}, \mathbf{x_r}, \omega) - p_0(\mathbf{x_s}, \mathbf{x_r}, \omega) = \frac{\partial p(\mathbf{x_s}, \mathbf{x_r}, \omega)}{\partial c(\mathbf{x})}, (c(\mathbf{x}) - c_0(\mathbf{x})) = \frac{\partial p(\mathbf{x_s}, \mathbf{x_r}, \omega)}{\partial c(\mathbf{x})} c_1(\mathbf{x}) \quad (5.2)$$

where $G(\mathbf{x_s}, \mathbf{x_r}, \omega) = \frac{\partial p(\mathbf{x_s}, \mathbf{x_r}, \omega)}{\partial c(\mathbf{x})}$ is the sensitivity matrix. By using the ray-Born approximation ((2.46)), the sensitivity matrix is expressed as:

$$G(\mathbf{x_s}, \mathbf{x_r}, \omega) = 2\omega^2 s(\omega) \int g_0(\mathbf{x_s}, \mathbf{x}, \omega) g_0(\mathbf{x_r}, \mathbf{x}, \omega) c_0^{-3}(\mathbf{x}) d\mathbf{x}. \quad (5.3)$$

By using the sensitivity function, the scattered wavefield $d(\mathbf{x_s}, \mathbf{x_r}, \omega)$ is given as:

$$d(\mathbf{x_s}, \mathbf{x_r}, \omega) = G(\mathbf{x_s}, \mathbf{x_r}, \omega) c_1(\mathbf{x}). \quad (5.4)$$

This equation is here of the form shown in equation (4.1) where $G(\mathbf{x_s}, \mathbf{x_r}, \omega)$ is the forward operator. $d(\mathbf{x_s}, \mathbf{x_r}, \omega)$ is the data and $c_1(\mathbf{x})$ is the model. The equation is solved as a least squares problem with Tikhonov regularization. By applying equation (4.12) the regularised least squares solution becomes:

$$c_1(\mathbf{x}) = (G^T(\mathbf{x_s}, \mathbf{x_r}, \omega) G(\mathbf{x_s}, \mathbf{x_r}, \omega) + \alpha^2 \mathbf{I} + \beta^2 \mathbf{L})^{-1} G^T(\mathbf{x_s}, \mathbf{x_r}, \omega) d(\mathbf{x_s}, \mathbf{x_r}, \omega), \quad (5.5)$$

where α is the damping parameter, β is the smoothing parameter, $\mathbf{I}$ is the identity matrix and $\mathbf{L}$ is a matrix of second derivatives. The least squares problem is solved by using QR factorization. QR factorization solves the linear system by decomposing the sensitivity matrix into a orthogonal matrix Q and an upper triangular matrix R. QR factorization is used because it is fast and efficient for large matrices.

Traditional waveform inversion algorithms (e.g Pratt et al. (1998), Operto et al. (2006), Sourbier et al. (2009a) and Sourbier et al. (2009b)) would at this point do the following operation: $c_0(\mathbf{x}) \rightarrow c_0(\mathbf{x}) + c_1(\mathbf{x})$. This step will update the background velocity model and the entire inversion routine could be repeated. The inversion implemented here is however performed in a slightly different way. Our model now consists of a starting model c_0 and a scatterer c_1. Using these models it is possible to perform forward modelling using the ray-Born approximation. The traveltime and amplitude that was computed by raytracing in the initial background model is used. The synthetic data $d^*(\mathbf{x_s}, \mathbf{x_r}, \omega)$ generated using the ray-Born approximation can be used to update our data residual.

$$d(\mathbf{x_s}, \mathbf{x_r}, \omega) \rightarrow d(\mathbf{x_s}, \mathbf{x_r}, \omega) + d^*(\mathbf{x_s}, \mathbf{x_r}, \omega). \quad (5.6)$$

The new data residual can be used to perform a new inversion iteration using equation (5.5). We can update the scatterer $c_1(\mathbf{x})$ and get a more accurate inversion result.

$$c_1(\mathbf{x}) = c_1(\mathbf{x}) + c_1^*(\mathbf{x}). \quad (5.7)$$

The process of performing waveform inversion (5.5), updating the scatterer (5.7) and updating the data

residual (5.6) can be repeated for as many iterations as required to achieve a satisfactory inversion result. For each iteration $c^*(\mathbf{x}) = c_0(\mathbf{x}) + c_1(\mathbf{x})$ will be more similar to the real model $c(\mathbf{x})$. In the first inversion iteration, the scatterer c_1 is equal to zero and the data generated using the ray-Born approximation is equal to zero. The data is therefore generated using the finite difference method only in the first iteration. The traveltime and amplitude computed using raytracing in the initial background model can be used for the entire inversion. This will greatly reduce the computation time of the forward modelling compared to traditional approaches. If the velocity contrast of the scatterer c_1 relative to the background model becomes too large, it is possible to update the starting model:

$$c_0(\mathbf{x}) = c_0(\mathbf{x}) + c_1(\mathbf{x}), \tag{5.8}$$

set $c_1(\mathbf{x}) = 0$ and start over again by performing forward modelling using finite difference in the new background model $c_0(\mathbf{x})$. This process will however make the inversion process more time-consuming.

5.3 Inversion Iterations

The inversion has been implemented by iterating over nine frequencies between 2 Hz and 20 Hz. Two iterations are performed for each frequency. It is expected that there is a higher offset between the data for high frequencies than for low frequencies. If the difference between the data from the real model and the background model is too large, then the inversion result will become inaccurate. It is therefore useful to invert for the low frequencies first and then gradually increase the frequency. As the frequency increases the model will gradually become more accurate and the resolution in the model increases, thus making sure that the data from the background model is as close to the data from the real model as possible. Due to traveltime inaccuracy when using the ray-Born approximation to perform the inversion, it is performed with a few low frequencies after the high frequencies. This is done because the relative difference between the ray-Born approximation and the finite difference method is less at low frequencies than at high frequencies as seen in chapter 3. Tests show that this will improve the inversion result. Two sets of inversion iterations have been used. The first inversion iteration set is seen in Table 5.1. This is a basic inversion iteration scheme that is used to find the optimal source/receiver geometry and the regularization parameters. In the basic inversion iteration scheme, two iterations are performed for each frequency from low to high frequency before doing some iterations at low frequency again. The second inversion iteration set can be seen in Table 5.2. This is an advanced inversion iteration scheme that is used to obtain the best inversion result after the best regularization parameters and the best source/receiver geometry have been identified. When using this advanced inversion iteration scheme we perform the waveform inversion as done previously, but instead of stopping after we reach the final iteration, we update the background velocity model, perform a new finite difference iteration and perform raytracing in the new background velocity model. This will result in more accurate waveforms when using an extra finite difference iteration that will decrease multi scattering effects. It will also result on more accurate travel times and amplitudes from

the raytracing.

Frequency	2	4.25	6.5	8.75	11	13.25	15.5	17.75	20	2	4.25	6.5
Number of iterations	2	2	2	2	2	2	2	2	2	2	2	2

Table 5.1: basic inversion iteration scheme

Order	1	2	3
Action	Inversion using Table (5.1)	finite difference in updated $c_0(\mathbf{x})$	Inversion using Table (5.1)

Table 5.2: Advanced inversion iteration scheme

5.4 Models

The velocity model that has been used to perform full waveform inversion is the SEG/EAGE overthrust model. Due to the fact that the raytracer used in this thesis does not support multipathing, the SEG/EAGE Overthrust model has been slightly modified in order to reduce the multipathing effects. This modification consisted of reducing the gradient of the velocity model, thereby decreasing the maximum velocity contrast in the model. The model consists of a smoothly varying background model that is shown in figure 3.18 and the full overthrust model shown in figure 3.20. The seismic data for the real velocity model will be generated using the full overthrust model. The goal of the waveform inversion is to reproduce the overthrust model using the background velocity model and the seismic data generated from the overthrust. The model and forward modelling in the model is discussed in more detail in chapter 3.

5.5 Results

5.5.1 Damping and Smoothing Parameters

The stability and accuracy of the waveform inversion depends strongly on the regularization parameters. The regularization parameters determine the damping and smoothing of the solution. The damping parameter is used to minimise the length of the model c_1 and stay close to the stationary model c_0. A high damping value will result in small model variance while a very small damping value will result in large model oscillations. The smoothing parameter is used to minimise the roughness of the model. For large smoothing values, the model will have a low resolution and become very smooth while for a small smoothing value the model will have large variations and high resolution. In order to properly determine the damping and smoothing values, a series of inversions with one iteration have been performed. The results from these inversions were used to compute the L-curve (e.g G. Rodriguesz (2005)) for the damping and smoothing parameters. The smoothing parameter

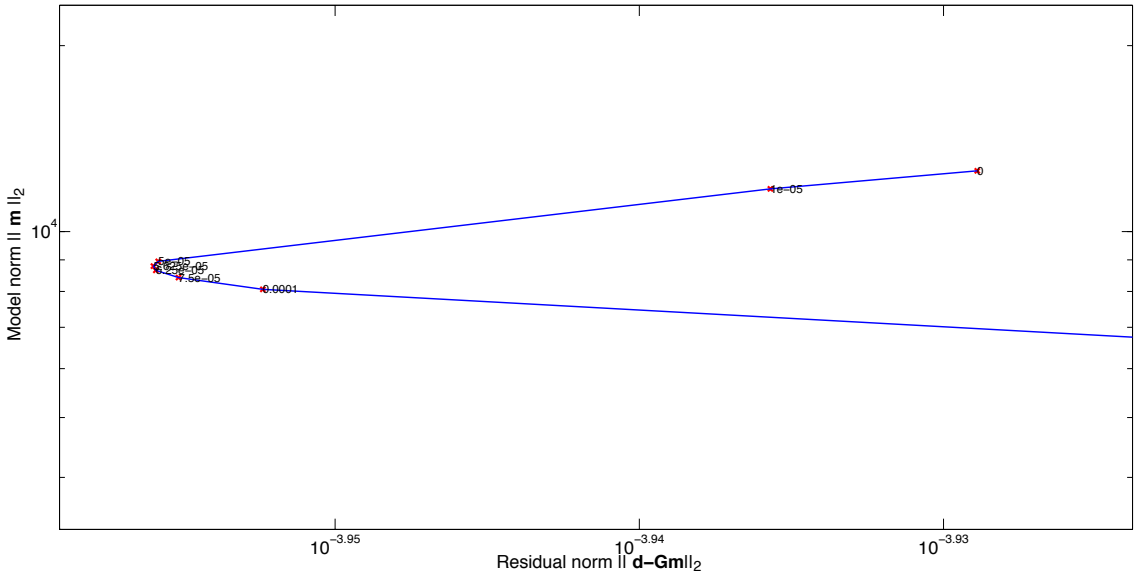

Figure 5.2: L-curve for the damping parameterl

was set to zero while the damping parameter was changed from a value of one to a value of zero as shown in figure 5.2. The damping parameter that gave the lowest data residual while still minimising the length of the model was chosen. The damping parameter was held constant for all iterations. The optimal smoothing parameter was found by using the best damping value and then iterating over smoothing values from one to zero as shown in figure 5.3. The smoothing parameter that gave the lowest data residual while still minimizing the length of the model was chosen. This smoothing value was used as the initial smoothing value for the first frequency. The smoothing was gradually reduced with increasing frequency, as more high resolution structures were identified. This procedure resulted in a stable inversion result with high resolution. In figure 5.4 three different inversion results have been plotted. The top figure shows the result from the waveform inversion when using a damping parameter that is too high. The high damping value resulted in very little change in the model for each iteration of the inversion, the inverted model is therefore very similar to the starting model. The middle figure shows the result from the waveform inversion when using the best damping parameter. The inverted model is very similar to the real overthrust model. The bottom figure shows the result from the waveform inversion when using a damping parameter that is too low. The inverted model has a high resolution and resolves most structures well. The inversion result is however very noisy and some unrealistic features are present in the inversion result. These inversion results illustrate the importance of choosing the best damping and smoothing parameter to obtain the best inversion result possible.

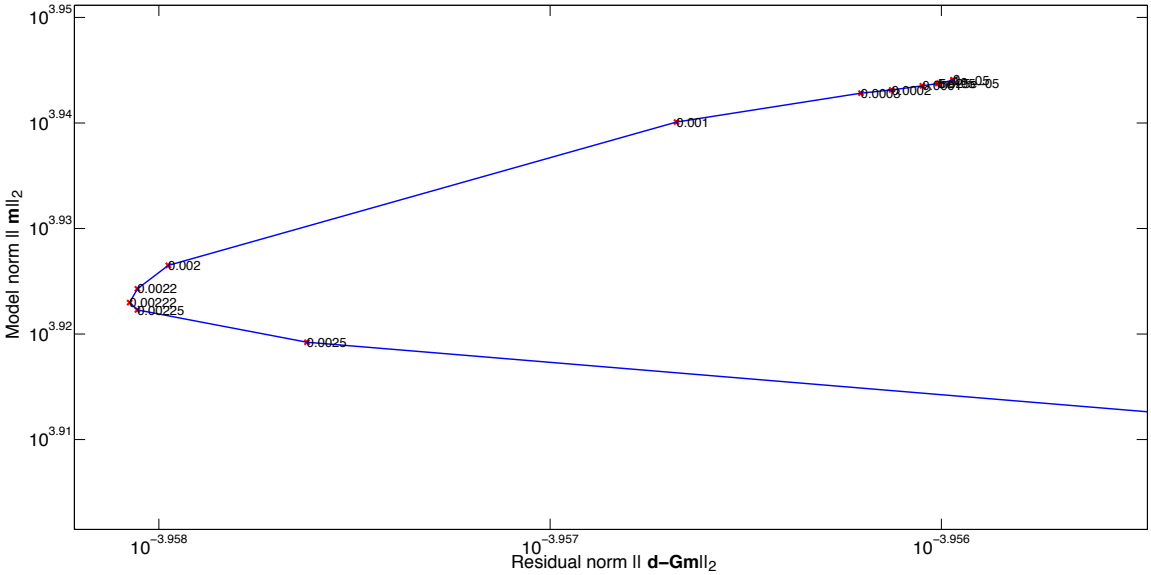

Figure 5.3: L-curve for the smoothing parameterl

5.5.2 Source and Receiver Geometry

The cost and accuracy of the waveform inversion is greatly affected by the spacing between sources and receivers. A very large receiver spacing will result in a very fast inversion while the accuracy of the inverted model will be low. A very small receiver spacing will result in a slower and more memory consuming inversion while the accuracy of the inverted model will be higher. Inversions have been performed with receiver spacings from 200 m to 1800 m in order to evaluate the model error with increasing receiver spacing. Figure 5.5 shows that the error between the real model and the inverted model is increasing with increasing receiver spacing. The model error does not change much when increasing the receiver spacing from 200 m to 400 m. For receiver spacings higher than 400 m, a roughly linear trend in error increase can be observed with increasing receiver spacing. Figure 5.6 shows the inversion result when using three different receiver spacings in order to visualise the effect of changing the receiver spacing. In the upper figure a receiver spacing of 1800 m has been used. The structures in the model are reproduced poorly and a significant ringing can be observed in the inversion result. In the middle figure a receiver spacing of 1000 m has been used. The structures are more accurately reproduced and the ringing is reduced. In the lower figure a receiver spacing of 200 m has been used. The structures are accurately reproduced and the ringing is completely removed. These results tell us that in order to accurately reproduce structures in the subsurface, you need to have sufficiently low source and receiver spacing. If only a rough image of the subsurface is required, higher source and receiver spacings can be used. The inversion will then be much faster, but the result will be that much more inaccurate.

The source and receiver spacing of the inversion can be further optimized. If we look at the forward modelling performed for the overthrust model in chapter 3 in figures 3.31, 3.32, 3.33 and 3.34 it is

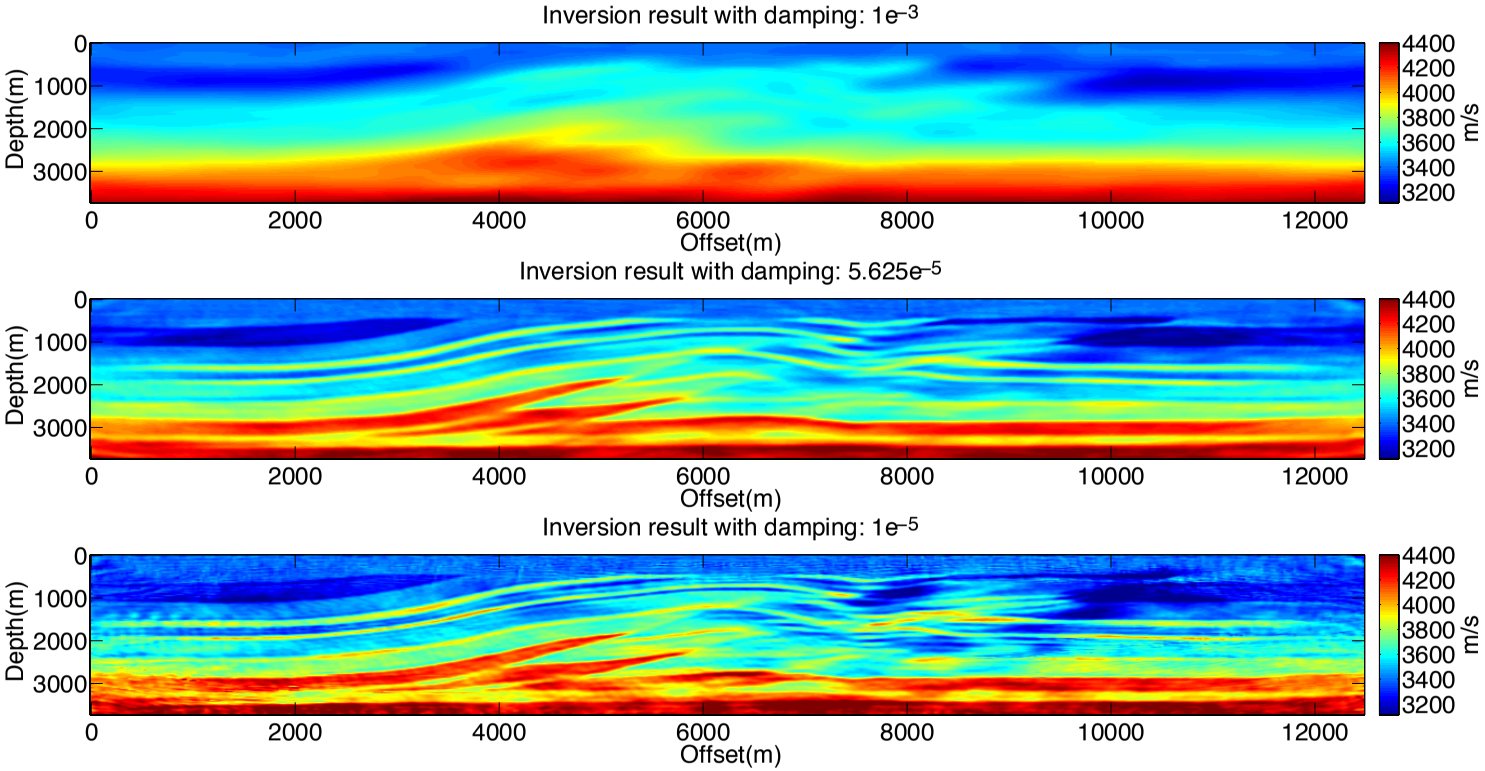

Figure 5.4: Waveform inversion using different damping parameters

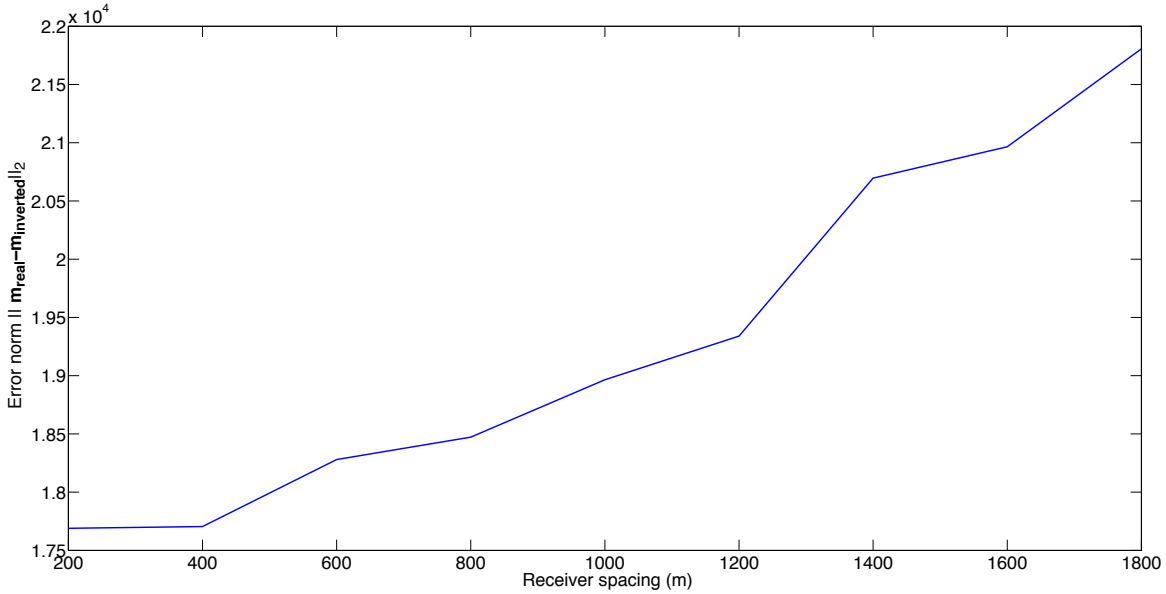

Figure 5.5: Correlation between receiver spacing and inversion accuracy

possible to see that the ray-Born approximation inaccurately reproduces the wavefield at offsets higher than 5 km from the source position. This error will affect the accuracy of the inversion and will yield a more inaccurate model. For each source, we can therefore limit the number of receivers and only include receivers that are closer than 5 km from the source. This will increase the accuracy of the forward modelling in the inversion and will lead to a more accurate inversion result. The number of receivers for each source will be less, but the inverted model will be more accurately reproduced. In figure 5.7 the optimised geometry has been used. It can be seen that the all the layers are more clearly defined, the velocities are more correct and the result contains less noise.

5.5.3 Inversion Optimization

In the previous sections we have found the optimal regularization parameters and the optimal source and receiver geometry. We will now discuss how to obtain the best inversion result possible for the discussed method and model. Up to this point we've only been using the travel times and amplitudes that were computed in the original background velocity model. This will limit the maximum velocity contrast from the background model that it is possible to obtain from the inversion. It is possible to improve the inversion result by using the inversion iteration scheme given in Table 5.2. When using this advanced inversion iteration scheme we perform the waveform inversion as done previously, but instead of stopping after we reach the final iteration, we update the background velocity model, perform a new finite difference iteration and perform raytracing in the new background velocity model. This will result in more accurate waveforms when using an extra finite difference iteration that will decrease multi scattering effects. It will also result on more accurate travel times and amplitudes from the raytracing. We can then continue with the new background velocity model and perform the inver-

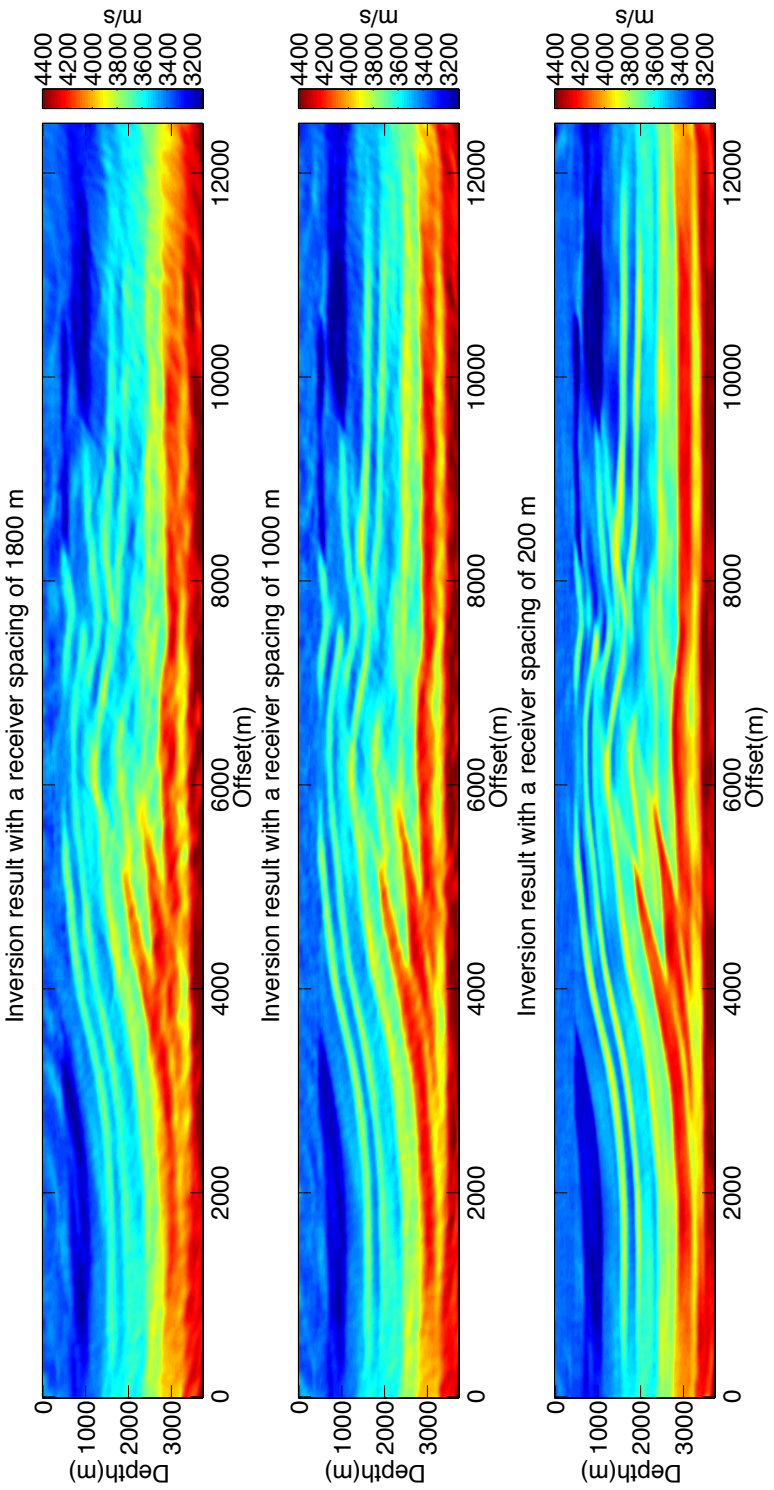

Figure 5.6: Waveform inversion using different receiver spacings

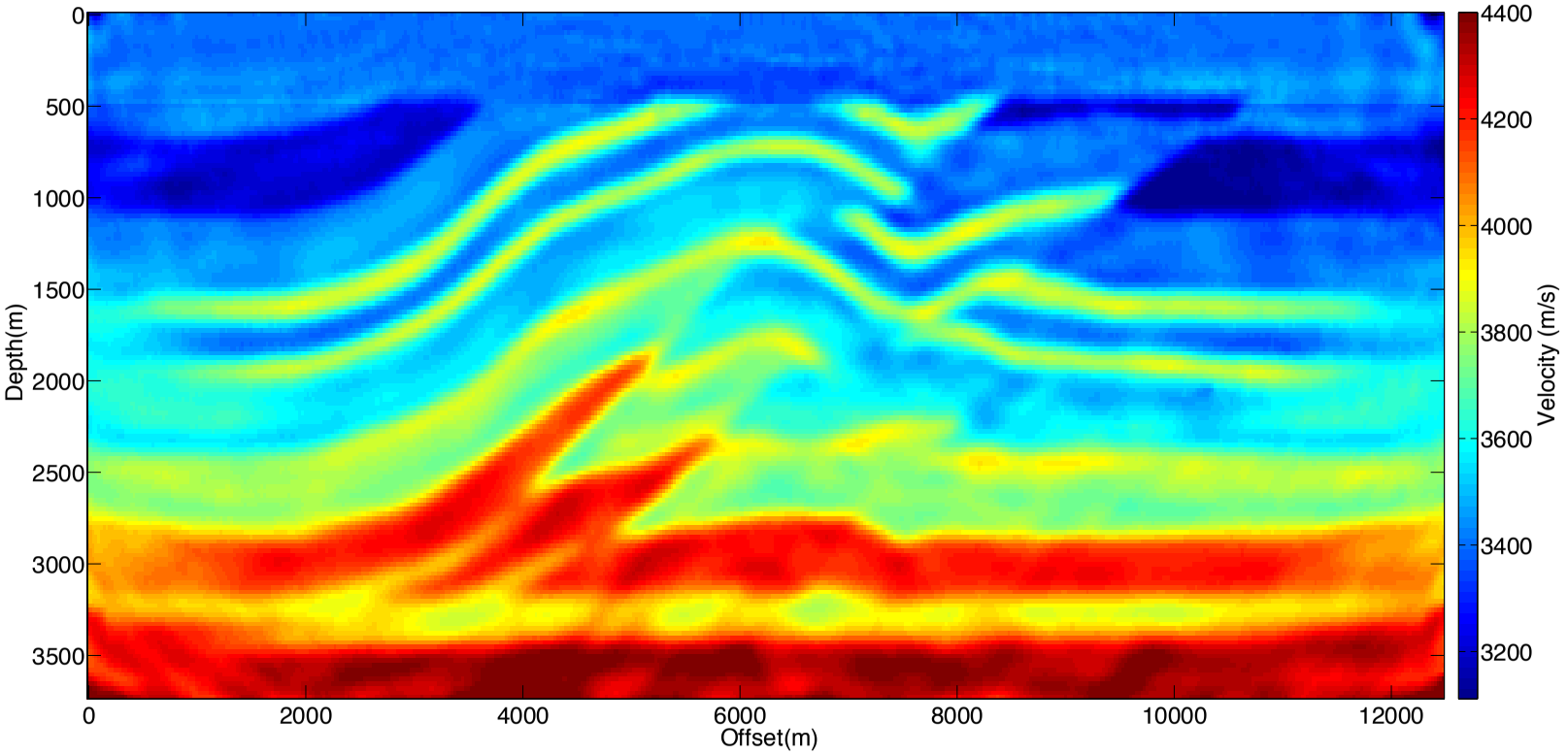

Figure 5.7: Waveform inversion using a optimised receiver geometry. For each source, only receivers that are closer to the source than 5 km have been used.

sion all over again with a more accurate starting model. The improved inversion result is plotted in figure 5.8. It is possible to see some improvements compared to the inversion result achieved in figure 5.7. The first difference is that the velocity contrasts between the layers in the model are stronger, indicating that the peak velocities in the model are more accurately reproduced. The second difference is that the near surface constant velocity layer is more accurately reproduced.

In figure 5.9 the model residual has been plotted with increasing number of iterations. The model residual is given as the norm of the real model minus the inverted model. The blue line shows how the model residual changes with increasing iterations while the red line separates the iterations before and after the finite difference iteration. In the first ten iterations a rapid decrease in model residual can be observed. A slight increase in model residual can be observed up to iteration number 18 before a rapid decrease in model residual is observed. This rapid decrease in model residual occurs when the frequency goes from 20 Hz and back down to 2 Hz. At iteration 24 a new finite difference iteration is performed and a new raytracing is performed in the updated background velocity model. This will improve the travel times and amplitudes for the inversion, allowing for a more accurate reproduction of the model. Only a small decrease in model residual is observed after the finite difference iteration, indicating that the ray-Born approximation inversion is already giving a very good result without having to perform a second finite difference iteration and update the traveltime and amplitude in the model.

In figure 5.10 the data residual has been plotted with increasing number of iterations. The green line separates the iterations performed for each frequency, the blue line separates the data residual that was computed before the second finite difference iteration and after the second finite difference iteration and the red dots indicate the actual data residual per iteration. From the figure it is seen that the data residual for a given frequency is decreasing with increasing number of iterations for that frequency. The blue line that is separating the iterations performed before and after the second finite difference iteration show a large decrease in data residual after the second finite difference iteration for most frequencies. This large decrease in data residual is caused as a combination of having more accurate travel times and amplitude from the raytracing and having more accurate waveforms from the finite difference method. More iterations have been performed for low frequencies than for high frequencies as tests indicated that this gave a better inversion result.

5.5.4 Comparing the ray-Born Inversion with the Finite Difference Inversion

We will now perform a comparison between the inversion result achieved by using the ray-Born approximation with an inversion result achieved by using the finite difference method. The finite difference full waveform inversion algorithm used to generate the inversion result is called FWT2D and its implementation is discussed in Hustedt et al. (2004) and Sourbier et al. (2009a) with numerical examples

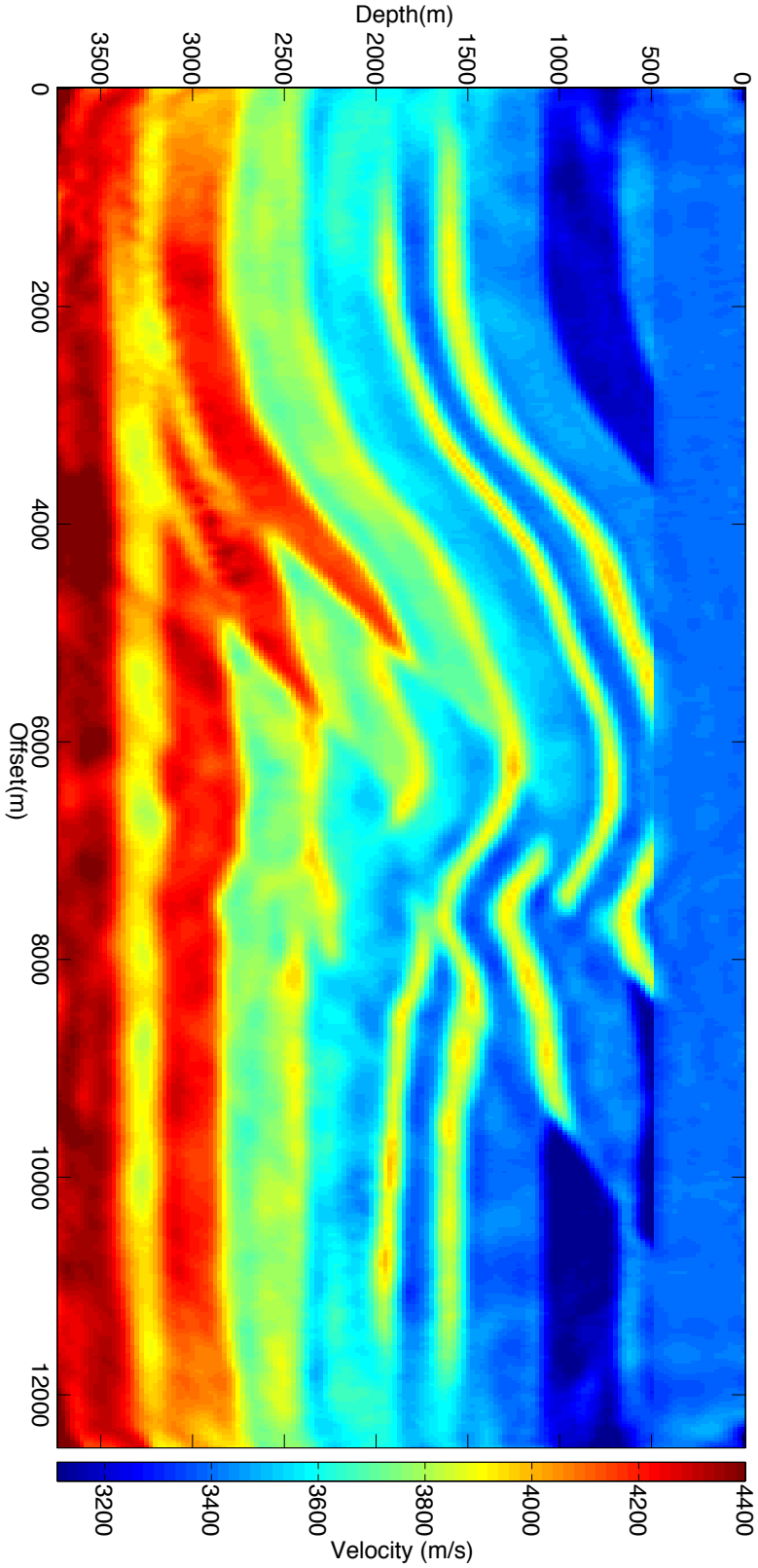

Figure 5.8: Waveform inversion using a optimised receiver geometry and two finite difference iterations

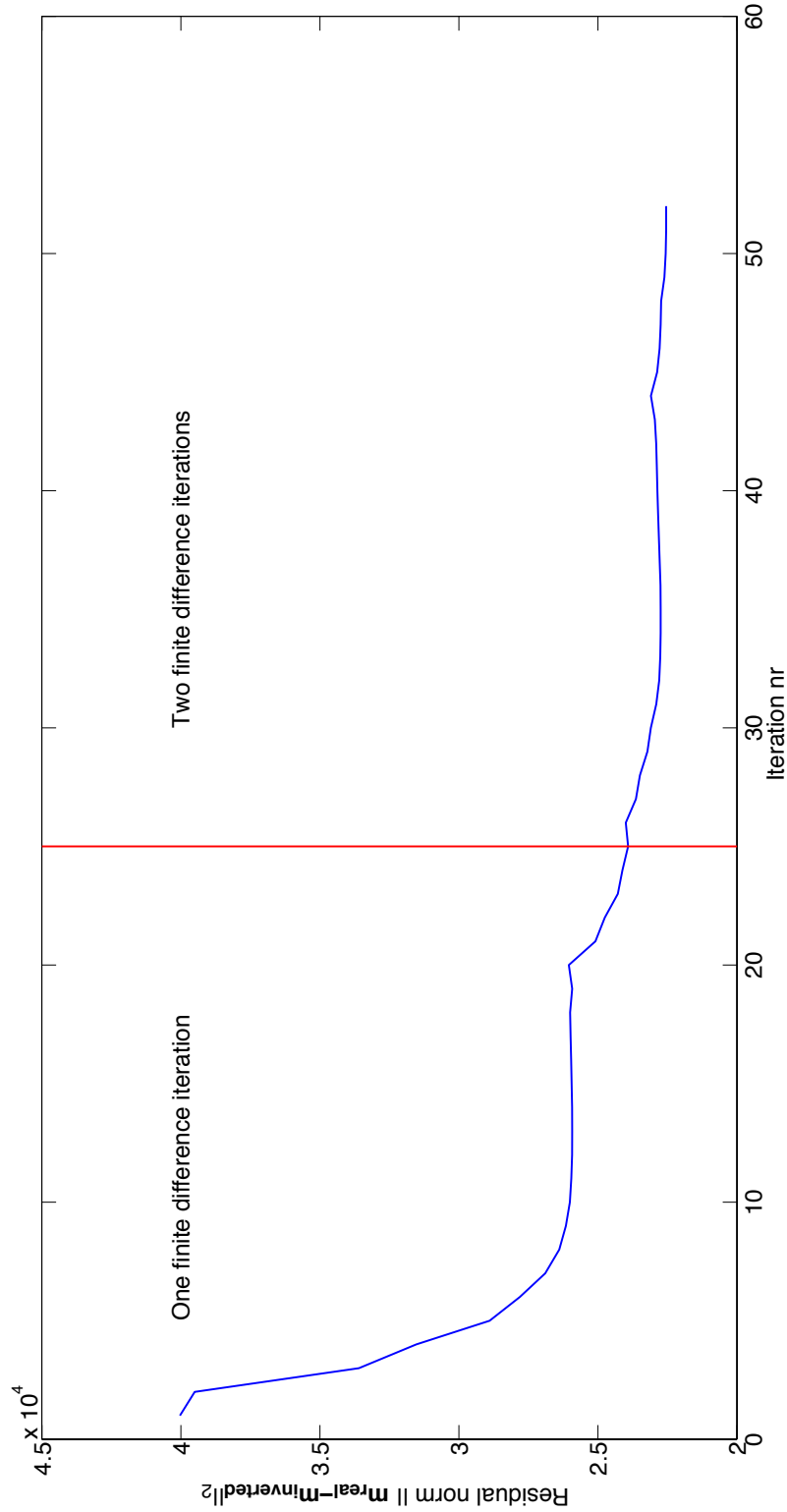

Figure 5.9: Model residual with increasing number of iterations

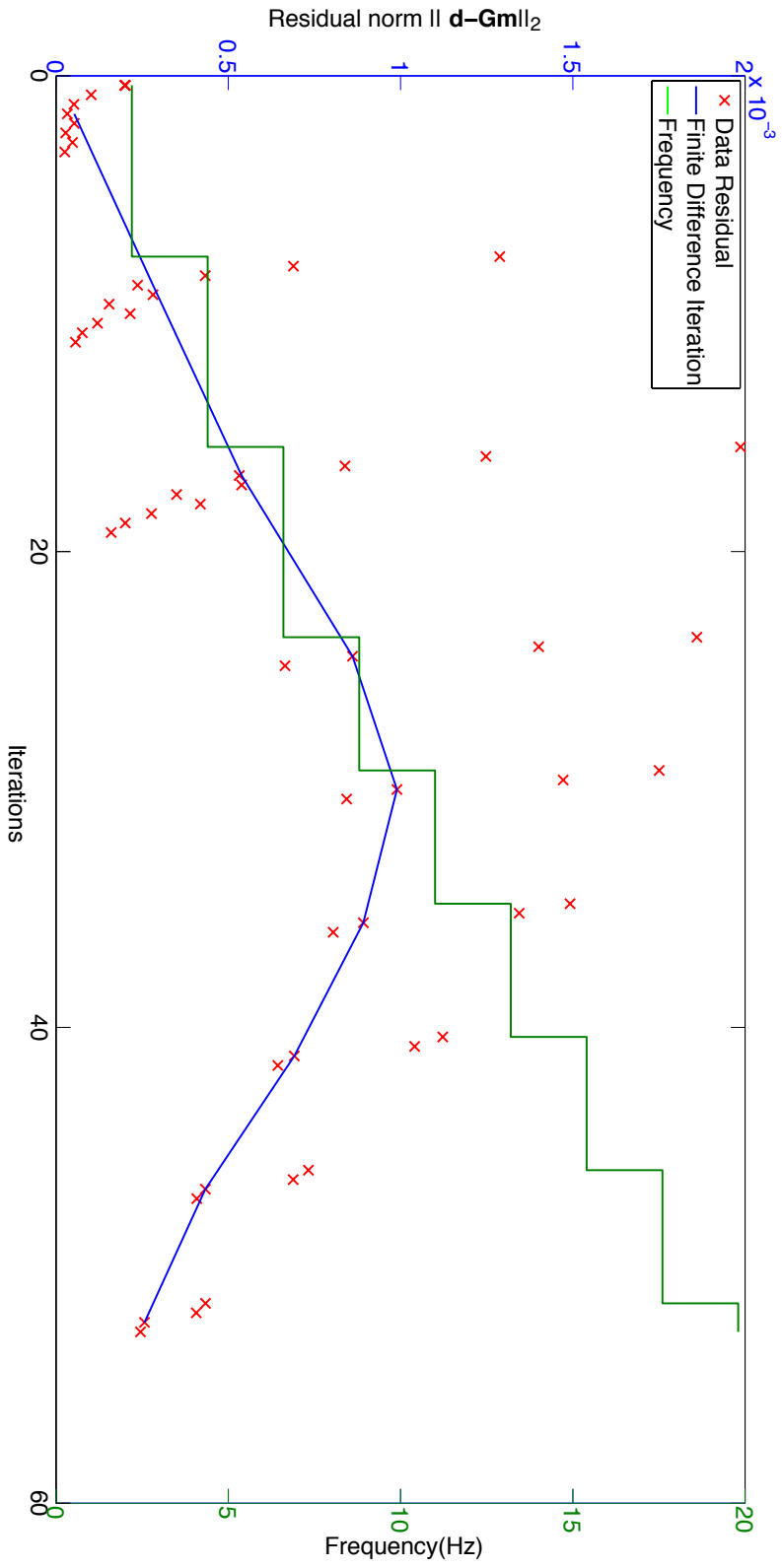

Figure 5.10: Data residual with increasing number of iterations

shown in Sourbier et al. (2009b). In figure 5.11 the inversion result using only the FWT2D method has been plotted. The inversion result is very similar to what we achieved when using the ray-Born approximation inversion seen in figure 5.8. Some differences can however be observed. At first glance it can be seen that the small thin layers are better resolved when using the FWT2D inversion. The velocity contrasts within the layers are smaller and the boundary between layers are more clearly defined. In figure 5.12 the real velocity model minus the ray-Born approximation inversion result has been plotted. In figure 5.13 the real velocity model minus the FWT2D inversion result has been plotted. From the figures it can be seen that both methods have problems reproducing the velocity model in the boundaries of the model. The ray-Born approximation inversion result has a slightly better defined velocity structure at the boundaries. The FWT2D inversion reproduces the central parts of the model very well while the ray-Born approximation inversion has problems with reproducing the velocity in the lower part of each layer. In figure 5.14 three 1-D profiles have been plotted for the starting model, the real model, the ray-Born approximation inversion and the FWT2D inversion. The inversion result obtained using the ray-Born approximation and FWT2D are very similar. In most areas both methods reproduce the real model very well. The exception is that the ray-Born approximation inversion in a few areas reproduces a lower peak velocity than the FWT2D method inversion. The results from this comparison shows that the ray-Born approximation will give a very good inversion result when compared to the FWT2D method and that it is a viable replacement for the finite difference method in waveform inversion.

5.6 Computation Time

Synthetic seismograms have been generated for the SEG/EAGE Overthrust background velocity model using the finite difference method and the ray-Born approximation for all source/receiver pairs. The finite difference method is a factor of 10 times slower than the ray-Born approximation for this given model. In the case of full waveform inversion using the finite difference method, the wavefield needs to be solved for each source and then the residuals need to be backwards propagated through the model for each receiver. This means that when performing 1 inversion iteration, the finite difference method is a factor of 20 slower than the ray-Born approximation. Assuming that the basic inversion iteration scheme was used (Table 5.1), a total number of 24 iterations need to be performed. As raytracing only needs to be performed for the first inversion iteration, the computation time of the waveform inversion using only the finite difference method implemented in this thesis is roughly 480 times higher than when using the ray-Born approximation inversion discussed in this chapter. This is a very large difference that occurs for several reasons. The first reason is that if only the finite difference method was used, the entire wavefield would need to be computed for each iteration. The raytracing on the other hand is an expense that needs to be taken only once, reducing the computation time drastically compared to traditional waveform inversion methods. The second factor is that the finite difference method has been implemented in the time domain. If the finite difference method was implemented in the frequency domain it would reduce the computation time of the finite difference

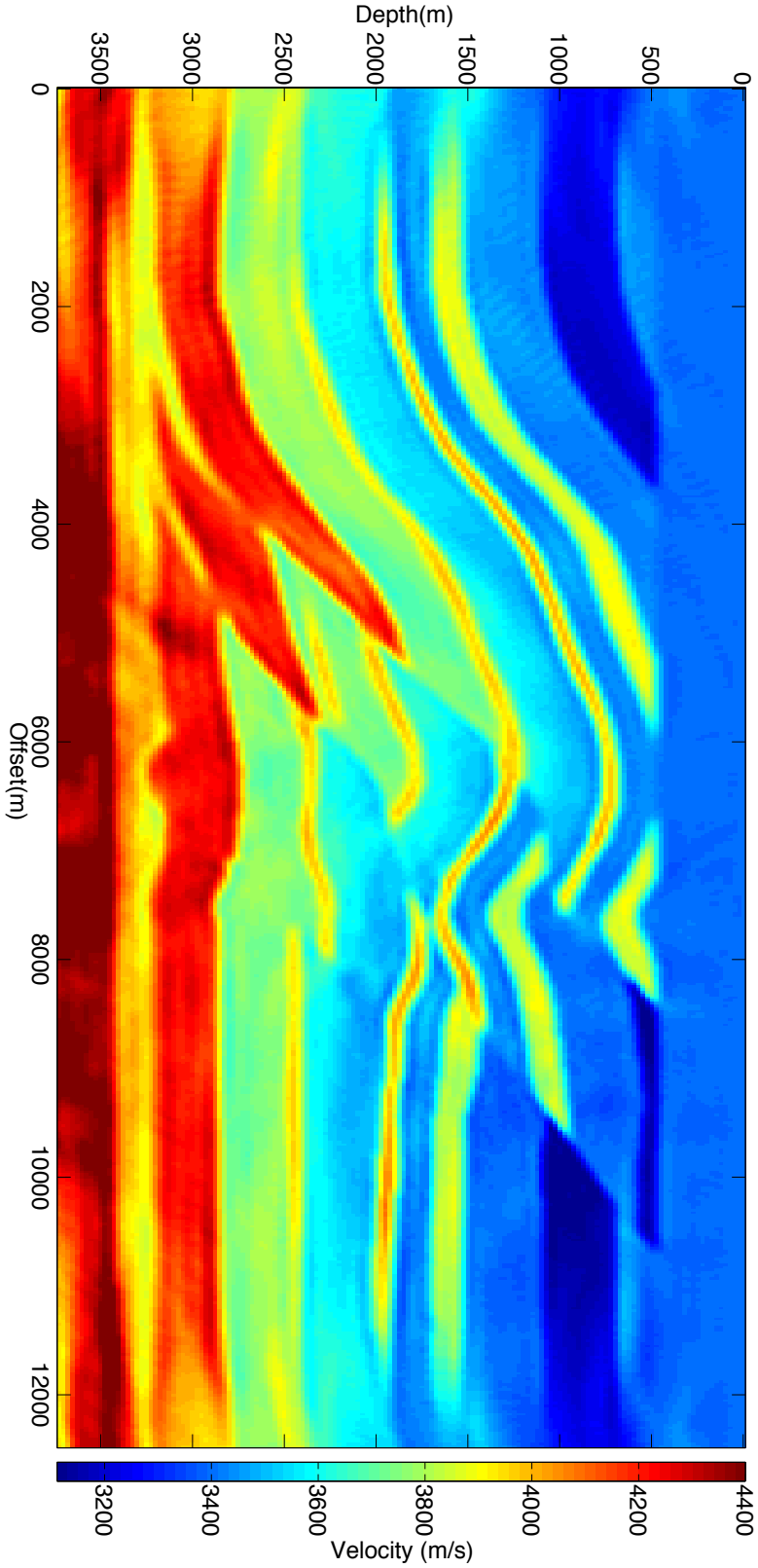

Figure 5.11: Waveform inversion using FWT2D discussed in Sourbier et al. (2009a) and Sourbier et al. (2009b)

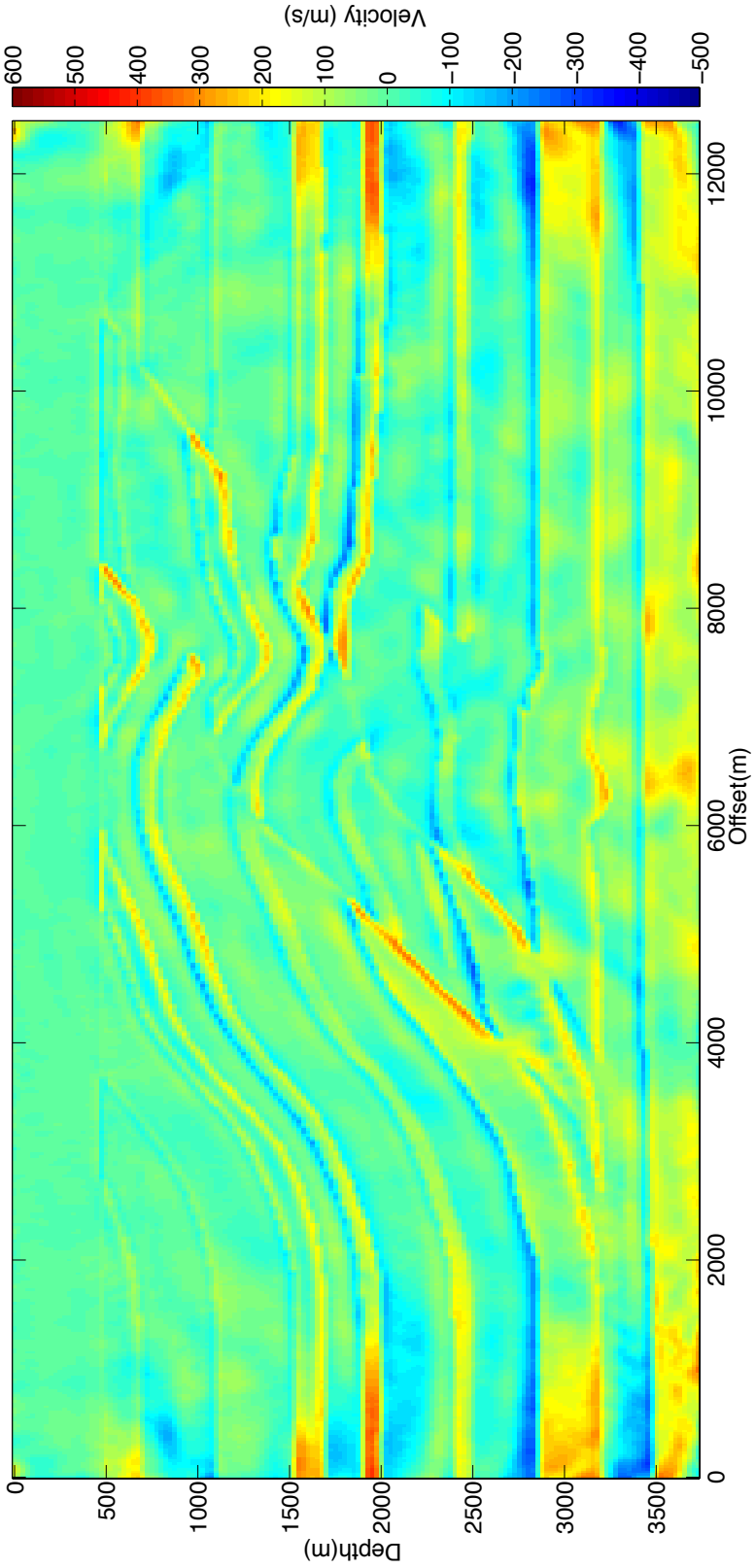

Figure 5.12: ray-Born approximation inversion result subtracted from the SEG/EAGE overthrust model

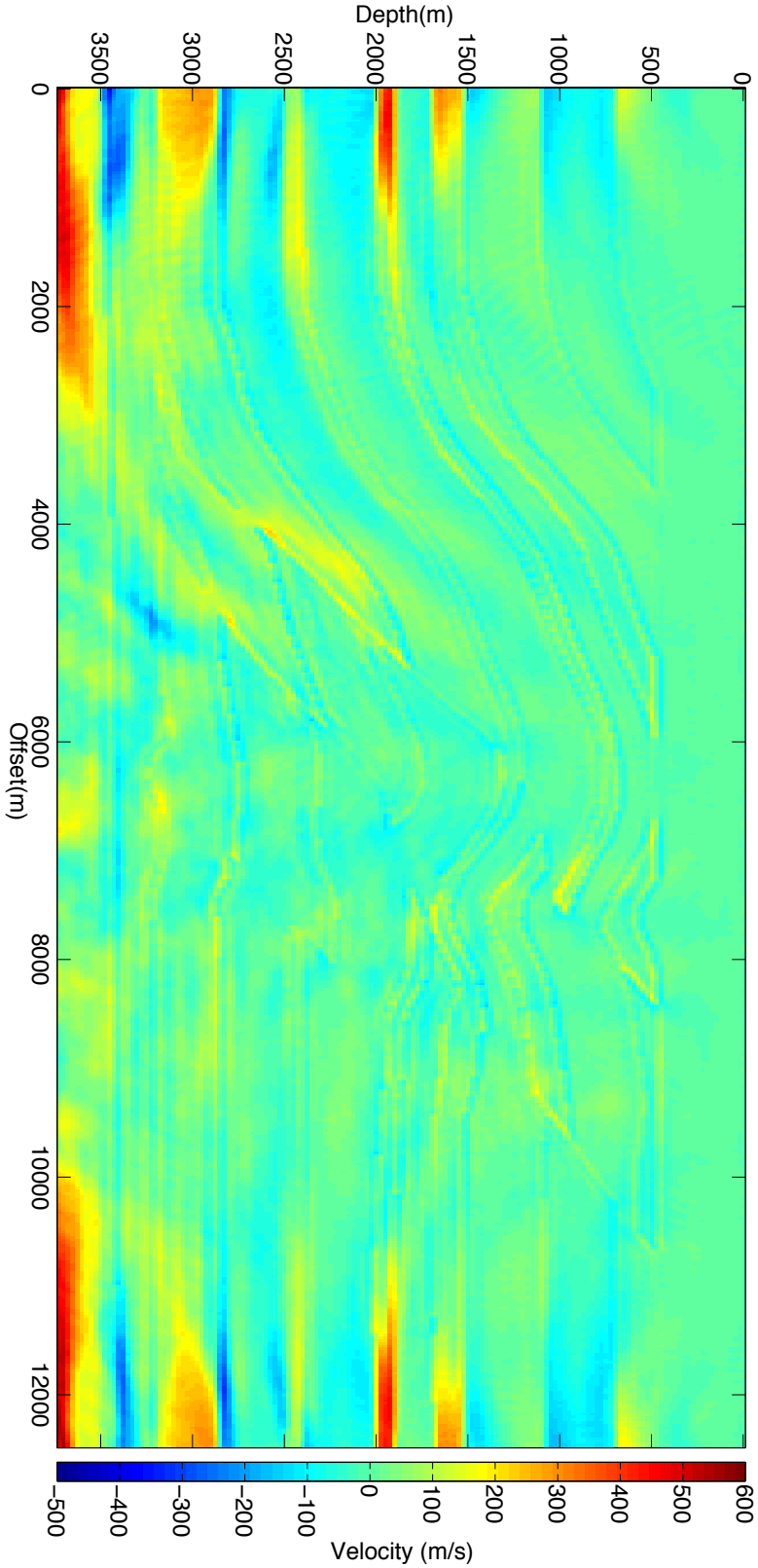

Figure 5.13: FWT2D inversion result subtracted from the SEG/EAGE overthrust model

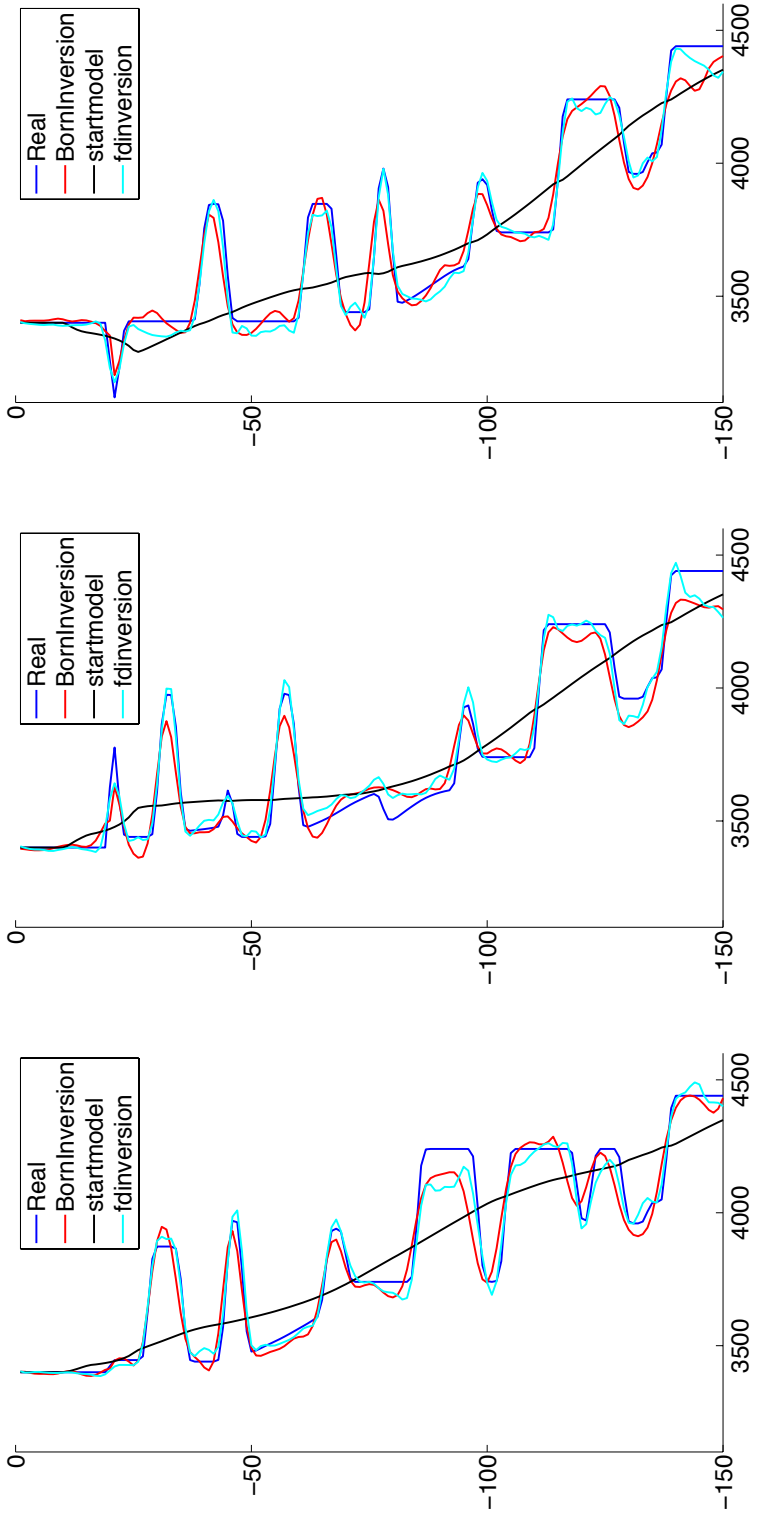

Figure 5.14: 1-D velocity profiles from the SEG/EAGE overthrust model, background model for the inversion, ray-Born approximation inversion result and FWT2D inversion result.

method because the synthetic seismogram could be generated for all the sources at the same time. The third factor is that the boundaries of the model were expanded when using the finite difference method. This was done in order to prevent reflections from the boundary to affect the synthetic seismograms recorded at the receivers. The computation time of the finite difference method could therefore be improved by implementing effective absorbing boundary conditions that remove boundary reflections. The raytracing can however also be performed more efficiently by interpolating the model onto a coarser grid and perform raytracing in the coarser model. This could drastically reduce the computation time of the raytracing. The computation time of the ray-Born approximation inversion compared to the FWT2D program has not been performed in this thesis as the FWT2D is paralellized and implemented with a different programming language, preventing direct comparison.

5.7 Discussion

In this chapter the ray-Born approximation has been used in a full waveform inversion algorithm. The inversion algorithm was implemented in the frequency domain and iterations were performed with frequencies ranging from 2 to 20 Hz. The lowest frequencies were inverted for first and the frequency was gradually increased so that gradually more features in the model were resolved. The accuracy of the waveform inversion algorithm was evaluated with varying receiver spacing and source/receiver geometries. By performing inversions with on iteration, the optimal regularization parameters, the damping and smoothing parameters were found. The inversion results were further improved by performing an additional finite difference iteration. The inversion result shows that the ray-Born approximation is able to accurately reproduce structures and velocities in the subsurface in a fast and efficient way. The benefit of the method is that the raytracing does not need to be performed for every iteration, but will yield a good result by just using the traveltime and amplitude computed for the original background model. The method has some disadvantages, if raytracing is only performed in the original background model, the traveltime in the background model will be inaccurate and it is hard to retrieve the largest velocity contrasts relative to the background model. This inaccuracy will be largest close to the lower boundary of each layer. The second disadvantage is that thin layers are not reproduced very well. The inversion result obtained using the ray-Born approximation was compared to the inversion result achieved by using FWT2D for the same frequencies and source/receiver geometry. The results showed that the FWT2D inversion will better reproduce the small thin layers and that the largest velocity contrasts are better retrieved. Despite the advantages of the finite difference method, the ray-Born approximation inversion is considerably faster than the finite difference method implemented in this thesis and will resolve all the subsurface structures. It is therefore a viable alternative to full waveform inversion algorithms using finite difference only.

Chapter 6

Discussion and Conclusion

6.1 Forward Modelling

A thorough comparison has been performed between the finite difference method and the ray-Born approximation. This comparison was performed in order to evaluate if the ray-Born approximation could be used as a replacement for the finite difference method in forward modelling. The comparison was performed using three background velocity models and four scattering models. Synthetic seismograms were generated for each model for several frequencies and perturbations strengths. The results show that the ray-Born approximation accurately reproduces the pressure field in models where the relative difference between the scatterer and the background model is ten percent or less. The ray-Born approximation will however have problems in velocity models where multipathing occur or in models where the relative difference between the background model and the scatterer is large. The ray-Born approximation is faster than the finite difference method, except in cases where there are a lot of receivers relative to the number of sources.

6.2 Inversion

The ray-Born approximation was evaluated to yield sufficiently accurate forward modelling results at a low cost relative to the finite difference method. It was therefore decided that the ray-Born approximation could be used as the primary forward modelling technique in a full waveform inversion algorithm. The full waveform inversion algorithm was developed and applied to the modified SEG/EAGE Overthrust model. The optimal regularization parameters were found by computing the L-curve. By performing several inversions it was found that the accuracy of the waveform inversion decreases with increasing source/receiver spacing and that due to multipathing in the background velocity model one should not use receivers with larger distance than 5 km from the source for this specific velocity model. Using this information it was possible to achieve a very good inversion result. The inversion result was compared to a result that was obtained using a full waveform inversion algorithm with the finite difference method as the primary forward modelling method. The comparison showed that the inversion algorithm that was developed in this thesis could produce an inversion result with a high accuracy when compared to the finite difference full waveform inversion.

6.3 Future Work

The ray-Born approximation has proven to be a viable option both for forward modelling and full waveform inversion. Using the current implementation as a basis, there are several directions that can be taken to further develop the method.

6.3.1 Generalized ray-Born

The ray-Born approximation is solved by computing traveltime and amplitude from a smoothly varying background velocity model $c_0(\mathbf{x})$, where the reflections are generated from a scatterer $c_1(\mathbf{x})$. If the scatterer is large or the velocity contrast relative to the background velocity model is large, the traveltime and amplitude computed using the ray-Born approximation will be inaccurate. Coates and Chapman (1990) describes the generalized ray-Born approximation that will allow the traveltime and amplitude to be computed in the real velocity model $c(\mathbf{x}) = c_0(\mathbf{x}) + c_1(\mathbf{x})$. The implementation of the generalized ray-Born approximation can remove the timeshift that occur for large velocity contrasts and improve the forward modelling results. Tests should therefore be performed while using the generalized ray-Born approximation in order to evaluate the accuracy and cost of the method relative to the ray-Born approximation and the finite difference method.

6.3.2 Multipathing

One of the weaknesses of the ray-Born approximation is that the amplitude and traveltime computed with raytracing are inaccurate in heterogenous media where multipathing occur. The raytracer can therefore be further improved by correcting for the multipathing effect. Techniques that can be used to correct for the multipathing effect are discussed in Chapman and Keers (2002) and Amodei et al. (2006). These techniques are computationally more expensive and complex than traditional raytracing techniques.

6.3.3 Full Waveform Inversion in 3-D

Traditionally full waveform inversion algorithms have been limited to 2-D for several reasons. Traditional full waveform inversion algorithms are computationally very expensive and the increase in cost of going from 2-D to 3-D is very large. The second limitation is that the size of the problem. The Helmholtz matrix can be computed when using the finite difference method in the frequency domain. Due to the size of the Helmholtz matrix the finite difference method cannot be used in the frequency domain for very large problems. The results obtained show that the ray-Born approximation is computationally less expensive and less memory consuming than the finite difference method in the frequency domain. The ray-Born approximation waveform inversion algorithm should therefore be expanded to 3-D in order to evaluate the computation time and accuracy in 3-D.

6.3.4 Full Waveform Inversion in Elastic Media

Most full waveform inversion algorithms are limited to using the acoustic wave equation due to the increased computation time of the problem in the elastic case. The computation time is higher when using the elastic wave equation because the synthetic seismograms for the S-waves need to be computed in addition to the synthetic seismograms for the P-waves. Not only is it needed to perform extra computations, the velocity of S-waves is also lower than the velocity of P-waves. A denser grid is

therefore needed in order to satisfy the criteria stated in equation (3.18). Some of the attempts to perform full waveform inversion include Brossier et al. (2009) who performed full waveform inversion using the elastic wave equation using the SEG/EAGE overthrust model and Xiong et al. (2013) who performed full waveform inversion using the elastic wave equation in 2.5-D using the elastic Marmousi model discussed in Martin et al. (2006). The ray-Born approximation full waveform inversion algorithm can be expanded to use the elastic wave equation and attempts could be made to perform full waveform inversion in both 2-D and 3-D.

6.3.5 Applications to Real Data

The goal of any full waveform inversion algorithm is its application to real data. Among those who have attempted full waveform inversion with the acoustic wave equation using real data in 2-D are Pratt and Shipp (1999), Hicks and Pratt (2001) and Operto et al. (2006). The ray-Born approximation full waveform inversion algorithm has several interesting applications. Not only can the algorithm be used to find a model of the subsurface, it can also be applied very efficiently in 4-D full waveform inversion algorithms. When working with 4-D seismic data, we have an image of the subsurface after the first waveform inversion. After a given timespan the next waveform inversion will be performed for the same model using a new dataset. In cases such as these, we can in many cases know that no changes have occurred in the model with the exception of the reservoirs. It is therefore possible to limit the target area of the ray-Born approximation to only include an area close to the reservoir. This will greatly limit the size of the model, increase the speed of the waveform inversion and allow the use of higher frequencies in the target area.

6.4 Conclusion

The ray-Born approximation full waveform inversion algorithm has successfully been applied to the SEG/EAGE overthrust model and the ray-Born approximation has proven to be able to create forward modelling results with comparable accuracy to the finite difference method. The method can be further developed by using the generalized ray-Born approximation and using a raytracer that takes multipathing into account. The method can further be applied to the elastic wave equation, expanded into 3-D and applied to real data. One can conclude that the possibilities of the method are vast and more research needs to be performed to further define the limitations and possibilities of the method.

References

Alford, R., K. Kelly, and D. Boore (1974). Accuracy of finite-difference modeling of the acoustic wave equation. *Geophysics 39*(6), 834–842.

Aminzadeh, F., J. Brac, and T. Kunz (1997). SEG/EAGE 3D Modeling Series No 1. *SEG and EAGE*.

Amodei, D., H. Keers, D. Vasco, and L. Johnson (2006). Computation of uniform wave forms using complex rays. *Physical Review E 73*(3), 036704.

Aster, R. C., B. Borchers, and C. H. Thurber (2012). *Parameter estimation and inverse problems*. Academic Press.

Auld, B. A. (1973). *Acoustic fields and waves in solids*, Volume 1. Wiley New York.

Baig, A. and F. Dahlen (2004). Traveltime biases in random media and the S-wave discrepancy. *Geophysical Journal International 158*(3), 922–938.

Bleistein, N., J. K. Cohen, and J. W. Stockwell Jr (2001). *Mathematics of multidimensional seismic imaging, migration, and inversion*, Volume 13. Springer Verlag.

Brossier, R., S. Operto, and J. Virieux (2009). Seismic imaging of complex onshore structures by 2D elastic frequency-domain full-waveform inversion. *Geophysics 74*(6), WCC105–WCC118.

Cerveny, V. (2005). *Seismic ray theory*. Cambridge University Press.

Chapman, C. H. and H. Keers (2002). Application of the Maslov seismogram method in three dimensions. *Studia Geophysica et Geodaetica 46*(4), 615–649.

Coates, R. and C. Chapman (1990). Ray perturbation theory and the Born approximation. *Geophysical Journal International 100*(3), 379–392.

Fowler, C. M. R. (1990). *The Solid Earth: An Introduction Global Geophysics*. Cambridge [England]; New York: Cambridge University Press.

G. Rodriguesz, D. T. (2005). An algorithm for estimating the optimal regularization parameter by the L-curve. *Rendiconti di matematica e delle sue applicazioni 25*, 69.

Gauthier, O., J. Virieux, and A. Tarantola (1986). Two-dimensional nonlinear inversion of seismic waveforms: Numerical results. *Geophysics 51*(7), 1387–1403.

Geiger, H. D. and P. F. Daley (2003). Finite difference modelling of the full acoustic wave equation in Matlab. *CREWES Research Report 15*.

Hicks, G. J. and R. G. Pratt (2001). Reflection waveform inversion using local descent methods: Estimating attenuation and velocity over a gas-sand deposit. *Geophysics 66*(2), 598–612.

Hudson, J. (1977). Scattered waves in the coda of P. *J. Geophys 43*, 359–374.

Hustedt, B., S. Operto, and J. Virieux (2004). Mixed-grid and staggered-grid finite-difference methods for frequency-domain acoustic wave modelling. *Geophysical Journal International 157*(3), 1269–1296.

Keers, H. (1997). *Chaotic ray behavior and asymptotic waveforms in regional seismology*.

Kincaid, D. R. and E. W. Cheney (2002). *Numerical analysis: mathematics of scientific computing*, Volume 2. Amer Mathematical Society.

Krebes, E. (2004). Seismic forward modeling. *CSEG Recorder 30*, 28–39.

Lay, D. C. (1994). Linear algebra and its applications. *New York*.

Lehtinen, J. (2003). Time-domain numerical solution of the wave equation.

Lines, L. R., R. Slawinski, and R. P. Bording (1999). A recipe for stability of finite-difference wave-equation computations. *Geophysics 64*(3), 967–969.

Martin, G. S., R. Wiley, and K. J. Marfurt (2006). Marmousi2: An elastic upgrade for Marmousi. *The Leading Edge 25*(2), 156–166.

Menke, W. (1984). Geophysical Data Analysis: Discrete Inverse Theory Academic. *New York*.

Moser, T. J. (2012). Review of ray-Born forward modeling for migration and diffraction analysis. *Studia Geophysica et Geodaetica 56*(2), 411–432.

Nowack, R. (2010). Seismic interferometry and estimation of the Green function using Gaussian beams. *Earthquake Science 23*(5), 417–424.

Operto, S., J. Virieux, J.-X. Dessa, and G. Pascal (2006). Crustal seismic imaging from multifold ocean bottom seismometer data by frequency domain full waveform tomography: Application to the eastern Nankai trough. *Journal of Geophysical Research: Solid Earth (1978–2012) 111*(B9).

Pratt, G., C. Shin, et al. (1998). Gauss–Newton and full Newton methods in frequency–space seismic waveform inversion. *Geophysical Journal International 133*(2), 341–362.

Pratt, R. G. and R. M. Shipp (1999). Seismic waveform inversion in the frequency domain, Part 2: Fault delineation in sediments using crosshole data. *Geophysics 64*(3), 902–914.

Pujol, J. (2003). *Elastic wave propagation and generation in seismology*. Cambridge University Press.

Ricker, N. (1953). The form and laws of propagation of seismic wavelets. *Geophysics 18*(1), 10–40.

Ryan, H. (1994). Ricker, Ormsby, Klauder, Butterworth-A choice of wavelets. *Hi-Res Geoconsulting*.

Sourbier, F., S. Operto, J. Virieux, P. Amestoy, and J.-Y. LExcellent (2009a). FWT2D: A massively parallel program for frequency-domain full-waveform tomography of wide-aperture seismic dataPart 1: Algorithm. *Computers & Geosciences 35*(3), 487–495.

Sourbier, F., S. Operto, J. Virieux, P. Amestoy, and J.-Y. LExcellent (2009b). FWT2D: A massively parallel program for frequency-domain full-waveform tomography of wide-aperture seismic dataPart 2: Numerical examples and scalability analysis. *Computers & Geosciences 35*(3), 496–514.

Tarantola, A. (1984a). Inversion of seismic reflection data in the acoustic approximation. *Geophysics 49*(8), 1259–1266.

Tarantola, A. (1984b). Linearized inversion of seismic reflection data*. *Geophysical prospecting 32*(6), 998–1015.

Tarantola, A. (2005). *Inverse problem theory and methods for model parameter estimation*. Society for Industrial & Applied.

Xiong, J., Y. Lin, A. Abubakar, and T. Habashy (2013). 2.5-D forward and inverse modelling of full-waveform elastic seismic survey. *Geophysical Journal International*.

Youzwishen, C. F. and G. F. Margrave (1999). Finite difference modeling of acoustic waves in Matlab. *the 11th Annual Research Report of the CREWES Project*.